Additive manufacturing of polyolefins via powder bed fusion

Jackson Sewall Bryant

Dissertation submitted to the faculty of the Virginia Polytechnic Institute and State University in partial fulfillment of the requirements for the degree of

Doctor of Philosophy

In

Macromolecular Science & Engineering

Christopher Williams, Chair

Michael Bortner, Co-Chair

Robert Moore, Member

Michael Bartlett, Member

Mark Dadmun, Member

December 13th, 2023

Blacksburg, VA

Keywords: powder bed fusion, selective laser sintering, polypropylene, polyethylene

Additive manufacturing of polyolefins via powder bed fusion

Jackson S. Bryant

(Abstract)

Powder bed fusion (PBF) is an additive manufacturing (AM) process in which a fine polymer powder is selectively heated and melted using infra-red (IR) energy from a CO_2 laser to melt the powder and coalesce the molten polymer together to form each layer. Semi-crystalline polymers are the most common thermoplastics processed in this AM process and powder is heated during the printing process to retard crystallization in the material. When crystallization happens too rapidly, warpage of a layer, which can lead to print failure is possible.

Polyolefins represent a class of thermoplastic chiefly comprised of polyethylene and polypropylene. These materials are highly used in engineering applications however, their rapid crystallization kinetics generally make them much less suitable for PBF. They represent a material class in which traditional processing approaches with PBF are not always sufficient to enable printability. In this dissertation, printing of multiple polyolefins is investigated to both understand the processing of these materials and grow an overall understanding of processing in PBF for any polymer.

A process chain which relies on fundamental polymer behavior is devised to process ultra-high molecular weight polyethylene (UHMWPE). This material has sufficiently high molecular weight that the viscosity is so high it is not considered to flow in the melt. The difficulty in coalescing this material was overcome by using melt explosion during processing to create some entanglements between adjacent powder particles and form a green part that could then be post-processed in the melt to develop final part properties. The viscosity of this material enabled shape retention during

this post-processing. Though this process chain enabled printing of UHMWPE, the printed parts were highly porous even after post-processing.

Post-processing under pressure was investigated to further densify printed parts to achieve the mechanical performance expected for UHMWPE. By employing both cold isostatic pressing (CIP) and hot isostatic pressing (HIP), fully dense UHMWPE samples were realized. Strain at break was on par with traditionally processed UHMWPE was achieved, and tensile strength was only slightly less than the traditional processed material.

Copolymerization of polypropylene (PP) with polyethylene (PE) to create random PP-PE copolymers, and its impact on material properties and processing was investigated. Increases in ethylene content were expected to decrease crystallization kinetics, which would increase processability of the material. Here, increases in processability means decreases in the likelihood of warpage. Though increases in ethylene content did lower the crystallization kinetics, these increases also significantly shifted the onset of melting for the copolymer to much lower temperatures, which limited the temperatures in which the material could be printed. Together these two changes led to a polymer that was more processable when ethylene content was 2.2% and then processability decreased as the ethylene content was increased to 4.9%. Printed parts from each copolymer showed a decrease in crystallinity with increasing ethylene content. Strain at break increased while tensile strength decreased with increasing ethylene content.

A method of emulation of the PBF process was created to enable prediction of crystallization during processing. This method used *in situ* thermal measurements of the printing process to inform a thermal model to generate temperature profiles for a printed layer and then used these temperature profiles in fast scanning calorimetry (FSC) to emulate a printed layer's thermal

history. This emulation enabled prediction of the crystallinity and the shape and temperatures covered by the melting endotherm during the printing process.

Investigations of printing UHMWPE and PP-PE copolymers helped expand processing knowledge of polyolefins and of polymers in PBF overall. Challenges in viscosity during printing were overcome by exploring unique processing and post-processing methods to enable PBF of UHMWPE. An understanding of the impacts of ethylene content on processing and properties of PP-PE copolymers was developed and this insight can be valuable to guide future development of polyolefins for PBF. A powerful methodology for emulating the PBF process to understand crystallization was developed. This emulation provides an alternative to crystallization modeling and characterizes the crystallinity in a printed layer rather than just determining an amount of crystallinity. Through each of these contributions, understanding of PBF of polyolefins and the PBF process in general has been furthered.

Additive manufacturing of polyolefins via powder bed fusion

Jackson S. Bryant

(General audience abstract)

Powder bed fusion (PBF) is an additive manufacturing (AM), or 3D printing, process. Like every type of 3D printing, this process builds 3-dimensional parts one layer at a time. In PBF a polymer powder, which looks similar to a fine sand, is selectively heated and melted using energy from a laser to melt the powder and form a layer. It does this by scanning across the surface of the powder in the desired layer shape.

Polyolefins represent the most used types of plastics. This research investigated both polyethylene (PE) and polypropylene (PP), which are common plastics that most people interact with every day. These materials are highly used in engineering applications. However, they rapidly shrink as they cool from a liquid to a solid, which leads to difficulties as layers can deform during printing. Due to this difficulty, they are a fairly new class of materials to print.

This dissertation includes the development of a method for printing a type of polyethylene so viscous that it doesn't flow even when it's a liquid. In this method, the part was only lightly scanned in the printer and was heated in an oven afterward to give the part strength. This method worked to print parts of the correct shape, but the parts were weak. Many other approaches were investigated to compress the parts to strengthen them. An approach in which parts were compressed at high pressures and heated proved successful for fully condensing parts together and led to the strongest 3D printed parts ever made using PBF.

Another focus of this dissertation was trying to print polypropylene which had changes in its chemistry. These changes slowed down the shrinkage of the material during cooling and changed

the structure of the part on a microscopic scale. Adjustments in chemistry were found to weaken parts but make them stretch more before breaking. With small adjustments to the chemistry parts were less likely to warp during printing and make the print fail, however, with a higher change in the chemistry away from polypropylene, the powders became harder to print. This research began the investigation into understanding how a specific change in chemistry could impact the properties and processing of polypropylene materials, with the goal of making materials that are easier to print.

Finally, a method to reproduce how a powder is heated by the laser and then cooled was developed. This method used an infra-red (IR) camera to measure the temperature of the powder during and following scanning and then used a temperature model to predict the temperature of that as the rest of the part was printed. By using this reproduction, the structure of each layer could be predicted during the build. This method will help understand what happens to the powder during the printing process.

Investigations of printing UHMWPE and PP helped expand processing knowledge of polyolefins and of polymers in PBF overall. Challenges in viscosity during printing were overcome by exploring unique processing and post-processing methods to enable PBF of UHMWPE. An understanding of the impacts of ethylene content on processing and properties of PP-PE copolymers was developed and this insight can be valuable to guide future development of polyolefins for PBF. A powerful methodology for emulating the PBF process to understand PBF was developed. Through each of these contributions, understanding of PBF of polyolefins and the PBF process in general has been furthered.

Acknowledgements

I feel very fortunate to have had the opportunity to work with such great scientists during my time at Virginia Tech. I would like to give special thanks to: Daniel Rau, Michelle Pomatto, Yifeng Lin, John Reynolds, Akan George, Camden Chatham and Ian Ho for their support during our collaborations.

My family was endlessly supportive during this endeavor and I am eternally thankful for the support both before and during my PhD.

Thank you to the friends I've made along that way that helped me persevere even during the most difficult times these past five years: Joel Serrano, Glenn Spiering, Amy Cheng, James Brown, my bandmates in Ranger Maid & Yung Lzrd, and my Friday coffee group.

Table of Contents

List of figures

List of Tables

Chapter 1: Introduction

The overall aim of this dissertation is to further the understanding of powder bed fusion (PBF) of polyolefin materials. Polyolefins offer properties unique from polyamide materials which are the almost exclusive materials processed via PBF, especially in industrial printing. Unlike the polyamides traditionally used in PBF, polyolefin materials do not undergo post-condensation reactions during processing that lead to changes in viscosity of the material, have high chemical resistance, and the opportunity to achieve higher elongations at break. These materials crystallize quickly relative to most semi-crystalline polymers, which leads to challenges in their processing coming from warpage. When shrinkage during cooling occurs too quickly during printing, stresses build up and warpage can occur. Shrinkage-rate is proportional to crystallization rate. Ultra-high molecular weight polyethylene (UHMWPE) is a polyolefin material with exceptionally high melt viscosity which makes it not flow while in the melt, and therefore inhibits coalescence. Since no pressure or shear is applied during the PBF process, these materials coalesce only via surface tension. This behavior can pose significant challenges to successfully processing these materials.

1.1 Motivation

Laser-based polymer powder bed fusion (PBF) is an additive manufacturing process in which a polymer (usually semi-crystalline) powder is selectively scanned and melted using a CO_2 laser. The polymer melt coalesces via surface tension and then cools and crystallizes to form a printed part. This process has the capability to batch process parts and work on an industrial scale. This scale and the capability to print semi-crystalline polymers, which are known for their high performance, makes this process especially powerful.

Though PBF has been extensively studied, the materials that are widely processable are still limited. Polyamide materials, specifically polyamide 11 & 12, still dominate the commercial market. Though these materials are valuable, they are not the best option for all applications and experience significant difficulties with recyclability in the process due to post-condensation reactions that happen in the printer. Polyolefin materials are of specific interest because of their common use in traditional polymer manufacturing and because they do not undergo post-condensation reactions during printing.

This research is driven by the goal of furthering understanding of PBF to enable successful processing of polyolefin materials. In literature, analysis of printing these materials is almost always limited to process-property relationships. Structure is not included and therefore trends based on a deep understanding of the materials have not been sufficiently formed. This literature is explored at length in Chapter 2.

This dissertation has four research chapters. Chapters 3 and 4 investigate PBF processing and post-processing of ultra-high molecular weight polyethylene (UHMWPE). Chapters 5 and 6 investigate processing and crystallization of polypropylene (PP) and polypropylene-ethylene (PP-PE) copolymers during the PBF process. Each chapter has a set of research questions that are detailed below.

1.2 Research questions

Chapter 3

- How can UHMWPE be processed to coalesce particles during the printing process even though viscosity suggests coalescence is not possible?

- How can the expansion that occurs during melting of UHMWPE be mitigated to enable printing of multi-layer parts?
- How can printed parts be densified to increase their mechanical properties?

Chapter 4

- How does pressure impact densification of a printed UHMWPE part?
    - What differences in densification occur during this process when comparing a cold isostatic pressing and hot isostatic pressing?
- How do results of a fully densified printed UHMWPE sample compare to a melt-pressed sample?

Chapter 5

- How do changes in ethylene co-monomer content impact processing of PP-PE materials in PBF?
- How do resultant mechanical properties and structure of printed parts change with increases in ethylene content?
- How does PBF processability change with ethylene content?

Chapter 6

- How can crystallinity of a given layer during a PBF build be predicted?
- How can a methodology to emulate crystallization during PBF maximize the direct measurements of a material?

Chapter 2: Review of powder bed fusion of polyolefins

This chapter is comprised as the author's contribution to the following review paper published in *Polymer Reviews*:

Das, Arit, **Jackson S. Bryant**, Christopher B. Williams, and Michael J. Bortner. "Melt-Based Additive Manufacturing of Polyolefins Using Material Extrusion and Powder Bed Fusion." *Polymer Reviews* (2023): 1-66.

2.1 Powder Bed Fusion (PBF): Process Considerations

Polymer PBF refers to the AM modality in which a fine polymer powder is selectively melted and coalesced by an energy source. In laser PBF (L-PBF), fresh powder is deposited onto the previously coalesced layer and scanned with an IR laser to create a three-dimensional object. PBF is an AM process which shows promise for being extensively used to make production parts in the future because of its ability to batch-process parts and lack of need for support material[1].

In this review, only L-PBF will be considered due to its prominence in literature as the first PBF process, as processing polyolefins through the high-speed sintering or multi-jet fusion modalities of PBF have not been reported extensively in the existing literature. In PBF, the energy supplied to the powder is a combination of the bed temperature (T_b) and the energy supplied by the laser during scanning[2]. The temperature the powder is held at during printing, T_b, is set by internal heating elements within the PBF machine. Energy supplied by the laser is most often described by "energy density"[3]. Energy density (ED) is a composite value that combines the most commonly controlled printing parameters of PBF machines, which includes laser power (W), beam velocity (mm/s), hatch spacing (mm), scan count (#), and layer height (mm). When combined, these parameters describe the volumetric ED (J mm^{-3}) if layer height is included, and ED (J mm^{-2}) if this value is excluded[2].

Polymer powder is most often heated to slightly below (~15° C) its melting temperature (T_m) since crystallization will occur slower the closer the T_b is to the polymer's equilibrium melting temperature[2]. Most often T_b is above the onset of crystallization observed when measuring the polymer of interest using differential scanning calorimetry (DSC) at 10° C/min. This slower crystallization will reduce warpage of a coalesced layer[4]. It must be kept in mind that the fairly rapid crystallization kinetics of polyolefins make them somewhat difficult to process in a manner that severely limits the crystal size to significantly reduce the melting temperature range (e.g., cooling out of the melt very quickly to limit crystallization). During the PBF process the powder is gradually warmed up from ambient temperature to the set bed temperature for processing (usually 1-2 h). During this time, the powder can anneal and form larger crystals that melt at higher temperatures. There can be other cases in which annealing does not occur significantly (high atactic content for PP or high co-polymer content for PE—both scenarios in which crystallinity in the sample will be severely limited).

Schmid notes that development of new materials for PBF are necessary to increase the applications for which PBF is suitable[5]. PE and PP are especially important for growing PBF markets in the automotive, electronics, and aviation industries[5]. To date, most PBF research has focused on polyamides because they are most prevalent industrially in powder form[6]. A number of studies on polyamides have focused on reuse or recycling rates of powders. However, because these polymers are step-growth polymers which can undergo post-condensation reactions that increase molecular weight and therefore viscosity, conclusions regarding reuse and recycling of powders may not be valid for non-step growth polymers such as PE and PP[2,7]. Another benefit of processing polyolefins via PBF is that the materials have lower melting temperatures than polyamides, which reduces energy consumption during processing[1].

Successful printing of a material via PBF is determined by the ability to print complex parts (parts with cross-sectional areas that change from layer to layer) with mechanical properties comparable to those for traditional manufacturing methods for that polymer (such as injection molding). To accomplish this, it is necessary to heat the polymer above T_m to consolidate and densify the material without (i) degrading the material and, (ii) without inducing layer warpage that could cause a print to fail.

Most current research in PBF of polyolefins is limited to reporting the most successful printing conditions for a specific powder. In the ensuing sections, we investigate the published research on PBF processing of PE and PP and discuss important successes and conclusions of each work. Afterwards we offer recommendations of future research areas that are necessary to accomplish successful PBF-based printing of polyolefins.

2.2 PBF of Polyethylene (PE)

Overall, the research into PBF of HDPE is very limited, which is likely due to warpage during printing, however it is uncommon to report on printing failures within PBF literature. Often, researchers only note that a processing window is small, which does little to help other researchers assess the printing difficulties for HDPE. The lack of more literature in this area, as summarized by the few reports in Table 2.1, combined with the limited mechanical properties of the HDPE processed via PBF suggests there is significant research to be accomplished on PBF of this polymer.

Research into PBF of HDPE began with Salmoria et al.'s investigation of printing parts using powders with different particle size distributions. They observed lower densities and mechanical

properties as the particle size distribution increased[8]. Bai et al. found success printing HDPE by supplying scanning layers twice[9]. This scan strategy helped deliver energy to the sample more gradually and made geometrically accurate parts. However, Bai's settings led to a maximum tensile strength of only 6 MPa, which is much lower than the 20-40 MPa tensile strength expected for injection-molded HDPE[9,10]. They note that inconsistencies in mechanical properties of their printed parts is an impediment to printing HDPE[9]. Hoelzel's research focused on trying to print HDPE via PBF at a low cost with a custom built PBF machine[11]. Hoelzel's print strategy included using tape in the print bed to promote first layer adhesion and help reduce warpage; notably, Hoelzel also printed some complex parts from HDPE. Hoelzel obtained mechanical properties comparable to the cast samples used as a control[11].

Different HDPE composite materials have been explored for medical applications. One that has received the notable interest is hydroxyapatite (HA) reinforced HDPE, useful because bone bonds to hydroxyapatite[12]. The first research on this composite determined that a CO_2 laser could successfully deliver energy to coalesce this composite[13]. Hao et al. first performed preliminary tests of HA-HDPE composites by analyzing printing of single layers[14]. They successfully printed single layers and showed increases in density with increased ED for 30 and 40 vol% HA composites[14]. Later Bao et al. successfully printed multilayer 40 vol% HA parts at different particle size distributions[15]. Although multi-layer parts were printable, all parts, regardless of particle size distribution and printing parameters, were too fragile for mechanical testing. Hao et al. suggested that this was due to the high filler percentage and that more robust parts could be produced with a higher concentration of HDPE[15]. Zhang et al. demonstrated printability of a 20 vol% HA-HDPE manufactured DMA test specimens[16]. Zhang et al. further

found that 20 vol% HA-HDPE composites produced via PBF showed good biocompatibility[17]. Salmoria et al. was able to print HA-HDPE scaffolds at HA wt% ranging from 0-20 wt%[18]. These parts enabled mechanical testing and showed decreasing mechanical properties as HA wt% increased. Salmoria et al. note that tensile strength range determined when testing these composites (4.5-33 MPa) are compatible with bone tissue properties. Fatigue tests showed increased fatigue strength with increasing HA wt% over 1000 cycles[18].

PBF processed HDPE is also of interest for implantable, drug-loaded devices. Salmoria et al. have successfully printed blends HDPE and the cancer treatment drugs fluorouracil and progesterone[19,20]. They printed HDPE/fluorouracil composite waffles for bone cancer treatment, and an HDPE/fluorouracil/progesterone composite intrauterine device for endometrial and ovarian cancer treatment. In each case, the drugs did not inhibit printing. Both blends initially showed rapid drug release followed by a slower, sustained release, which is desirable for these applications[19,20].

UHMWPE is of special interest for AM because of its utility in biomedical applications and wear applications. Initial research into PBF of UHMWPE conducted by Rimell et al.[21] was limited to demonstrating the ability of UHMWPE to coalesce after being scanned by a CO_2 laser in a custom PBF machine. Single-layer lines were printed in this machine. Using IR-spectroscopy, Rimell et al. confirmed that degradation occurred during laser scanning[21]. For Goodridge et al., multilayer UHMWPE parts became printable at T_b = 135°C and over a small laser power range with a scan count of two. Parts were able to be handled thermal post-processing was necessary to improve mechanical properties of the parts to make them sufficient for actual applications[22]. The T_b used for these experiments is notable because it is within the polymer's melting

endotherm. Though the T_b is below the melting peak determined via DSC, it is still expected that some fraction of the polymer's crystals would melt at this T_b[22]. The reason behind this proposition is that even partial melting of the polyolefin crystals will make some polymer chains labile, which could induce coalescence. Small amounts of coalescence between particles increases the average particle size and reduces flowability during powder recoating that hinders the PBF process.

Khalil et al. investigated both tensile and flexural properties of UHMWPE processed via PBF[23,24]. Tensile properties are significantly less than those reported by the material supplier (Ticona). Samples (Figure 12a) did not achieve a relative density exceeding 40% at any processing parameters, likely limiting the mechanical properties of these parts. Much like Goodridge et al., Khalil et al. used a T_b within the polymer's melting endotherm of 142°C, which was above the polymer's peak melting temperature of 141°C[23,24]. Khalil et al. further studied coalescence of UHMWPE using hot-stage microscopy and performed tests to elucidate changes in crystallinity with heating and cooling rates, as highlighted in Figure 12b[25]. At higher cooling rates, the crystallization rate increased (leading to the generation of crystals with more defects), indicating the process to be a nucleation-dominated while the crystallization temperature decreased.[25] However, the degree of crystallinity of UHMWPE remained relatively unchanged when cooled at different rates.

Multiple approaches have been employed to improve processing of UHMWPE in PBF. Ullsperger et al. investigated using near-IR laser pulses at a wavelength of 1030 nm, which they note as a wavelength where PE has poor absorption. Samples were printable but had poor resolution and the smoothness of the fracture surface suggests degradation occurred. These

samples were printed at especially high EDs (6-8 J/mm^2) but showed a tensile strength of 3.9 ± 0.3 MPa[26]. Zhu and Wang explored the addition of a silica filler to increase printability of their UHMWPE powder. Though dimensional accuracy increased for the samples with the filler, samples over a range of energy inputs had about the same tensile strength (~2 MPa) and elongation at break (10%)[27]. Though these examples are still far from achieving properties expected for this polymer when traditionally processed, they offer insight into process and material changes that can be employed in PBF, demonstrating the need to explore new approaches.

One common challenge observed in PBF of UHMWPE is z-direction growth during printing. Goodridge et al. observed this growth in powder across the build piston during the warm-up process[22]. Kozlovsky does not specifically note the expansion but shows images of z-direction growth occurring after laser scanning[28]. Both Khalil et al. and Zhu et al. observed parts with much greater z-direction height than designed[23,24,27]. Zhu and co-authors assign this growth to caking, however the z-direction caking was much greater than in the x & y-directions[27]. Any amount of z-direction growth would create difficulties during re-coating, which makes this unique behavior something that should be further investigated in future research.

Zhao et al. investigated post-processing of PBF-manufactured UHMWPE using a hot isostatic press (HIP)[29]. Pressures ranged from 4-12 MPa and temperatures ranged from 165-185°C. A noticeable increase in mechanical properties was observed with this post-process, and the greatest increase came from a post-process at 185°C and 12 MPa for 1 hour (Figure 12c). Even with the inclusion of post-processing, tensile properties were still much lower than expected for UHMWPE[29]. The main reason behind the poor tensile properties of PBF processed UHMWPE

might be due to the limited amount of chain diffusion and re-entanglement across the printed layer interface through chain reptation. In case of UHMWPE, reptation dynamics is extremely slow due to the high molecular weight and high melt viscosity of the polymer.[30]

2.2 PBF of Polypropylene (PP)

PBF of PP has garnered significantly more attention than PE due to the relatively broader sintering window (T_m-T_c) of around 35°C.[31] A major portion of the literature studies the printability of the polymer by varying the processing parameters. Upon initial investigation of various grades of PP with the intent of determining processability, Fiedler et al. compared various material properties to those of polyamides. Each grade of PP showed much lower absorbance at 10.6 μm when compared to polyamides. Fiedler et al. also found that PP showed a greater temperature difference between the onset of melting and onset of crystallization than the polyamides tested, which suggests better control over processing[32].

Reinhardt et al. performed a design of experiment and used a Taguchi analysis during their research to guide process parameter selection for PBF of PP. is the. Reinhardt et al This work Determined the influence of each key processing parameter, including orientation on the print bed, on mechanical properties and other useful metrics such as dimensional accuracy and curling[33]. Ituarte et al. performed a screening design of experiment for PBF of PP and found that tensile strength increased with increasing energy density, while elongation at break decreased. They also found strong interactions between process parameters, which led to non-linear trends[31].

Zhu et al. achieved a tensile strength comparable to injection molded PP but a much lower strain at break when printing low-isotacticity PP[34]. This difference is attributed to the greater degree of crystallinity achieved during the slow cooling that is part of PBF. The researchers also observed that the relative amounts of each crystal phase differed between IM and PBF samples and changed with changes in energy density for PBF[34]. As illustrated in Figure 13a, it was found the tensile strength increased with increasing energy density up to a certain point, beyond which tensile strength declined[34]. This is analogous to results reported by Caulfield et al.[35] for nylon 12 and the trend was also observed by Wegner et al.[36] Figure 13b illustrates the different complex PP functional parts printed using PBF process parameters selected by Zhu et al.[34]

Understanding crystallization kinetics of a polymer can greatly aid in understanding process-structure-property relationships and printability in PBF. The morphology of the printed parts is dependent on the crystallization kinetics of the polymer under the printing conditions. Armado et al. evaluated isothermal and non-isothermal crystallization for an isotactic co-polypropylene using a Nakamura model and Hoffmann-Lauritzen theory. They found material constants for these models and simulated crystallization over 10 layers of printing[37]. Tan et al. investigated the crystallization kinetics of isotactic PP (iPP) and a PP copolymer (co-PP)[38]. XRD tests of printed samples found that crystalline regions in iPP were predominantly α-phase, while co-PP samples were predominantly γ-phase. This is notable for PBF manufactured co-PP because γ-phase crystalline regions are hard to achieve during injection molding. They found the iPP to have a wider sintering window, which suggests that processing iPP without warpage is easier than for co-PP[38].

A critical powder property for PBF is recyclability in order to have efficient build volume utilization.[39] This property will determine how your material ages with processing. Having a powder that maintains its properties during multiple print cycles will lead to more consistent and less wasteful printing. In a powder recycling study of PP for PBF, Wegner et al. found only small decreases in mechanical properties of recycled powder. They tested virgin powder, recycled powder taken from a 13.5 h build, and a 50/50 blend of virgin and recycled powder. Mechanical properties of parts printed from the recycled powder were only slightly lower than virgin powder, and the authors hypothesized this loss could be minimized at higher EDs[40]. Mwania et al. similarly found insignificant changes in the two PP powders they tested. Crystallinity and viscosity after use and re-use of excess powder from previous builds did not significantly impact material properties [41,42]. Together, this research on recyclability of PP in PBF suggests that polyolefin powders will show greater recyclability than polyamide powders due to their lack of post-condensation reactions during printing.

Glass fiber reinforced PP composites are one of the most common PP composites. Kleijnen sought to increase mechanical properties by reinforcing the PP powder with short (20-150 μm) glass fibers. Though tensile modulus increased by over 50% when PP was loaded at 30 wt.% with 50 μm fibers, the tensile strength decreased. Kleijnen et al. attributed this decrease to poor adhesion between the glass fibers and the PP[43]. Kleijnen et al. also investigated the inclusion of nucleating agents to increase impact strength in PBF produced PP. This inclusion shifted the melting endotherm to lower temperatures and increased impact strength[44]. Preliminary experiments, which were limited to scans that produced single layer parts, have been conducted for PP filled with zeolite[45].

Powder production for PBF can be challenging because the target powder size distribution is 10-120 μm and spherical particles are important for flowability[2,46]. Wang et al. investigated the production of PP powders via thermal-induced phase separation (TIPS)[47]. A variety of solvents were tested, and xylene was found to work best. Using this system, Wang et al. was able to produce highly spherical particles and could control particle diameter and particle size distribution by changing the concentration of PP in the solvent[47]. Fang et al. also worked to produce PP powders via TIPS in xylene. They further successfully used this powder to make parts. Multiple grades of PP were investigated, and Fang et al. found that grades of PP with melt flow rates (MFR) of less than 10 g/(10 min) didn't easily form powders via TIPS[48]. Tan et al.[49] built on Wang et al.'s research when they produced montmorillonite filled PP powder via TIPS in xylene. This work suggests the possibility of using this solvent system to produce both neat and filled PP powders[49].

Other methods of powder manufacturing have also been explored. Schafer et al. saw success in producing spherical polyethylene particles using a novel extrusion process in which jets of air were directed at the extrudate to stimulate Rayleigh disturbances which led to particle formation[50]. Fanselow et al.[51] took a similar approach to Schafer et al. but used melt-emulsification for powder production of both PE and PP. This enabled the production of highly spherical particles in which a portion of the particles were in the correct particle diameter range for PBF[51].

Polypropylene powders have also been modified to improve printability. Gong et al. used a thermal treatment with mixed dispersant system (TTMS) to treat their PP powders. In this method, PP powder was sonicated in a dispersant at 170°C before quenching the sample,

resulting in decreased particle size. Further, the temperature difference between the onset of melting and onset of crystallization was increased, which should reduce warpage during printing[52] as highlighted in Figure 13c. Plasma treatment of PP powders has also been explored. Bonilla et al. successfully used a plasma surface treatment of PP powder to add a colorant to the powder. Only minor changes in crystallinity and particle size were observed[53]. However, the mechanical properties of the printed parts fabricated using plasma treated powders were superior to those printed using untreated powders (Figure 13d). Higher packing density and improved layer resolution in the plasma treated powders likely resulted in the enhanced mechanical performance of the printed parts.

Table 2.1. Mechanical properties of pure polyolefins and their composites along with the relevant print conditions when printed using PBF.

Polymer	Mechanical properties of printed parts	Print conditions	Reference
HDPE	Tensile strength: 5.5 ± 0.3 MPa Tensile modulus: 140.9 ± 15.5 MPa Elongation at break: 32.0 ± 7.7 %	ED: 0.016 J/mm^2 T_b: 101℃	Bai et al. 2016[9]
HDPE	Tensile strength: 10.6 ± 2.0 MPa Tensile modulus: 7.6 ± 0.7 MPa Elongation at break: 3.0 ± 0.4 %	ED: 3.30 J/mm^2 T_b: 125℃	Hoelzel 2019[11]

UHMWPE	Maximum flexural stress: 2.12 ± 0.05 MPa Maximum flexural strain: 60 ± 3%	ED: 0.027 J/mm^2 T_b: 142℃	Khalil et al. 2016[23]
UHMWPE	Tensile strength: 2.42 ± 0.20 MPa Tensile modulus: 72.6 ± 14.9 MPa Elongation at break: 51.4 ± 6.6%	ED: 0.027 J/mm^2 T_b: 142℃	Khalil et al. 2016[24]
PP	Tensile strength: 19.9 ± 0.5 MPa Tensile modulus: 599.1 ± 14.1 MPa Toughness: 19.3 ± 3.5 MJ/mm^3 Elongation at break: 122 ± 25%	ED: 0.0458 J/mm^2 T_b: 105℃	Zhu et al. 2015[34]
PP	Maximum tensile strength: 23.1 MPa Maximum elongation at break: 3.5%	ED: 0.0122 J/mm^2 T_b: 150℃	Flores Ituarte et al. 2018[31]
PP + 30 wt.% glass fiber	E_{11}: 1819 MPa E_{22}: 1245 MPa	ED: 0.0137-0.0205 J/mm^2 T_b: 115℃	Kleijnen et al. 2017[43]

2.3 PBF of Polyolefins: Future Directions

Researchers have been reasonably successful printing PP via PBF, but printing PE with mechanical properties equivalent to injection molded parts has been limited. To achieve IM mechanical properties for PE, researchers must understand how to control crystallization of the

polymer during printing. Understanding temperatures and heat flow in the powder bed during printing and connecting this behavior to crystallization kinetics is imperative to optimizing printed part properties. Further, researchers must spend more time printing parts with complex geometries since most current research is limited to printing 2.5D parts for mechanical testing as the ability to print these parts is necessary to fully utilize AM of polyolefins.

Developing metrics for rheological properties and crystallization rates necessary to make a polyolefin powder printable would be an invaluable aid for processing polyolefins via PBF. Exploration into controlling molecular weight, polymer architecture, copolymer content and nucleation additives would help further establish the properties necessary to make a polyolefin powder printable. Fundamental polymer science and understanding polymer physics is necessary to achieve these types of analysis, which means analysis tools outside of the printer must be employed. Extensional rheometry will help directly measure the viscosities pertinent to the PBF process, which will aid in modelling and understanding of PBF. Fast-scanning calorimetry (e.g., Flash DSC) can match cooling rates observed in the printer and give insight into how crystallization occurs during PBF. Using analysis tools that accurately mimic PBF is crucial to understanding the impact of fundamental properties on processing of polyolefins.

Powder production should be another area of future work. Optimization of powder production to not only achieve optimal particle size distributions and sphericity but also controlled morphology would greatly help PBF research of polyolefins. Research to increase powder production efficiency would help researchers more rapidly screen powders to understand the material properties necessary to make a powder processable. Additives such as flame retardants, stabilizers, and nano-fillers would all be valuable to try and include during the powder

production process since each of these additives increases the application space for parts made via PBF.

As discussed in the preceding sections, the non-isothermal thermal profiles, rapid crystallization kinetics, and formation of porous structure during the melt-based AM processing of polyolefins limits their widespread application. The presence of shear- or flow-induced crystallization effects can result in the nucleation of crystals that impede polymer chain diffusion across the interfacial welds. To optimize both PBF and MatEx of polyolefins it is necessary to develop a physics-based understanding of each polymer's processing and then employ this understanding to determine appropriate print conditions for each polymer. The focus of most studies in current literature is to investigate the effect of print parameters on print properties (process-structure-property relationships). However, the fundamental polyolefin properties and modifications that can enable successful processing in AM (structure-process-processing relationships) must be investigated.

2.4 References

[1] M. Schmid, Laser Sintering with Plastics: Technology, Processes, and Materials, Carl Hanser Verlag GmbH Co KG, 2018.

[2] C.A. Chatham, T.E. Long, C.B. Williams, A review of the process physics and material screening methods for polymer powder bed fusion additive manufacturing, Prog. Polym. Sci. 93 (2019) 68–95. https://doi.org/10.1016/j.progpolymsci.2019.03.003.

[3] J.C. Nelson, Selective laser sintering: a definition of the process and an empirical sintering model, PhD Thesis, University of Texas at Austin, 1993.

[4] E.D. Dickens Jr, B.L. Lee, G.A. Taylor, A.J. Magistro, H. Ng, Sinterable semi-crystalline powder and near-fully dense article formed therewith, US5342919A, 1994. https://patents.google.com/patent/US5342919A/en (accessed November 6, 2020).

[5] M. Schmid, A. Amado, K. Wegener, Materials perspective of polymers for additive manufacturing with selective laser sintering, J. Mater. Res. 29 (2014) 1824–1832. https://doi.org/10.1557/jmr.2014.138.

[6] J.W. Stansbury, M.J. Idacavage, 3D printing with polymers: Challenges among expanding options and opportunities, Dent. Mater. 32 (2016) 54–64. https://doi.org/10.1016/j.dental.2015.09.018.

[7] D. Drummer, K. Wudy, M. Drexler, Modelling of the aging behavior of polyamide 12 powder during laser melting process, in: AIP Publishing LLC, 2015: p. 160007.

[8] G.V. Salmoria, C.H. Ahrens, P. Klauss, R.A. Paggi, R.G. Oliveira, A. Lago, Rapid manufacturing of polyethylene parts with controlled pore size gradients using selective laser sintering, Mater. Res. 10 (2007) 211–214.

[9] J. Bai, B. Zhang, J. Song, G. Bi, P. Wang, J. Wei, The effect of processing conditions on the mechanical properties of polyethylene produced by selective laser sintering, Polym. Test. 52 (2016) 89–93. https://doi.org/10.1016/j.polymertesting.2016.04.004.

[10] G.R. Moore, D.E. Kline, Properties and processing of polymers for engineers, Prentice-Hall Inc 1984. (1984) 209.

[11] B. Hoelzel, Additive Manufacturing of HDPE Using Selective Laser Sintering, Master of Science Thesis, University of Oklahoma, 2019. https://shareok.org/handle/11244/319676 (accessed November 26, 2019).

[12] K.A. Hing, S.M. Best, K.E. Tanner, W. Bonfield, P.A. Revell, Biomechanical assessment of bone ingrowth in porous hydroxyapatite, J. Mater. Sci. Mater. Med. 8 (1997) 731–736. https://doi.org/10.1023/A:1018500309969.

[13] M.M. Savalani, L. Hao, R.A. Harris, Evaluation of CO2 and Nd:YAG Lasers for the Selective Laser Sintering of HAPEX®, Proc. Inst. Mech. Eng. Part B J. Eng. Manuf. 220 (2006) 171–182. https://doi.org/10.1243/095440505X32986.

[14] L. Hao, M.M. Savalani, Y. Zhang, K.E. Tanner, R.A. Harris, Selective Laser Sintering of Hydroxyapatite Reinforced Polyethylene Composites for Bioactive Implants and Tissue Scaffold Development, Proc. Inst. Mech. Eng. [H]. 220 (2006) 521–531. https://doi.org/10.1243/09544119JEIM67.

[15] L. Hao, M.M. Savalani, Y. Zhang, K.E. Tanner, R.A. Harris, Effects of material morphology and processing conditions on the characteristics of hydroxyapatite and high-density polyethylene biocomposites by selective laser sintering, Proc. Inst. Mech. Eng. Part J. Mater. Des. Appl. 220 (2006) 125–137. https://doi.org/10.1243/14644207JMDA92.

[16] Y. Zhang, L. Hao, M.M. Savalani, R.A. Harris, K.E. Tanner, Characterization and dynamic mechanical analysis of selective laser sintered hydroxyapatite-filled polymeric composites, J. Biomed. Mater. Res. A. 86A (2008) 607–616. https://doi.org/10.1002/jbm.a.31622.

[17] Y. Zhang, L. Hao, M.M. Savalani, R.A. Harris, L. Di Silvio, K.E. Tanner, In vitro biocompatibility of hydroxyapatite-reinforced polymeric composites manufactured by selective laser sintering, J. Biomed. Mater. Res. Part Off. J. Soc. Biomater. Jpn. Soc. Biomater. Aust. Soc. Biomater. Korean Soc. Biomater. 91 (2009) 1018–1027.

[18] G.V. Salmoria, E.A. Fancello, C.R. Roesler, F. Dabbas, Functional graded scaffold of HDPE/HA prepared by selective laser sintering: microstructure and mechanical properties, Int. J. Adv. Manuf. Technol. 65 (2013) 1529–1534.

[19] G.V. Salmoria, F.E. Vieira, E.A. Muenz, I.M. Gindri, M.S. Marques, L.A. Kanis, Additive Manufacturing of PE/fluorouracil/progesterone intrauterine device for endometrial and ovarian cancer treatments, Polym. Test. 71 (2018) 312–317. https://doi.org/10.1016/j.polymertesting.2018.09.023.

[20] G.V. Salmoria, F.E. Vieira, G.B. Ghizoni, I.M. Gindri, L.A. Kanis, Additive Manufacturing of PE/Fluorouracil Waffles for Implantable Drug Delivery in Bone Cancer Treatment, Int. J. Eng. Res. Sci. 3 (2017) 62–70.

[21] J.T. Rimell, P.M. Marquis, Selective laser sintering of ultra high molecular weight polyethylene for clinical applications, J. Biomed. Mater. Res. Off. J. Soc. Biomater. Jpn. Soc. Biomater. Aust. Soc. Biomater. Korean Soc. Biomater. 53 (2000) 414–420.

[22] R.D. Goodridge, R.J.M. Hague, C.J. Tuck, An empirical study into laser sintering of ultra-high molecular weight polyethylene (UHMWPE), J. Mater. Process. Technol. 210 (2010) 72–80. https://doi.org/10.1016/j.jmatprotec.2009.08.016.

[23] Y. Khalil, A. Kowalski, N. Hopkinson, Influence of energy density on flexural properties of laser-sintered UHMWPE, Addit. Manuf. 10 (2016) 67–75. https://doi.org/10.1016/j.addma.2016.03.002.

[24] Y. Khalil, A. Kowalski, N. Hopkinson, Influence of laser power on tensile properties and material characteristics of laser-sintered UHMWPE, Manuf. Rev. 3 (2016) 15. https://doi.org/10.1051/mfreview/2016015.

[25] Y. Khalil, N. Hopkinson, A. Kowalski, J.P.A. Fairclough, Characterisation of UHMWPE Polymer Powder for Laser Sintering, Materials. 12 (2019) 3496. https://doi.org/10.3390/ma12213496.

[26] T. Ullsperger, Y.L. Wencke, B. Yürekli, G. Matthäus, M. Rettenmayr, G.A. Luinstra, S. Nolte, Laser powder bed fusion of ultra-high molecular weight polyethylene (UHMWPE) using near-infrared ultrashort laser pulses, Mater. Des. 210 (2021) 110048. https://doi.org/10.1016/j.matdes.2021.110048.

[27] X. Zhu, Q. Yang, Sintering the feasibility improvement and mechanical property of UHMWPE via selective laser sintering, Plast. Rubber Compos. 49 (2020) 116–126. https://doi.org/10.1080/14658011.2020.1718321.

[28] K.M. Kozlovsky, Additive Manufacturing of Ultra-High Molecular Weight Polyethylene under Applied External Pressure, Ph.D., University of Notre Dame, n.d. https://www.proquest.com/docview/2322186293/abstract/252693F78D224297PQ/1 (accessed April 26, 2022).

[29] Y. Zhao, Q. Yang, H. Ma, P. Wu, Y. Huang, P. Gong, An investigation of post treatment on properties and structure of ultrahigh molecular weight polyethylene parts prepared by selective laser sintering for biomedical application, Polym. Adv. Technol. 31 (2020) 1484–1495. https://doi.org/10.1002/pat.4878.

[30] C.W.M. Bastiaansen, H.E.H. Meyer, P.J. Lemstra, Memory effects in polyethylenes: influence of processing and crystallization history, Polymer. 31 (1990) 1435–1440. https://doi.org/10.1016/0032-3861(90)90147-Q.

[31] I. Flores Ituarte, O. Wiikinkoski, A. Jansson, Additive Manufacturing of Polypropylene: A Screening Design of Experiment Using Laser-Based Powder Bed Fusion, Polymers. 10 (2018) 1293. https://doi.org/10.3390/polym10121293.

[32] L. Fielder, Evaluation of Polypropylene powder grades in consideration of the laser sintering process ability, J. Plast. Technol. 3 (2007) 34–39.

[33] T. Reinhardt, A. Martha, G. Witt, P. Köhler, Preprocess-Optimization for Polypropylene Laser Sintered Parts, Comput.-Aided Des. Appl. 11 (2014) 49–61. https://doi.org/10.1080/16864360.2013.834138.

[34] W. Zhu, C. Yan, Y. Shi, S. Wen, J. Liu, Y. Shi, Investigation into mechanical and microstructural properties of polypropylene manufactured by selective laser sintering in comparison with injection molding counterparts, Mater. Des. 82 (2015) 37–45. https://doi.org/10.1016/j.matdes.2015.05.043.

[35] B. Caulfield, P.E. McHugh, S. Lohfeld, Dependence of mechanical properties of polyamide components on build parameters in the SLS process, J. Mater. Process. Technol. 182 (2007) 477–488. https://doi.org/10.1016/j.jmatprotec.2006.09.007.

[36] A. Wegner, New Polymer Materials for the Laser Sintering Process: Polypropylene and Others, Phys. Procedia. 83 (2016) 1003–1012. https://doi.org/10.1016/j.phpro.2016.08.105.

[37] A. Amado, K. Wegener, M. Schmid, G. Levy, Characterization and modeling of non-isothermal crystallization of Polyamide 12 and co-Polypropylene during the SLS process, in: 5th Int. Polym. Moulds Innov. Conf., Ghent, 2012.

[38] L.J. Tan, W. Zhu, K. Sagar, K. Zhou, Comparative study on the selective laser sintering of polypropylene homopolymer and copolymer: processability, crystallization kinetics, crystal phases and mechanical properties, Addit. Manuf. 37 (2021) 101610. https://doi.org/10.1016/j.addma.2020.101610.

[39] C.A. Chatham, A. Das, T.E. Long, M.J. Bortner, C.B. Williams, Ageing of PBF-Grade Poly(Phenylene Sulfide) Powder and its Effect on Critical Printability Properties, Macromol. Mater. Eng. 306 (2021) 2000599. https://doi.org/10.1002/mame.202000599.

[40] A. Wegner, T. Ünlü, Powder Life Cycle Analyses for a New Polypropylene Laser Sintering Material, in: Proc. 27th Annu. Int. Solid Free. Fabr. Symp. – Addit. Manuf. Conf., Austin, Texas, 2016: pp. 834–846.

[41] F.M. Mwania, M. Maringa, K. van der Walt, Powder Characterization for a New Selective Laser Sintering Polypropylene Material (Laser PP CP 60) after Single Print Cycle Degradation, Int. J. Eng. Res. Technol. 13 (2020) 3342. https://doi.org/10.37624/IJERT/13.11.2020.3342-3358.

[42] F.M. Mwania, M. Maringa, J.G. van der Walt, Investigating the Recyclability of Laser PP CP 75 Polypropylene Powder in Laser Powder Bed Fusion (L-PBF), Polymers. 14 (2022) 1011. https://doi.org/10.3390/polym14051011.

[43] R.G. Kleijnen, J.P.W. Sesseg, M. Schmid, K. Wegener, Insights into the development of a short-fiber reinforced polypropylene for laser sintering, AIP Conf. Proc. 1914 (2017) 190002. https://doi.org/10.1063/1.5016791.

[44] R.G. Kleijnen, M. Schmid, K. Wegener, Nucleation and impact modification of polypropylene laser sintered parts, AIP Conf. Proc. 1779 (2016) 100004. https://doi.org/10.1063/1.4965572.

[45] K. Wudy, M. Hinze, F. Ranft, D. Drummer, W. Schwieger, Selective laser sintering of zeolite filled polypropylene composites: Processing and properties of bulk adsorbents, J. Mater. Process. Technol. 246 (2017) 136–143.

[46] D. Drummer, M. Medina-Hernández, M. Drexler, K. Wudy, Polymer Powder Production for Laser Melting Through Immiscible Blends, Procedia Eng. 102 (2015) 1918–1925. https://doi.org/10.1016/j.proeng.2015.01.332.

[47] S.-J. Wang, J.-Y. Liu, L.-Q. Chu, H. Zou, S.-J. Zhang, C.-J. Wu, Preparation of polypropylene microspheres for selective laser sintering via thermal-induced phase separation: Roles of liquid–liquid phase separation and crystallization, J. Polym. Sci. Part B Polym. Phys. 55 (2017) 320–329.

[48] L. Fang, Y. Wang, Y. Xu, Preparation of polypropylene powder by dissolution-precipitation method for selective laser sintering, Adv. Polym. Technol. 2019 (2019) 5803895.

[49] L.J. Tan, W. Zhu, K. Zhou, Development of organically modified montmorillonite/polypropylene composite powders for selective laser sintering, Powder Technol. 369 (2020) 25–37. https://doi.org/10.1016/j.powtec.2020.05.005.

[50] C. Schäfer, S.P. Meyer, T.A. Osswald, A novel extrusion process for the production of polymer micropellets, Polym. Eng. Sci. 58 (2018) 2264–2275. https://doi.org/10.1002/pen.24847.

[51] S. Fanselow, S.E. Emamjomeh, K.-E. Wirth, J. Schmidt, W. Peukert, Production of spherical wax and polyolefin microparticles by melt emulsification for additive manufacturing, Chem. Eng. Sci. 141 (2016) 282–292. https://doi.org/10.1016/j.ces.2015.11.019.

[52] X. Gong, X. Gao, N. Yu, D. Zhang, L. Tan, J. Li, Characterization of thermally treated polypropylene powders with wide sintering window for powder bed fusion of polymers, Polym. Test. 96 (2021) 107078. https://doi.org/10.1016/j.polymertesting.2021.107078.

[53] J.S.G. Bonilla, T. Szymczak, X. Zhou, S. Schrüfer, M.A. Dechet, P. Schmuki, D.W. Schubert, J. Schmidt, W. Peukert, A. Bück, Improving the coloring of polypropylene materials for powder bed fusion by plasma surface functionalization, Addit. Manuf. 34 (2020) 101373. https://doi.org/10.1016/j.addma.2020.101373.

Chapter 3: Powder bed fusion additive manufacturing of ultra-high molecular weight polyethylene using a novel laser scanning strategy

This chapter has been published by *Additive Manufacturing* and is presented in the published form.

J.S. Bryant, M.J. Bortner, C.B. Williams, Powder bed fusion additive manufacturing of ultra-high molecular weight polyethylene using a novel laser scanning strategy, *Additive Manufacturing*. (2023) 103885. https://doi.org/10.1016/j.addma.2023.103885.

3.1 Abstract

Current processing routes (ram extrusion, compression molding, and sheet molding) for fabricating ultra-high molecular weight polyethylene (UHMWPE) greatly limit the geometries that can be processed. Due to these limitations, additive manufacturing (AM) of UHMWPE has long been a goal, as the ability to fabricate complex geometries from this polymer could open new applications not possible using these traditional processing routes. UHMWPE's especially high wear properties also fill a gap in current AM materials. Powder bed fusion (PBF) processing of UHMWPE is challenging due to the high melt viscosity of UHMWPE and melt explosion, which occurs during melting of UHMWPE and causes powder particle expansion during scanning and leads to powder recoating failure.

This work demonstrates a novel scan strategy for PBF of UHMWPE, in which layers are scanned using large (1.2 mm) hatch spacings. Scanning with a large hatch spacing reduces conduction between scanlines and distributes energy so as to encourage coalescence without melt explosion. UHMWPE powder is only partially melted during this scanning approach, which causes light coalescence between particles and avoids z-direction expansion that disrupts powder

recoating. The lightly coalesced “green” parts are brittle and are densified by thermally post-processing them in the melt. Parts retain their shape during post-processing due to the high melt viscosity of UHMWPE. Using this combination of a novel scan strategy with large hatch spacing and a post-processing thermal treatment, a 3000 kDa UHMWPE was successfully printed, demonstrating the first reported multi-layer PBF of UHMWPE with complex geometries.

3.2 AM of UHMWPE state of the art

Ultra-high molecular weight polyethylene (UHMWPE) is a polymer that is notable for its high wear properties and utility in biomedical applications [1,2]. Traditional UHMWPE processing employs a combination of time, temperature and pressure to form highly densified, solid parts which can be milled into the desired shape for an end-use application. It has traditionally been processed using compression molding, ram extrusion or sheet molding due to its especially high melt viscosity [3]. However, each of these processes limits conceivable part geometries, and takes many hours to complete. Additive manufacturing (AM) provides a route to obtain more complex geometries in existing applications while opening the door to additional functionalities and new markets.

Though PBF of UHMWPE has previously been explored, there are still significant gaps in the research and realizing part performance expected for this polymer. PBF of UHMWPE was first explored by Rimell et al. In this research, only single lines were scanned and characterized in a custom PBF setup. Degradation was observed and increased with energy input. No layers or complex parts were printed [4] . Later, research conducted by Goodridge et al. showed the first successful printing of UHMWPE multi-layer parts via PBF. However, only flexural strength was reported, and the resulting value was only 0.52 ± 0.2 MPa [5]. Khalil et al. followed this research and printed UHMWPE at energy densities ranging from 0.016-0.032 J/mm^2. They tested flexural

strength as well as tensile strength and reported values of 2.12 ± 0.05 MPa and 2.42 ± 0.20 MPa respectively [6,7]. This value is approximately 6% of the tensile strength at break reported by Celanese for the grade of UHMWPE used in their study when processed using compression molding. Kozlovsky printed UHMWPE using a custom PBF system that applied pressure to the powder bed during scanning and produced multilayer parts that were tested in compression. The true compressive yield strength of these printed parts ranged from 4.4-14 MPa [8]. Despite this progress, the current research has not demonstrated consistent printing of complex parts using PBF, nor have the printed results matched the properties attained for this polymer using traditional processing methods.

Fused filament fabrication (FFF), has also been used to explore printing UHMWPE. The approach in that process has been to blend UHMWPE at different concentrations into other matrix materials— mostly polypropylene and polyethylene—and print the resulting composite [9–14]. Since these materials were composites rather than neat UHMWPE, the results in this work will not be compared to them.

3.3 Challenges in powder bed fusion of UHMWPE

3.3.1 Overview of polymer powder bed fusion

Laser-based polymer powder bed fusion (PBF) is an additive manufacturing (AM) process in which polymer particles (20-100 μm in diameter) are selectively melted using scanning infrared (typically from a CO_2 laser) irradiation under an inert nitrogen atmosphere. Powder is supplied to the build area during powder recoating using a counter-rotating roller or recoating blade [1]. The most common processing parameters for PBF are: laser power, beam velocity, bed temperature, and hatch spacing, which is the distance between the center line of parallel scanlines. Hatch

spacing is typically set to a value lower than the laser diameter, to induce scanline overlap which encourages densification and entanglement of polymer chains between scanlines.

In PBF the laser rasters across the print area, selectively melting the polymer to form layers in the specified shape. Upon energy deposition by the laser, the polymer powder melts, coalesces, and then cools and crystallizes. Semicrystalline thermoplastics are the most processed materials in PBF and, during printing, the polymer is held at a temperature slightly below its onset of melting temperature to retard crystallization, which limits warpage. However, being in this temperature range does not mean that a polymer won't crystallize (which could cause warpage) during cooling and at the bed temperature [1]. Warpage during printing can occur due to stresses developed during crystallization of the polymer during cooling and can be mitigated through changes in processing parameters, such as bed and feed temperatures or laser parameters [1]. Warpage of a printed layer during cooling often leads to sample shifting during recoating.

3.3.2 UHMWPE's high melt viscosity

No shear is applied during the PBF process, which makes a polymer's zero shear viscosity (η_0) the relevant viscosity for processing [15]. As a point of comparison, at 200° C, multiple researchers have measured polyamide 12 (the most common PBF-processed material) to have a η_0 of less than 10^3 Pa·s [16,17]. UHMWPE has been reported to show a η_0 as high as 10^8 Pa·s at 190° C [18]. This high viscosity is in large part due to the high molecular weight (MW) of the UHMWPE. First proposed by Fox & Flory, and later measured for polyethylene by Peticolas & Watkins, the zero-shear viscosity of polyethylene will scale with MW raised to the 3.4 power [19,20]. Surface tension, on the other hand, increases with molecular weight until it reaches a maximum value [21]. This five magnitude difference in η_0 can prove challenging in PBF because coalescence depends on having sufficient surface energy to overcome the resistance of a polymer's

melt viscosity to coalescence [15]. Limited coalescence during PBF will result in a low density printed part with significant porosity, which limits the part's mechanical properties [22].

3.3.3 Z-direction expansion of UHMWPE upon energy deposition

Initial printing attempts of the UHMWPE powder used in this research showed a unique expansion of the scanned layer in the z-direction. Often, when cooling of a scanned layer is not properly controlled, the edges of the layer will curl upwards during cooling, which disrupts powder recoating. Instead of curling, the entire scanned surface of the UHMWPE expanded uniformly. This growth led layers to be pushed out of position by the roller during powder recoating, which made printing multilayer parts with controlled geometries impossible.

Though this phenomenon has not been directly mentioned in other literature on PBF of UHMWPE, other researchers have given evidence of this expansion being a consistent problem during PBF of this polymer. Goodridge et al. used a bed temperature within the melting endotherm of their grade of UHMWPE. In their research, they show that the powder uniformly expanded across the entire print bed during printing. Their feed piston, which was held at a temperature below the melting endotherm for their powder, showed no such expansion [5]. Khalil et al. make no note of expansion during printing; however, their parts showed z-direction thicknesses that were up to 3 mm greater than the designed thickness for their parts, which suggests a similar z-direction expansion during printing [7]. Kozlovsky shows images of single layer prints in which the scanned area is raised above the rest of the print bed [8]. Each of these results suggest that z-direction layer growth is a consistent problem when processing UHMWPE via PBF. However, no explanation for this behavior has been proposed. To achieve consistent printing of UHMWPE this behavior must first be explained and then, by understanding the behavior, a solution can be proposed to mitigate the expansion during printing.

3.3.4 Melt explosion in UHMWPE

UHMWPE has a long history of being studied using fundamental polymer analysis techniques. This type of research can prove to be an invaluable complement to AM research, especially with difficult to process materials such as UHMWPE. Initial results found by Sadler et al. showed that, in solution-crystallized UHMWPE, the radius of gyration (R_g) did not scale with molecular weight (MW) as expected. Rather than having $R_g \propto MW^{\alpha}$ (where α is 0.5 or greater), Sadler et al. found an α value of 0.1 for their UHMWPE sample, thus as MW increases, there is a smaller increase in R_g than would be expected. This result led Sadler et al. to conclude that polymer chains in their samples showed minimal entanglement with each other [23]. Later research found that upon melting, polyethylene chains changed from their smaller than expected R_g to their melt R_g almost instantaneously. This change occurred at timescales much shorter than reptation theory would predict for the molecular weight of polyethylene tested [24]. DeGennes et al. further explored this research topic in UHMWPE and described the phenomenon as "explosion upon melting," [25]. In this work, the authors will discuss this phenomenon using the name, "melt explosion." In their work exploring melt explosion during sintering of UHMWPE powder, Deplancke et al. concluded that chain interdiffusion between particles was controlled by melt explosion rather than reptation [26]. This work elucidated the role of melt explosion during processing of UHMWPE and suggests that chain interdiffusion between powder particles could occur during energy deposition and melting in the PBF process. Further research by Deplancke et al. demonstrated that melt explosion during processing was critical to achieving significant entanglements between particles during the sintering process [27].

It is hypothesized that the z-direction growth observed during printing of UHMWPE via PBF is caused by melt explosion. The neat polymer powder undergoes melting during laser scanning,

which causes chains to move farther than would be expected over the timescale of heating during scanning. Once the chains have moved due to melt explosion, they are too viscous to continue moving significantly and crystallize at a much greater volume.

3.4 Use of scan strategy to mitigate z-direction growth during PBF of UHMWPE

It is hypothesized that this behavior can be mitigated by a novel scan strategy. Specifically, we propose using a larger than usual hatch spacing (hatch spacing larger than the laser diameter), to limit conduction between individual scanlines, and yield greater control of temperature, and therefore melting of the polymer, during printing. It is hypothesized that powder scanned with appropriate process parameters can undergo enough melting to lightly coalesce powder together, but not enough melting to show the macroscopic z-direction growth that disrupts powder recoating for subsequent layers. In this proposed process approach, the scanning approach would yield a "green part" with defined geometry and enough strength to be removed from the printer and then undergo thermal post-processing to densify the sample. Here, PBF processing would be used as a method to set the shape of the final part, but not to develop its final properties.

Thermal post-processing of UHMWPE at temperatures above its melting endotherm to encourage diffusion and densification while maintaining part geometry would be possible due to the exceptionally high melt viscosity of UHMWPE. Using a two-step process-chain featuring thermal post-processing is usually not possible for PBF, though it is common in other AM processes such as vat photopolymerization, direct ink-write, and binder jetting [28–32]. Currently, materials printed via PBF have insufficient viscosities to maintain shape during a thermal post-processing step. This method would remove the limitation of needing mechanical properties to be fully developed during printing.

Figure 3.1 displays the powder particles at each step of the proposed printing process-chain.

- Step 1: powder particles are spread during powder recoating; they are loosely touching.
- Step 2: a fraction of powder particles is lightly coalesced by non-overlapping laser scanlines (shown in red). This step shows the printed green part where some of the particles have not undergone any melting and are trapped between scanlines.
- Step 3: samples are thermally post-processed, which densifies them. They show low amounts of porosity, which would yield mechanical properties close to that expected for UHMWPE.

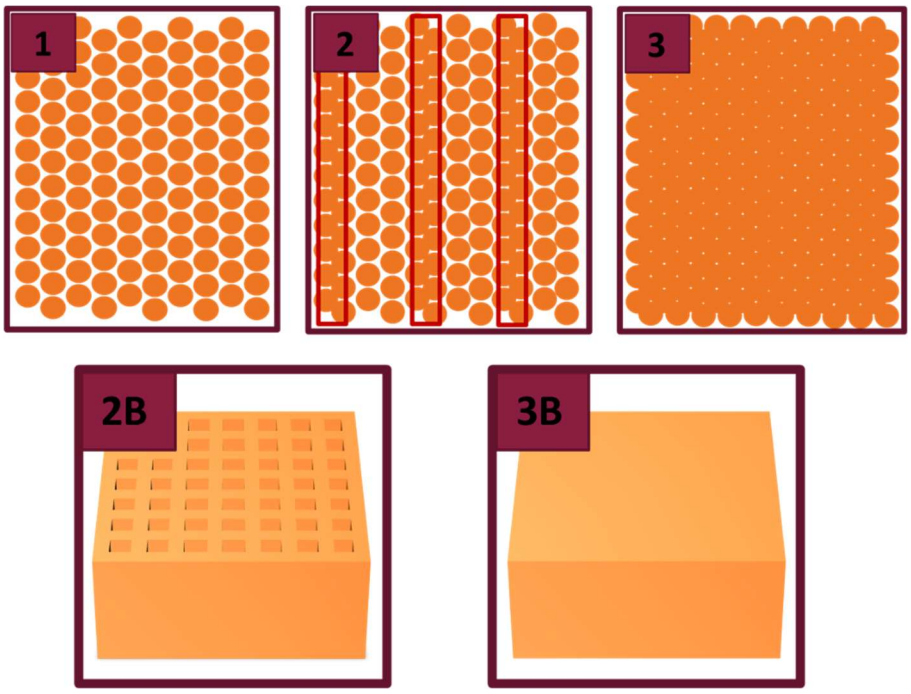

Figure 3.1 Depicts powder particles at each step of the proposed printing process. In step 1, powder is loose and unconnected. In step 2, some powder has been lightly coalesced and has formed a green part. Step 3 shows the hypothesized state of the final part that has been densified through thermal post-processing. 2B and 3B are three dimensional representations of steps 2 and 3 respectively for printing a cube. All holes in the part shown in 2B are filled with loose powder

that will coalesce with the scanned scaffold during thermal post-processing to produce 3B. 2B shows both the high hatch spacing infill and the contour scan which creates a shell at the outer edges of the part.

3.5 Materials and Methods

3.5.1 Overview

The goal of this work was to determine a suitable processing chain that would enable PBF of UHMWPE. All characterization was conducted to evaluate the hypothetical printing workflow proposed to avoid z-direction expansion during laser scanning (Figure 3.1). Methods are used to determine the appropriate processing parameters to successfully print single layers and then print multi-layer green parts. Green parts are evaluated to understand their structure and how their process-structure relationship enabled successful printing. Thermal post-processing parameters were evaluated and post-processed part properties were characterized.

3.5.2: Characterization of neat powder

3.5.2.1: Molecular weight

Braskem provided a 3000 kDa UHMWPE powder that was used in this research. MW of printed samples was not analyzed. UHMWPE chains are at too high a MW for size-exclusion chromatography (SEC) measurements. As such, empirical observations of yellowing or change of opacity in the material during printing or post-processing were used to determine if MW loss occurred.

3.5.2.2: Particle analysis

Received powders were analyzed via a Horiba LA-950 laser diffraction powder size analyzer to quantify particle size for the powder. Water was used as the liquid medium for this experiment and d10, d90, and mean particle size were determined from the particle size distribution. The neat powder morphology also was analyzed using scanning electron microscopy (SEM). Samples were sputter coated with a 5 nm thick Iridium (Ir) coating and measured at 4 kV. In addition, static and tapped density measurements were conducted and the Hausner ratio was calculated from these values to predict powder flowability.

3.5.2.3: Differential scanning calorimetry (DSC) of powder

Differential scanning calorimetry (DSC) was performed using a TA Instruments Q2000 to understand the morphology and phase transition temperatures of the neat powder. Samples were heated at 10 °C/min from 25-180 °C. The first heat was chosen to assess the material because this measurement aligns with the morphology of the powder as it enters the printer. Degree of crystallinity was calculated using a heat of fusion of 288 J/g for polyethylene [33].

3.5.3: Printed part analysis

3.5.3.1: PBF system

The polymer powder bed fusion machine used for this research was a Prodways Promaker P2000 HT manufactured by Farsoon. This machine is equipped with a 60 W, CO_2 laser that has a beam diameter of 500 μm and wavelength of 10.6 μm. This machine has controllable laser power, beam velocity, and hatch spacing. Values for these parameters can be set for both infill and contour scanning (Figure 3.2). Contour scanning is a scanline that occurs at the edges of each layer and adjacent, unscanned powder.

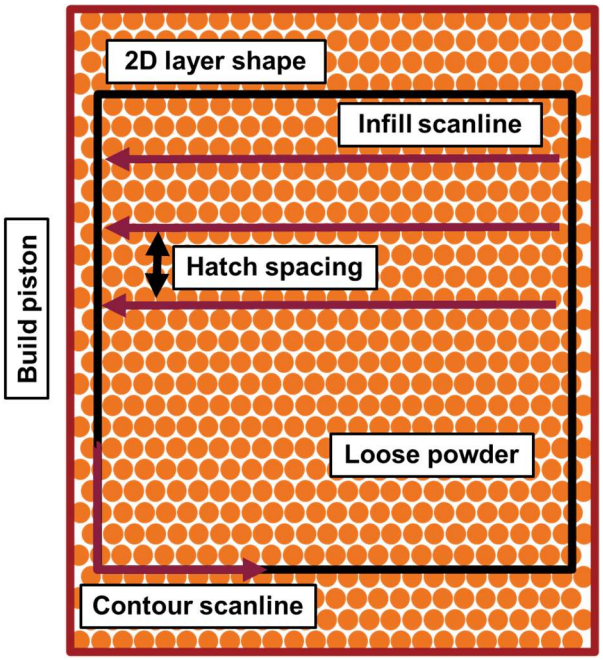

Figure 3.2 A 2D representation of the PBF print process which shows the powder bed, a single layer 2D shape that will be scanned, and representations of scanlines and hatch spacing.

3.5.3.2: Process parameter selection for novel scan strategy

PBF process parameters such as laser power and hatch spacing were systematically altered to experimentally identify a processing window for this polymer. In situ IR-thermography of powder surface temperature was captured using a Micro Epsilon TIM 640 camera to track how different processing parameters changed the peak temperature measured during scanning. Peak temperature was chosen because this value represents how much powder melting occurred during scanning (higher temperature = more melting). Temperature measurements of scanned powder were coupled with observations of z-direction expansion at different sets of process parameters to determine process parameters that would limit melting and therefore z-direction expansion such that multi-layer parts were printable.

3.5.3.3: Thermal post-processing

Printed green parts (featuring trapped powder in a scanned scaffold) were post-processed under N_2 at 180, 200 and 220 °C for 2 h in a Thermo Fisher Lindberg Blue M vacuum oven. These temperatures were chosen to be above the full melting endotherm of the UHMWPE powder, but low enough to reduce the risk of molecular weight loss during post-processing. Two hours was chosen to enable a sample to equilibrate at the set temperature while limiting time in the melt to limit the chance of molecular weight loss.

3.5.3.4: Part density, printed part dimensions and shrinkage

Density of PBF samples are typically measured using Archimedes method by measuring part mass with a balance and finding part volume with a buoyant force measurement [34]. Because the densities of the samples printed in this research were lower than the common liquids used for this method (water, ethanol), the buoyant force could not be calculated. Instead, density was determined by measuring printed 7 x 7 x 7 mm cubes. Density was calculated by dividing the measured sample mass by the calculated sample volume (measured by digital calipers). Printed dimensions of green parts were compared to their intended dimensions. Samples dimensions were measured before and after post-processing to determine shrinkage and post-processed density.

3.5.3.5: Tensile testing

A tensile specimen adapted from an ASTM D638 type IV bar was designed to enhance the robustness of printed tensile specimens. The standard size was modified as shown in Figure 3.3. Samples were tested at a strain rate of 5 mm/min on an Instron 5944 tensile tester with a 2 kN load cell.

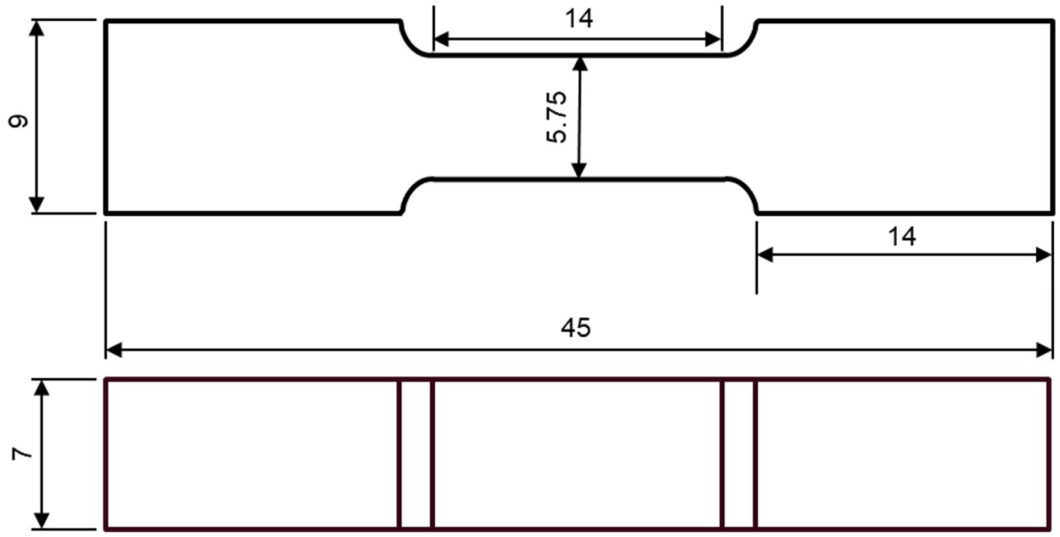

Figure 3.3 Depicts the dimensions of the adapted tensile bar used for testing. All dimensions are in millimeters.

3.5.3.6: Scanning electron microscopy

Fracture surfaces of pulled tensile specimens were analyzed using scanning electron microscopy (SEM). Samples were sputter coated with a 5 nm thick Iridium (Ir) coating and measured at 4 kV. This method helped to qualitatively assess the level of densification of the sample and evaluate how the sample fractured during tensile testing.

3.5.3.7: Differential scanning calorimetry (DSC) of printed parts

Differential scanning calorimetry (DSC) was performed using a TA Instruments Q2000 to understand the morphology of the printed green parts and parts after post-processing. These results elucidate how much melting occurred in the green part and the degree of crystallinity in printed parts. Samples were heated at 10 °C/min from 25-180 °C. Degree of crystallinity was calculated using a heat of fusion of 288 J/g for polyethylene [33].

3.6: Results/Discussion

3.6.1: Characterization of neat powder

Particle size analysis (Figure 3.4) showed the powder particles had an average particle size of 73 µm, d10 of 42 µm and a d90 of 103 µm, which are primarily within the 45-90 µm range suggested by Schmid et al. for good flowability in PBF [35].

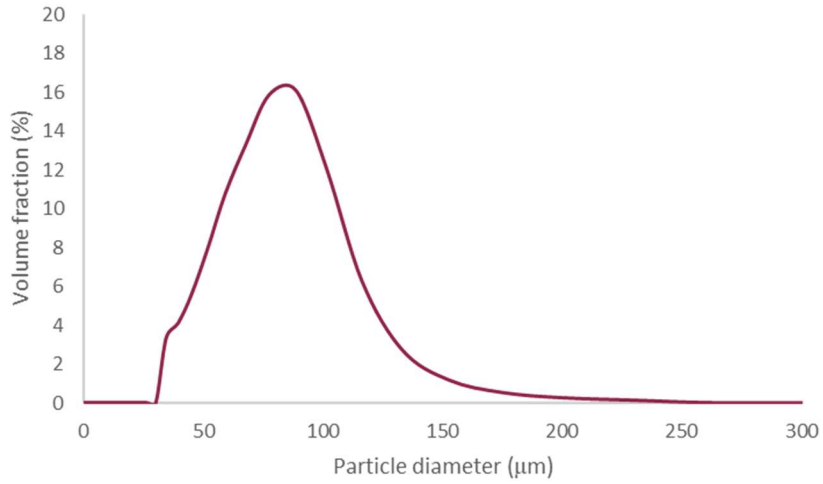

Figure 3.4 the particle size distribution shows the majority of particles are below 100 µm. No particles below 30 µm are present.

SEM of the powder (Figure 3.5) showed the powder particles are fairly spherical and rounded without sharp edges. Particles display some rounded surfaces and some nodules, which form during synthesis of the UHMWPE, on their surface. The static density of the neat powder was 0.477 ± 0.003 g/cm^3. The tapped density of the powder was 0.569 ± 0.002 g/cm^3. Together these values yield a Hausner ratio of 1.19, which is less than 1.25 and therefore predicts good flowability of the powder [15].

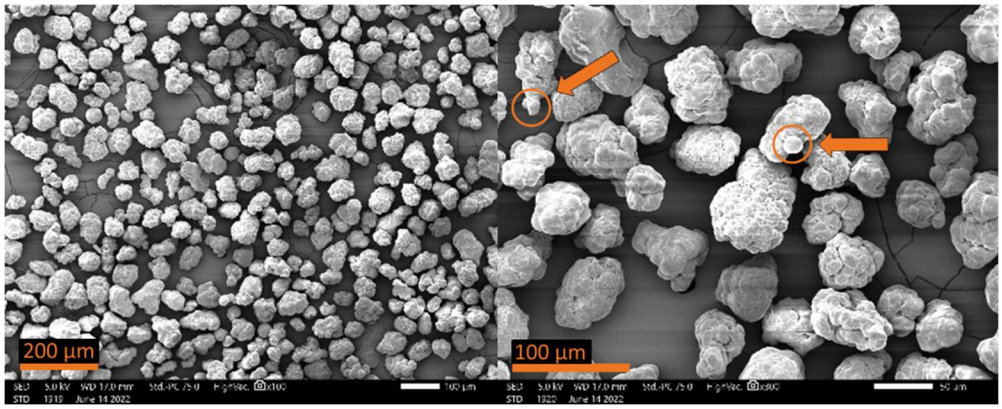

Figure 3.5 neat powder is reasonably spherical and edges are rounded, which suggests good flowability. Some powder particles show nodules on their surface (circled above), but no especially angular features.

A first heat DSC measurement of the neat powder shows a peak melting temperature ($T_{m,peak}$) of 139 °C. The onset of melting ($T_{m,onset}$) occurs at 123.5 °C. A first cooling DSC measurement of the same powder shows an onset of crystallization ($T_{c,onset}$) at 123.5 °C and crystallization peak ($T_{c,peak}$) at 119.5 °C (Figure 3.6).

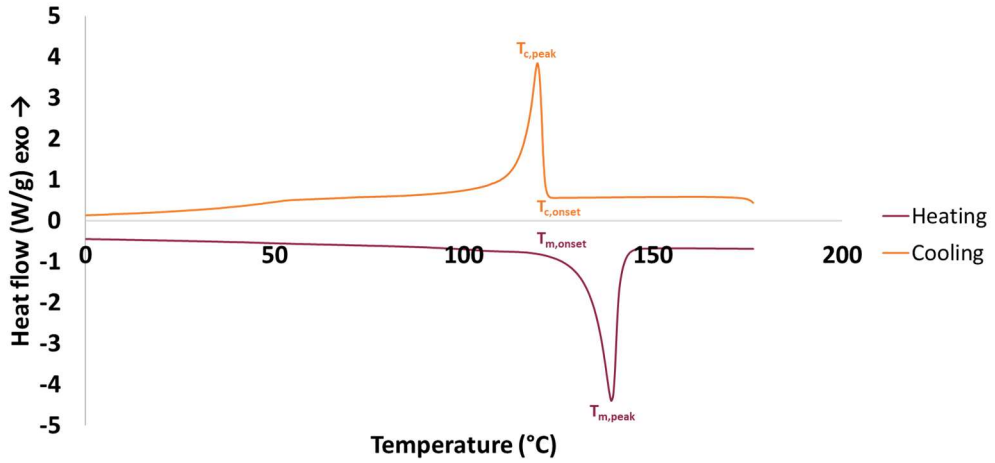

Figure 3.6 DSC of first heat and first cool of the neat UHMWPE powder.

3.6.2: Determination of print parameters for novel scan strategy

To reduce powder melting via conduction from a scanned area, and therefore z-direction expansion, all temperatures in the printer were set to 100° C, which is 20° C below the onset of melting for the polymer. Printing at this temperature created a larger barrier to melting since the powder would have to be heated up significantly more than is commonly used for bed temperatures in PBF (usually only 5-10° C below onset of melting).

To determine the energy input necessary to cause coalescence of individual scanlines without significant z-direction expansion, single layer scans of 20 x 20 mm squares were printed. These layers were printed with no infill and a single contour scan. Having a contour scan with no infill yields a single scanline square, which connects to itself and is therefore easier to remove from the printer. Samples were scanned with laser powers of 10-60 W (in 10 W increments) and a constant beam velocity of 1000 mm/s. Samples were manually evaluated to see if coalescence occurred and visually inspected to determine if expansion occurred relative to the unscanned powder in the build area.

For each sample where coalescence occurred (40-60 W), the coalesced scanline was very fragile and could be reduced to powder by hand. The results of this experiment are detailed in Table 3.1. A laser power of 50 W was determined to be the best option for printing samples at this beam velocity because samples scanned at this power showed coalescence without z-direction expansion.

Table 3.1 Samples showed a shift in behavior at 40 W to begin showing coalescence. At 60 W, the coalescence was sufficient to cause expansion of the scanline as well. All samples were scanned at 1000 mm/s.

Laser power (W)	Was coalescence observed? (Yes/No)	Was expansion observed? (Yes/No)
10	No	N/A
20	No	N/A
30	No	N/A
40	Yes	No
50	Yes	No
60	Yes	Yes

After an appropriate laser power was determined, the hatch spacing for a layer needed to be chosen. Hatch spacings of 0.1-0.3 mm are common in PBF and have been used to print a variety of polymers ranging from polycarbonate to PEEK [36,34,37–40]. These hatch spacing values are smaller than the diameter of the laser in PBF, usually 500 µm, which leads to overlap of scanlines during scanning. To ensure coalescence of individual scanlines without conduction between scanlines causing melt explosion, single layer samples (20 x 20 mm squares) were scanned at 50 W, 1000 mm/s and hatch spacings ranging from 0.3-1.8 mm in 0.3 mm increments.

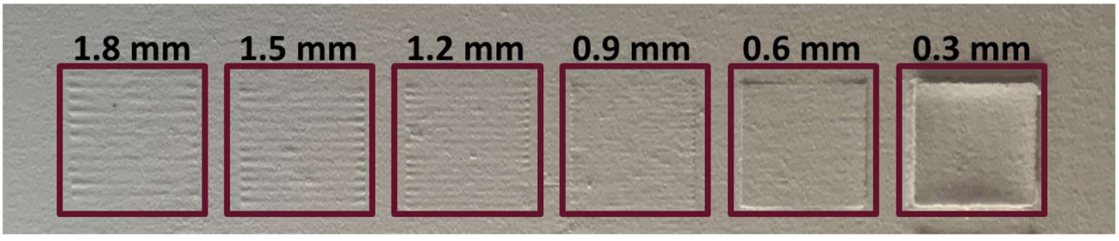

Figure 3.7 Changes in hatch spacing will determine the amount of conduction between individual scanlines. Lower hatch spacings have more conduction and result in greater melting of the powder

and z-direction expansion and shown in the samples printed at 0.3-0.9 mm hatch spacings. Higher hatch spacings lead to individually defined scanlines.

At hatch spacings of 0.3-0.9 mm, conduction between scanlines led to expansion of the layer (Figure 3.7). Hatch spacings of 1.2-1.8 mm yielded a layer of individual scanlines (scanned horizontally) that showed no significant z-direction expansion. The amount of z-direction expansion is directly related to the peak temperature reached during scanning at each hatch spacing. At 0.3 mm hatch spacing, scanlines overlap significantly (overlap of 0.2 mm) and leads to the highest peak temperature of any sample as measured by IR camera during scanning (139.7° C). This peak temperature decreases significantly when hatch spacings are larger than the beam diameter (> 500 µm). Peak temperature decreases with increased hatch spacing due to a greater distance between scanlines, which limited conduction between them.

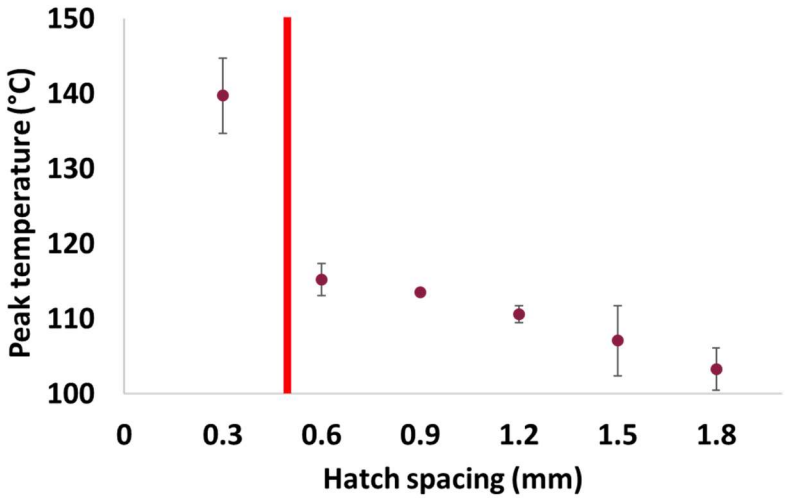

Figure 3.8 Peak temperature of scanned area as measured by in situ IR thermography decreases significantly as hatch spacing becomes greater than the beam diameter (0.5 mm) shown in red. Above that value, peak temperature slowly decreases as the distance between scanlines decreases the amount of conduction between scanlines.

At a 1.2 mm hatch spacing, single layer samples showed little to no z-direction expansion (Figure 3.7) and little conduction between scanlines (Figure 3.8). At this hatch spacing, approximately 42% of a layer's area will be scanned (beam diameter divided by hatch spacing), while the majority of the layer is loose, unscanned powder. This hatch spacing balances scanning a large fraction of each layer to provide green part strength, while still greatly limiting conduction between scanlines and preventing z-direction growth. Based on the experiments shown in this section, the processing parameters of 50 W for power, 1000 mm/s for beam velocity and a 1.2 mm hatch spacing were chosen for the infill and contour laser parameters.

3.6.3: Characterization of printed parts

3.6.3.1 Analysis of green parts

Printing multilayer parts with these processing parameters in section 3.2 was successful. Printed green parts were brittle but could be removed from the powder bed by placing a perforated metal sheet on the build piston before printing. This allowed the samples to be removed from the printer and then excess powder surrounding the part was removed using compressed air. Complex parts with a variety of different layer shapes were printed.

Green parts had a printed density of 0.424 ± 0.023 g/cm^3. It is noted that this value is lower than the static density for this powder (0.477 ± 0.003 g/cm^3), due to the effects of recoating. Green parts dimensions showed a $-1.3 \pm 2.6\%$ deviation from its set dimension in the x-axis, $-1.9 \pm 2.0\%$ in the y-axis and $-5.6 \pm 4.1\%$ in the z-axis. This high level of accuracy in the x and y-axes suggests conduction from the scanned part to the surrounding powder is insufficient to raise the surrounding powders' temperature enough to cause melting. Loss of height in the z-axis is likely due to loss of loose powder during part removal. However, the amount of dimension loss in this direction is still

quite low and could be calibrated to account for differences in dimensions, as is standard for PBF of commercial materials.

DSC of the printed scaffold that was scanned during printing was performed. To test only the areas scanned during printing, compressed air was used to remove all loose powder inside the high hatch spacing printed parts. Figure 3.6 showed that the neat, unprocessed powder has only one melting peak when measured with DSC. The scanned powder area of the part shows two melting peaks. The higher temperature peak at 138° C occurs at the same temperature as melting peak observed in the neat powder. The second peak occurred at a lower temperature, which suggests only a fraction of the measured sample has melted and recrystallized at a lower temperature. This result suggests that powder particles are only partially melted during scanning, possibly only melting the particles at the center of the laser scanline or only melting the surface of the particles. This partial melting behavior has been previously observed when processing Nylon 12 with insufficient energy density to fully melt the powder particles [41].

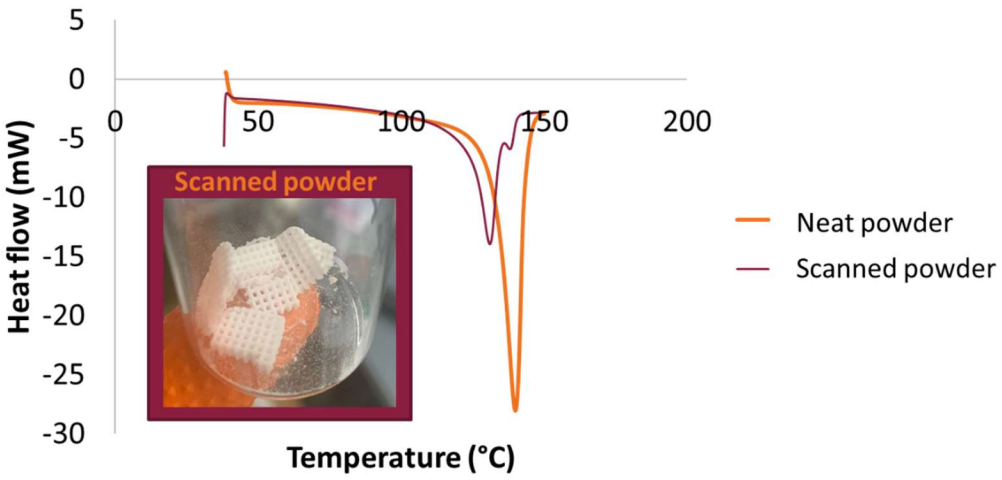

Figure 3.9 DSC of both the scanned section from a printed part with excess, unmelted powder removed and the neat, as received powder. The scanned powder curve has two peaks which suggests a partial melting of the powder.

3.6.3.2: Post-processed part analysis

For a sample that fractured along a layer interface during printing, both the high hatch spacing infill and the contour are visible inside the sample after post-processing (Figure 3.10).

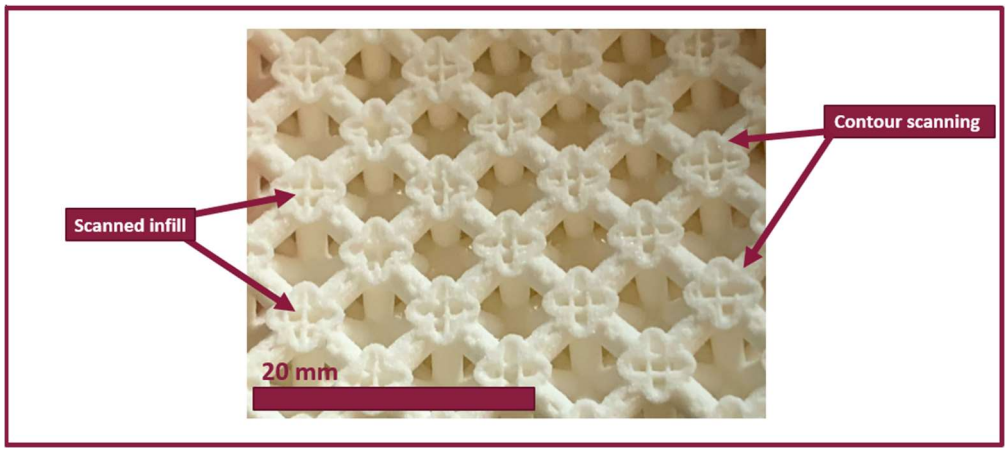

Figure 3.10 In this lattice sample, vertical and horizontal lines are visible in the sample and show the hatch spacing scanned infill. The contour scanline that traces the perimeter of the scanned layer is visible as well.

Table 3.2 All mechanical and dimensional properties measured for samples at each post-processing temperature.

Post-processing temperature (°C)	Tensile strength (MPa)	Elongation at break (%)	Density (g/cm³)	X-direction shrinkage (%)	Y-direction shrinkage (%)	Z-direction shrinkage (%)	Volumetric shrinkage (%)	Degree of crystallinity (%)
180	2.34 ± 0.20	52.61 ± 2.38	0.537 ± 0.018	6.06 ± 0.16	9.45 ± 1.54	10.09 ± 1.24	23.50 ± 5.77	44.8
200	1.82 ± 0.17	47.80 ± 5.75	0.544 ± 0.003	7.40 ± 0.49	6.58 ± 2.27	8.96 ± 0.69	21.20 ± 4.96	45.6
220	1.37 ± 0.06	50.39 ± 4.37	0.508 ± 0.002	3.84 ± 6.28	5.37 ± 3.60	6.41 ± 4.77	14.86 ± 3.81	46.5

Results of properties at east post-processing temperature are shown in Table 3.2. A two tailed T-test was used to assess if differences in measured properties between each post-processing temperature were significantly different and a p-value of 0.05 was chosen for these tests. Surprisingly, tensile specimens showed decreasing tensile strength with increasing temperature, which suggests that coalescence in these parts is not controlled by reptation, which scales with temperature, and is more likely primarily controlled by melt explosion of un-melted regions of powder in the part. All post-processing temperatures showed statistically significant differences in

tensile strength. Elongation at break at each post-processing temperature was near 50%, with no significant difference between any post-processing temperature. The peak tensile strength achieved was 2.34 ± 0.20 MPa when post-processing at 180 °C. This tensile strength is similar to the best reported tensile strength reported by Khalil et al., however this work demonstrates printing of complex geometries not reported by Khalil or Goodridge work [5,7].

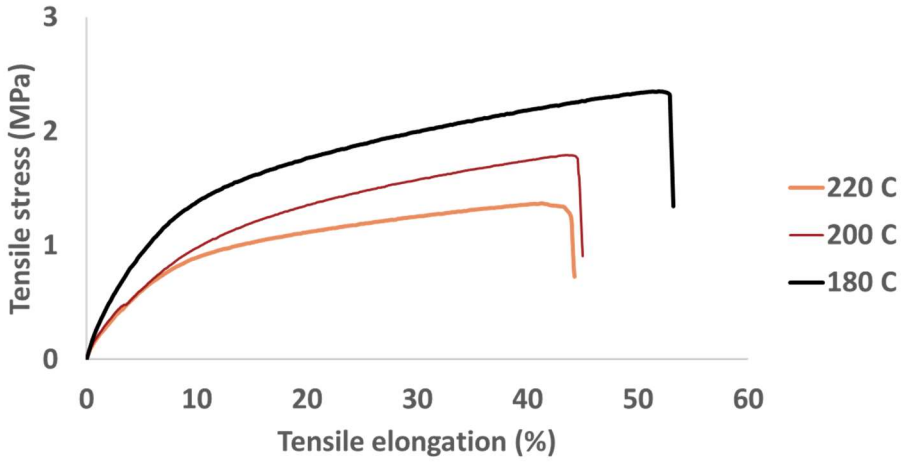

Figure 3.11 representative tensile curves for each post-processing temperature show a slight increase in tensile strength and elongation with decreasing post-processing temperature.

Sample densities were close to one another, and the only statistically significant difference in density occurred between the samples post-processed at 200 and 200° C. Densities for all post-processed samples are below the tapped density for the powder (0.569 ± 0.002 g/cm^3). No statistical difference was found for volumetric shrinkage at any post-processing temperature. Differences in shrinkage between the X, Y and Z direction of post-processed parts were not statistically significant at any temperature except the X and Y direction shrinkage in the 180° C samples.

All three post-processing temperatures led to samples with very similar degrees of crystallinity. No yellowing, or other discoloration was observed in any of the parts during printing or post-processing, which suggests that molecular weight loss is not present. Samples maintained their printed geometry and did not show any slumping of features, even when lattice geometries with significant overhangs were printed (Figure 3.12).

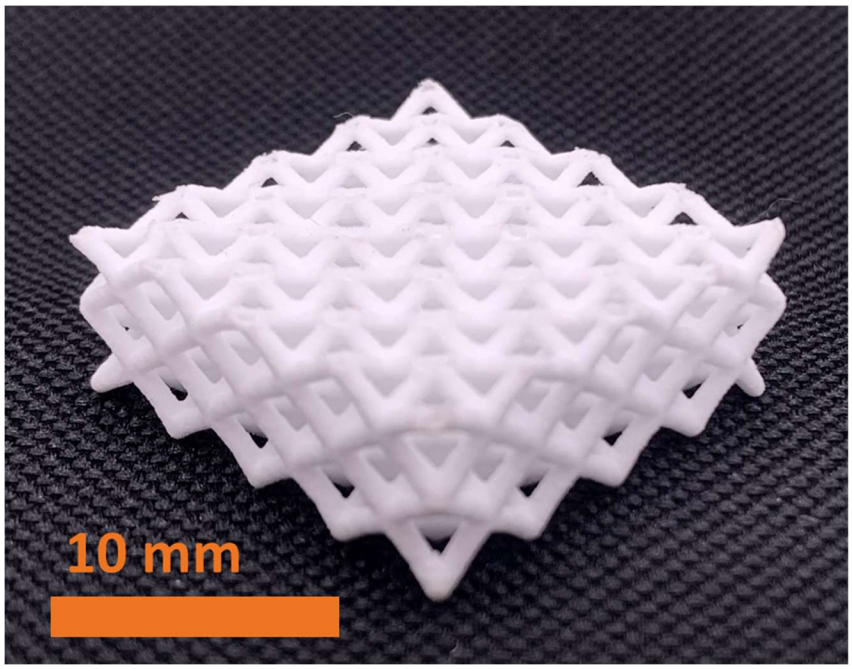

Figure 3.12, a printed lattice after being post-processed for 2 h at 220 °C under N_2. The high melt viscosity of the sample enables the part to maintain its shape during post-processing.

SEM of a tensile fracture surface shows that particles deformed very little during printing and post-processing (Figure 3.13). There is significant porosity in the part, which matches the low measured density compared to the bulk density of this polymer (0.925 g/cm^3). A closer inspection of the fracture surface shows that the samples are fracturing in areas of low contact between the particles. The morphology shows UHMWPE bridges connecting the particles; however, the bulk of each particle's volume retained its original, somewhat spherical, shape. The results suggest that

the measured stress is acting over a very small surface relative to the cross-sectional area used to calculate stress at break.

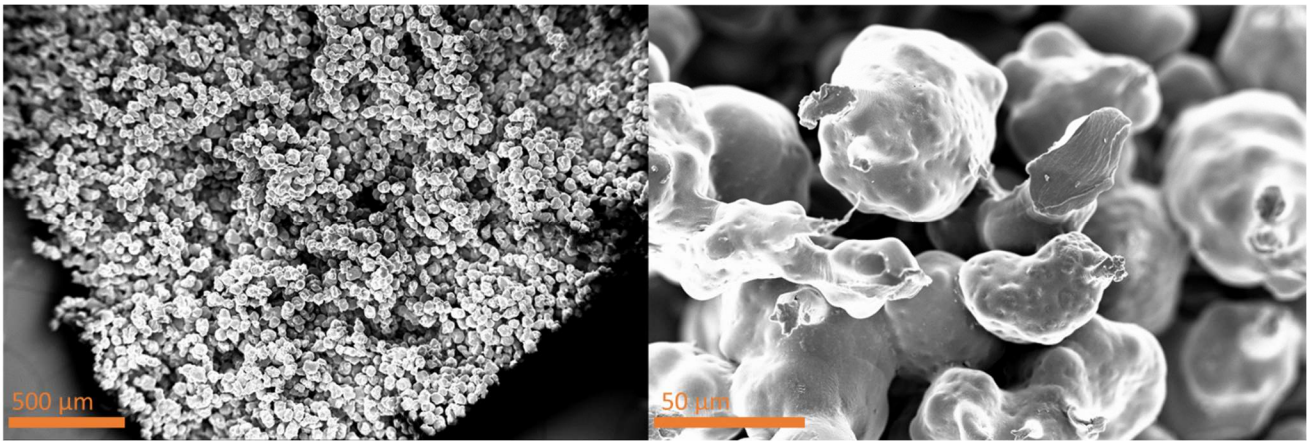

Figure 3.13 shows the fracture surface from a tensile specimen post-processed at 220 °C. Rather than deforming significantly during post-processing, samples have small deformations connect particles together and form a slightly interconnected network.

3.7: Conclusion & Future Work

Multilayer UHMWPE parts were successfully printed using a novel scan approach. By using a high hatch spacing, melting during scanning was controlled and expansion of the powder due to melt explosion was reduced to a level that enabled powder recoating. Printed samples were post-processed in the melt and maintained their shape during densification.

The DSC of scanned powder suggest that the partial melting of the scanned area allows the polymer particles to melt enough to coalesce and form a scaffold structure that can be removed from the print bed, while also limiting the z-direction growth that occurs during melting. This balance is crucial to enabling printing of this polymer.

When post-processing at 180° C, samples showed a 23.6% increase in density after thermal post-processing when compared to the printed green part density. Both density measurements and SEM images of the tensile fracture surface show significant porosity is present in samples even after post-processing, which leads to mechanical properties much lower than that of compression molded UHMWPE of the same molecular weight.

This work showed the first successful multilayer printing of UHMWPE with complex geometries. Additive manufacturing of this polymer was achieved by connecting process observations to melt explosion in UHMWPE. By understanding melt explosion, a solution using a scan strategy with especially high hatch spacing was determined. This research is the first example of setting a part's shape during the polymer PBF printing process and developing its mechanical properties during a post-processing step. UHMWPE's high melt viscosity was leveraged to enable thermal post-processing at temperatures well above its melting endotherm while maintaining the part's shape. In this research, densification of printed green parts was driven exclusively by heating. Traditional processing of UHMWPE uses both heating and pressure to drive densification. Future post-processing experiments will include both heating and pressure via a hot isostatic press (HIP), autoclave or other method. It is hypothesized that external pressure will help close pores in the parts and increase density, which will lead to more robust parts.

3.8: References

[1] G. Lewis, Polyethylene wear in total hip and knee arthroplasties, J. Biomed. Mater. Res. 38 (1997) 55–75.

[2] A. Das, J.S. Bryant, C.B. Williams, M.J. Bortner, Melt-Based Additive Manufacturing of Polyolefins Using Material Extrusion and Powder Bed Fusion, Polym. Rev. (2023) 1–66. https://doi.org/10.1080/15583724.2023.2220024.

[3] J. Higgins, D. Schroeder, Using Isostatic Pressing Techniques to Mold Uhmwpe, MRS Online Proc. Libr. OPL. 394 (1995).

[4] J.T. Rimell, P.M. Marquis, Selective laser sintering of ultra high molecular weight polyethylene for clinical applications, J. Biomed. Mater. Res. 53 (2000) 414–420. https://doi.org/10.1002/1097-4636(2000)53:4<414::AID-JBM16>3.0.CO;2-M.

[5] R.D. Goodridge, R.J.M. Hague, C.J. Tuck, An empirical study into laser sintering of ultra-high molecular weight polyethylene (UHMWPE), J. Mater. Process. Technol. 210 (2010) 72–80. https://doi.org/10.1016/j.jmatprotec.2009.08.016.

[6] Y. Khalil, A. Kowalski, N. Hopkinson, Influence of energy density on flexural properties of laser-sintered UHMWPE, Addit. Manuf. 10 (2016) 67–75. https://doi.org/10.1016/j.addma.2016.03.002.

[7] Y. Khalil, A. Kowalski, N. Hopkinson, Influence of laser power on tensile properties and material characteristics of laser-sintered UHMWPE, Manuf. Rev. 3 (2016) 15. https://doi.org/10.1051/mfreview/2016015.

[8] K.M. Kozlovsky, Additive Manufacturing of Ultra-High Molecular Weight Polyethylene under Applied External Pressure, Ph.D., University of Notre Dame, n.d. https://www.proquest.com/docview/2322186293/abstract/252693F78D224297PQ/1 (accessed April 26, 2022).

[9] R. Araujo Borges, D. Choudhury, M. Zou, 3D printed PCU/UHMWPE polymeric blend for artificial knee meniscus, Tribol. Int. 122 (2018) 1–7. https://doi.org/10.1016/j.triboint.2018.01.065.

[10] S.V. Panin, D.G. Buslovich, L.A. Kornienko, V.O. Aleksenko, Yu.V. Dontsov, B.B. Ovechkin, S.V. Shil'ko, Comparative Analysis of Tribological and Mechanical Properties of Extrudable Polymer–Polymer UHMWPE Composites Fabricated by 3D Printing and Hot-Pressing Methods, J. Frict. Wear. 41 (2020) 228–235. https://doi.org/10.3103/S1068366620030125.

[11] C.G. Schirmeister, T. Hees, O. Dolynchuk, E.H. Licht, T. Thurn-Albrecht, R. Muelhaupt, Digitally Tuned Multidirectional All-Polyethylene Composites via Controlled 1D Nanostructure Formation during Extrusion-Based 3D Printing, ACS Appl. Polym. Mater. 3 (2021) 1675–1686. https://doi.org/10.1021/acsapm.1c00174.

[12] M.S. Ramli, M.S. Wahab, M. Ahmad, A.S. Bala, FDM PREPARATION OF BIO-COMPATIBLE UHMWPE POLYMER FOR ARTIFICIAL IMPLANT, 11 (2016) 7.

[13] S.V. Panin, D.G. Buslovich, L.A. Kornienko, V.O. Alexenko, Yu.V. Dontsov, S.V. Shil'ko, Structure, as well as the Tribological and Mechanical Properties, of Extrudable Polymer-Polymeric UHMWPE Composites for 3D Printing, J. Frict. Wear. 40 (2019) 107–115. https://doi.org/10.3103/S1068366619020090.

[14] Y.V. Dontsov, S.V. Panin, D.G. Buslovich, F. Berto, Taguchi Optimization of Parameters for Feedstock Fabrication and FDM Manufacturing of Wear-Resistant UHMWPE-Based Composites, Materials. 13 (2020) 2718. https://doi.org/10.3390/ma13122718.

[15] C.A. Chatham, T.E. Long, C.B. Williams, A review of the process physics and material screening methods for polymer powder bed fusion additive manufacturing, Prog. Polym. Sci. 93 (2019) 68–95. https://doi.org/10.1016/j.progpolymsci.2019.03.003.

[16] B. Haworth, N. Hopkinson, D. Hitt, X. Zhong, Shear viscosity measurements on Polyamide-12 polymers for laser sintering, Rapid Prototyp. J. 19 (2013) 28–36. https://doi.org/10.1108/13552541311292709.

[17] J. Benz, C. Bonten, Temperature induced ageing of PA12 powder during selective laser sintering process, in: Dresden, Germany, 2019: p. 140001. https://doi.org/10.1063/1.5084904.

[18] J.F. Vega, S. Rastogi, G.W.M. Peters, H.E.H. Meijer, Rheology and reptation of linear polymers. Ultrahigh molecular weight chain dynamics in the melt, J. Rheol. 48 (2004) 663–678. https://doi.org/10.1122/1.1718367.

[19] T.G. Fox, P.J. Flory, Further Studies on the Melt Viscosity of Polyisobutylene., J. Phys. Chem. 55 (1951) 221–234. https://doi.org/10.1021/j150485a010.

[20] W.L. Peticolas, J.M. Watkins, The Molecular Structure of Polyethylene. VII. Melt Viscosity and the Effect of Molecular Weight and Branching [1], J. Am. Chem. Soc. 79 (1957) 5083–5085. https://doi.org/10.1021/ja01576a002.

[21] S. Wu, Interfacial and Surface Tensions of Polymers, J. Macromol. Sci. Part C Polym. Rev. 10 (1974) 1–73. https://doi.org/10.1080/15321797408080004.

[22] C.A. Chatham, M.J. Bortner, B.N. Johnson, T.E. Long, C.B. Williams, Predicting mechanical property plateau in laser polymer powder bed fusion additive manufacturing via the critical coalescence ratio, Mater. Des. 201 (2021) 109474. https://doi.org/10.1016/j.matdes.2021.109474.

[23] D.M. Sadler, A. Keller, Neutron Scattering of Solution-Grown Polymer Crystals: Molecular Dimensions Are Insensitive to Molecular Weight, Science. 203 (1979) 263–265. https://doi.org/10.1126/science.203.4377.263.

[24] C. Bastiaansen, H. Meyer, P. Lemstra, Memory effects in polyethylenes: influence of processing and crystallization history, Polymer. 31 (1990) 1435–1440. https://doi.org/10.1016/0032-3861(90)90147-Q.

[25] -Gilles de Gennes, “Explosion”upon melting, Comptes Rendus Académie Sci. Sér. 2 Mécanique Phys. Chim. Astron. (1995) 363–365.

[26] T. Deplancke, O. Lame, F. Rousset, I. Aguili, R. Seguela, G. Vigier, Diffusion versus Cocrystallization of Very Long Polymer Chains at Interfaces: Experimental Study of Sintering of UHMWPE Nascent Powder, Macromolecules. 47 (2014) 197–207. https://doi.org/10.1021/ma402012f.

[27] T. Deplancke, O. Lame, F. Rousset, R. Seguela, G. Vigier, Mechanisms of Chain Reentanglement during the Sintering of UHMWPE Nascent Powder: Effect of Molecular Weight, Macromolecules. 48 (2015) 5328–5338. https://doi.org/10.1021/acs.macromol.5b00618.

[28] J. Herzberger, V. Meenakshisundaram, C.B. Williams, T.E. Long, 3D Printing All-Aromatic Polyimides Using Stereolithographic 3D Printing of Polyamic Acid Salts, ACS Macro Lett. 7 (2018) 493–497. https://doi.org/10.1021/acsmacrolett.8b00126.

[29] P.J. Scott, V. Meenakshisundaram, M. Hegde, C.R. Kasprzak, C.R. Winkler, K.D. Feller, C.B. Williams, T.E. Long, 3D Printing Latex: A Route to Complex Geometries of High Molecular Weight Polymers, ACS Appl. Mater. Interfaces. 12 (2020) 10918–10928. https://doi.org/10.1021/acsami.9b19986.

[30] D.A. Rau, J. Herzberger, T.E. Long, C.B. Williams, Ultraviolet-Assisted Direct Ink Write to Additively Manufacture All-Aromatic Polyimides, ACS Appl. Mater. Interfaces. 10 (2018) 34828–34833. https://doi.org/10.1021/acsami.8b14584.

[31] P.J. Scott, D.A. Rau, J. Wen, M. Nguyen, C.R. Kasprzak, C.B. Williams, T.E. Long, Polymer-inorganic hybrid colloids for ultraviolet-assisted direct ink write of polymer nanocomposites, Addit. Manuf. 35 (2020) 101393. https://doi.org/10.1016/j.addma.2020.101393.

[32] Y. Bai, C.B. Williams, An exploration of binder jetting of copper, Rapid Prototyp. J. 21 (2015) 177–185. https://doi.org/10.1108/RPJ-12-2014-0180.

[33] F.M. Mirabella, A. Bafna, Determination of the crystallinity of polyethylene/α-olefin copolymers by thermal analysis: Relationship of the heat of fusion of 100% polyethylene crystal and the density, J. Polym. Sci. Part B Polym. Phys. 40 (2002) 1637–1643. https://doi.org/10.1002/polb.10228.

[34] C.A. Chatham, T.E. Long, C.B. Williams, Powder bed fusion of poly(phenylene sulfide) at bed temperatures significantly below melting, Addit. Manuf. 28 (2019) 506–516. https://doi.org/10.1016/j.addma.2019.05.025.

[35] M. Schmid, A. Amado, K. Wegener, Polymer powders for selective laser sintering (SLS), (n.d.) 6.

[36] B. Caulfield, P.E. McHugh, S. Lohfeld, Dependence of mechanical properties of polyamide components on build parameters in the SLS process, J. Mater. Process. Technol. 182 (2007) 477–488. https://doi.org/10.1016/j.jmatprotec.2006.09.007.

[37] L.J. Tan, W. Zhu, K. Sagar, K. Zhou, Comparative study on the selective laser sintering of polypropylene homopolymer and copolymer: processability, crystallization kinetics, crystal phases and mechanical properties, Addit. Manuf. 37 (2021) 101610. https://doi.org/10.1016/j.addma.2020.101610.

[38] P.K. Jain, P.M. Pandey, P.V.M. Rao, Experimental investigations for improving part strength in selective laser sintering, Virtual Phys. Prototyp. 3 (2008) 177–188. https://doi.org/10.1080/17452750802065893.

[39] S. Berretta, K.E. Evans, O. Ghita, Processability of PEEK, a new polymer for High Temperature Laser Sintering (HT-LS), Eur. Polym. J. 68 (2015) 243–266. https://doi.org/10.1016/j.eurpolymj.2015.04.003.

[40] Y. Shi, J. Chen, Y. Wang, Z. Li, S. Huang, Study of the selective laser sintering of polycarbonate and postprocess for parts reinforcement, Proc. Inst. Mech. Eng. Part J. Mater. Des. Appl. 221 (2007) 37–42. https://doi.org/10.1243/14644207JMDA65.

[41] H. Zarringhalam, N. Hopkinson, N.F. Kamperman, J.J. de Vlieger, Effects of processing on microstructure and properties of SLS Nylon 12, Mater. Sci. Eng. A. 435–436 (2006) 172–180. https://doi.org/10.1016/j.msea.2006.07.084.

Chapter 4: Pressurized post-processing of ultra-high molecular weight polyethylene processed via powder bed fusion

Coauthor: Yifeng Lin

4.1 Abstract:

Ultra-high molecular weight polyethylene (UHMWPE) offers the best wear properties found in thermoplastic materials. However, processing this material is intensely difficult due to its high melt viscosity. Recently, the authors presented a novel tool-pathing strategy in which the powder was lightly fused to set the shape, and a thermal post process further consolidated the powder. The high viscosity of UHMWPE prevented slumping and distortion of the part. While the approach presented a path towards creating 3D shapes from UHMWPE, parts were limited by very low densities and poor mech properties. In this work, the authors explore the impact of applying an isostatic pressure to the post-processing thermal treatment on the density, crystallinity, and mechanical properties of printed UHMWPE. It was discovered that the use of cold isostatic pressing to densify samples at room temperature and then using hot isostatic pressing to densify the sample in the melt successfully yielded fully dense printed parts. Parts processed in this manner achieved density and strain at break equivalent to compression molded properties for the same grade of UHMWPE, with only slightly lower tensile strength.

4.2. Introduction

4.2.1 Post-processing in additive manufacturing

Although often heralded for being a complete manufacturing system capable of directly producing final parts, almost all additive manufacturing (AM) processes require post-processing steps to

achieve final part properties. All metal AM processes require some post-process annealing, heat treatment, sintering, and/or hot isostatic pressing. For example, in binder-jetting (BJT), samples do not have significant strength in their as printed state and instead develop their properties during a post-process heating in which binder is burned out—referred to as debinding—and sintering, which enables densification of the printed material below its melting temperature [1].

Polymer AM processes also require post-processing to remove support structures, to remove excess powder, to complete curing, or to initiate additional chemical reactions. For example, in vat photopolymerization (VP), printed parts often undergo a post-cure to react any uncured material and strengthen the part [2,3]. In other approaches, resins are printed so that only phase of the material cures during UV processing while the rest of the material cures during a thermal post-process [4–6]=. Hegde et al., used VP to print fully-aromatic polyimides, by first photocuring a scaffold material and trapping a polyamic acid precursor in the scaffold to create an organogel. Through drying and a thermal post-processing step, imidization occurred to form a printed polyimide part [7,8]. Later studies explored even higher post-processing temperatures to form carbonaceous structures [9].

Within filament-based thermoplastic material extrusion (MEX), post-processing can include annealing to heal interfaces created during processing and increase mechanical properties [10]. Annealing of the amorphous polymers most often printed in MEX is limited to temperatures below the glass transition temperature (T_g) of the material (which severely limits the amount of diffusion that can occur to heal interfaces), as post-processing above T_g would cause parts to deform and lose dimensional accuracy [10]. Wach et al. explored thermal annealing in MEX-printed polylactic acid (PLA), and observed no densification, but observed increases in crystallinity that led to increases in mechanical properties [11]. This result is expected because polymer chains are

restricted from moving distances large enough to consolidate below T_g for amorphous polymers, and below the melting endotherm for semicrystalline polymers. Other researchers have circumvented this limitation by printing core-shell composite filaments via MEX. The shell polymer had a lower T_g than the core polymer, which allowed heating that would enable flow in the shell (above shell T_g) but no deformations in the core polymer [10].

In polymer powder bed fusion (PBF), Chatham et al. intentionally induced oxidation during thermal post-processing to crosslink polyphenylene sulfide as a method for tuning printed parts' storage modulus [12]. Post-processing has generally not been explored in PBF due to the limitations of the material to maintain shape when heated to elevated temperatures (above T_m). However, post-processing is necessary to develop mechanical properties in PBF printed ultra-high molecular weight polyethylene (UHMWPE).

4.2.2 Powder bed fusion of UHMWPE

Recently, the authors demonstrated the use of a thermal post process to enable PBF processing of complex UHWMPE parts from a 3000 kDal powder. Older studies in powder bed fusion of UHMWPE have yielded parts that that are weak compared to compression molded UHMWPE and have been unable to print complex geometries [13–17]. To enable printing of multilayer complex 3D parts, the authors selectively scanned the UHMWPE powder bed with large hatch spacing (1.2 mm) to partially melt the powder during the printing process; a thermal post-process in the melt further densified the 3D parts. However, this post-processing step yielded parts that were only 55% dense compared to the density of the bulk polymer, and did not yield part properties comparable to compression molding of the same material (tensile strength < 3 MPa) [18].

4.2.3 Consolidating UHMWPE

The overall goal of this work is to explore post-processing methods for PBF-produced UHMWPE to result in full density and have equivalent performance to compression molded UHMWPE. Consolidation in all traditional UHMWPE manufacturing processes relies on using high pressures to densify the part. For example, during the compaction step in compression molding, which occurs before melting of the material, UHMWPE powder is compacted to 80-90% relative density [19]. This high starting density minimizes the amount of densification needed during molding [20].

Ram extrusion, sheet molding and compression molding all provide pressure to a molten material over a long time to create a dense final part [21]. The pressure in these processes is required for consolidation because of UHWMPE's high melt viscosity, which in some recorded cases is as high at 10^8-10^{10} Pa-s [20,22]. This two orders of magnitude higher than the zero-shear viscosities (η_o) of PBF-grade polyamide 12, which is less than 10^3 Pa-s [23,24].

One primary conclusion in the authors' previous work on PBF of UHMWPE was that melt explosion is both the largest issue during processing and also the only way to achieve coalescence of UHMWPE on PBF timescales [18]. Research into melting of nascent or solution crystallized UHMWPE has found that this material has a much smaller radius of gyration (R_g) in its crystallized state and low levels of entanglements [25]. Beyond this unique small R_g, samples achieved their full, molten R_g faster than reptation theory would predict by way of a phenomenon de Gennes labeled as "explosion upon melting," [26–28]. Results from previous researchers suggest that expansion occurs during processing of UHMWPE in PBF [13,15,17]. Expansion during processing was thoroughly demonstrated and connected to melt explosion of the material in the authors' prior work [18].

The development of entanglements across particle interfaces is critical to the development of part properties during densification of UHMWPE. Erasing interfaces between particles is difficult to

achieve even during compression molding, and modeling of welding of UHMWPE interfaces to fully erase an interfaces predict times greater than one week to achieve this [29]. Researchers have demonstrated that developing entanglements across interfaces from UHMWPE samples that have already been melted is limited [30,31]. Xue et al. found that even at welding times exceeding 60 h, bulk properties were not achieved in their samples in their melt crystallized films [30]. Increases in pressure during molding of UHMWPE improves consolidation of the material [32].

4.2.4 Post-processing additively manufactured parts using pressure

Post-processing AM parts under pressure has also been explored but has been typically limited to metal AM parts. In hot isostatic pressing (HIP), parts are densified by a heated gas at pressures up to 200 MPa [3]. For BJT, significant increases in density and mechanical properties have been reported when parts are HIPed following sintering [33–35]. Similar results have been found for increasing fatigue strength and density in parts manufactured via metal PBF [36,37].

HIP of parts has been much less common in polymer AM; however, reductions in void content have been observed after HIP post-processing of carbon fiber reinforced polyetheretherketone (PEEK) composites printed via FFF [38]. Though the exploration of HIP in polymer PBF has been more limited, Abbott et al. demonstrated significant increases in mechanical properties for their post-processed polyamide 12 parts. Parts were held in a mold of salt around the part and the part was completed melted during post-processing [39].

4.2.5 Overview

To accomplish the overall goal of further enhancing the density and performance of PBF-printed UHMWPE, multiple post-processing methods that combine different steps of applying heat, pressure, or a combination of both, were explored. At each processing step or treatment, structural

and mechanical properties are characterized to understand the impact of each step. It is hypothesized that a combination of post-processing steps (cold isostatic pressing (CIP) and hot isostatic pressing (HIP)) could yield a fully dense part with compression molded performance. It was hypothesized that complete densification of the part (reaching bulk density) could not be achieved unless the sample was densified using pressure in the melt (via HIP) because in this phase, polymer chains would undergo enough motion to fully consolidate under pressure. The printing and post-processing steps are organized in Figure 4.14.

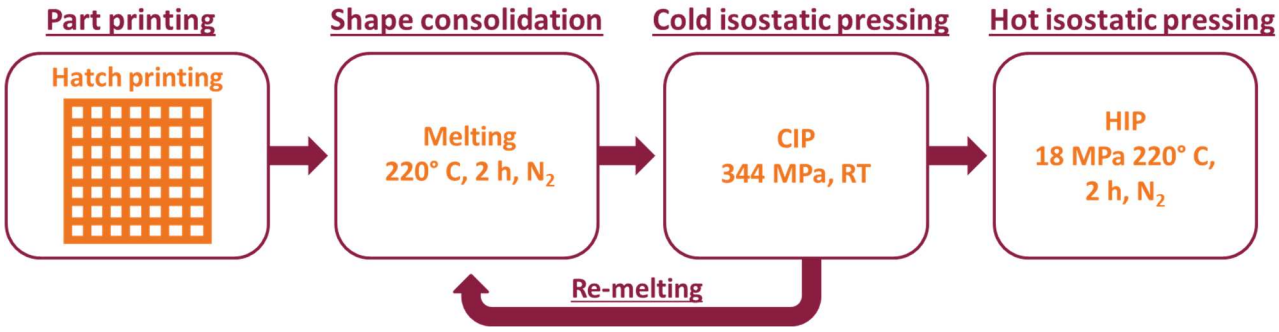

Figure 4.14 The sequence of post-processing steps explored to densify UHWMPE parts printed by PBF.

4.3. Materials and methods

4.3.1 Overview

Research on the effects of post-processing printed UHMWPE parts under pressure and/or heat was conducted by applying a series of treatments and characterizing the resultant parts' structure and mechanical properties. The different post-processing treatment explored are presented in Table 4.1, and are described in Section 2.5.2. Three tensile bar specimens were processed for each treatment and measured for all characterization of the treatments. Evaluation of the structure and properties of the parts resulting from each treatment will enable understanding of the process-structure-property relationships for post-processing treatments.

Table 4.13 Details of all post-processing treatments, which can involve Melting, Cold Isostatic Pressing (CIP), and Hot Isostatic Pressing (HIP). Temperature, time, environment, and pressure of post-processing treatment are detailed.

Treatment name	Post-processing step 1	Post-processing step 2	Post-processing step 3
Control	220° C, 2 h, N_2	-	-
CIP	220° C, 2 h, N_2	RT, 344 MPa, water	-
CIP + re-melt	220° C, 2 h, N_2	RT, 344 MPa, water	220° C, 2 h, N_2
CIP + HIP	220° C, 2 h, N_2	RT, 344 MPa, water	220° C, 2 h, N_2, 18 MPa
Melt-pressed	220° C, 15 min, 15 MPa	-	-

4.3.2 UHMWPE powder

A 3000 kDa UHMWPE powder was provided by Braskem North America. As reported in previous work , this powder has d10 = 42 µm, d90 = 103 µm and average particle size = 73 µm [18]. This powder showed an onset of melting at 123.5° C and peak melting temperature of 139° C in Chapter 3.

4.3.3 Melt-pressed sample

Powder was melt-pressed in a 3 mm thick tensile bar mold at 220° C for 15 min at 15 MPa. This sample serves as a fully dense control specimen that is similar to a compression molded sample and allows for comparison against printed specimens.

4.3.4 Part printing for post-processing treatments

4.3.4.1 Printing parameters

"Green parts" are the as-printed parts that come out of the printer. These samples are partially coalesced and must be thermally post-processed to become handleable. Print parameters were determined in previous work[18]. One set of processing parameters was used for all printed parts. These were: 50 W laser power, 1000 mm/s beam velocity, and 1.2 mm hatch spacing. The large

hatch spacings enables slight coalescence of scanlines during printing without expansion that causes warpage. Samples were printed at a bed temperature of 90° C. The contour scanning parameters were also 50 W and 1000 mm/s.

4.3.4.2 Testing specimen design

As the printed green parts are lightly sintered, they are quite fragile. To minimize printed part breakage, a thicker, non-standard tensile bar was printed, featuring a 5.75 mm gauge width, 14 mm gauge length and 7 mm thickness. Empirical observations showed that samples with a higher proportion of contour scanning compared to infill scanning were less likely to break during post-processing. To maximize the amount of area scanned with contour scanning, a lattice tensile bar was designed. Using a lattice geometry helps to maximize surface area of the part which would be scanned using a contour. A lattice designed in nTopology. Then, a Boolean subtraction was performed to remove the lattice's volume from a solid tensile bar. The lattice chosen was a gyroid with 0.25 mm thickness, and unit cells 1.5 mm in length. The resulting negative lattice had a 60% volume fraction of the part. This created a lattice surface inside the part that would be primarily scanned with contour scans as opposed to conventional PBF printing of a solid tensile bar where contour scans only occur on the outside surface of the part. This design was able to be printed in the PBF system without failure, and also entrapped unscanned powder within the lattice voids for consolidation in subsequent post-processing steps. All specimens were printed in the XY orientation.

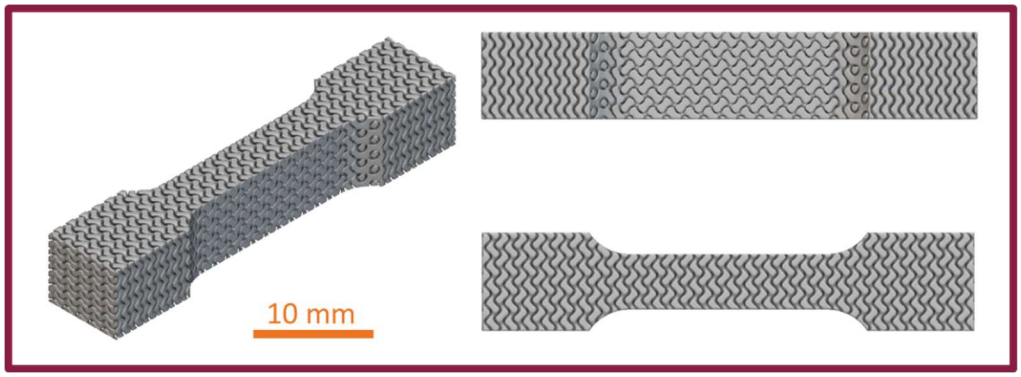

Figure 4.15 the negative lattice sample does not have a smooth surface, but led to less breakage of tensile specimens during depowdering compared to the high hatch spacing approach developed by Bryant et al.[18].

4.3.5 Post-processing

4.3.5.1 Thermal post-processing

After printing, the samples were retrieved from the powder bed and then placed in an oven, where they were held at 220° C for 2 h under N_2 to melt the material and densify the part. As noted in prior work, despite being held above its melt temperature, the specimens held their printed shape due to UHWMPE's high MW[18]. This first thermal post-processing step was conducted for all tested samples and acts as a control specimen when evaluating post-processing treatments. Shrinkage during this initial post-processing step is isotropic [18].

4.3.5.2 Cold isostatic pressing (CIP)

Following the initial thermal post-process treatment, samples were then processed via Cold Isostatic Pressing (CIP), to further consolidate the green body, reduce interparticle spacing and increase contact surface area. To prepare samples for CIP, samples were first encased in fine, powdered salt and wrapped in two layers of aluminum foil. The fine salt powder provides a supporting structure to minimize distortion during CIP. Salt is chosen as it is readily dissolved following processing (as has been demonstrated by other AM researchers exploring MEX

annealing [39,40]) and will not undergo a phase change in subsequent thermal post-processing treatment. Fine powders were chosen so that the salt particles didn't impact into the part surface during post-processing and add additional texture to the part. The aluminum foil package holds the salt in place and can deform and compress the sample during CIP. The aluminum foil package was then placed inside a latex balloon and sealed. The balloon was then wrapped in a non-woven breather fabric; the resulting package was then placed inside a second balloon. The breather fabric protects the outer balloon from potential puncturing from the aluminum foil as it is compressed during CIP. The balloons provide a flexible membrane and seal between the sample and the water used to apply pressure during the CIP process.

Samples were CIPed at 344 MPa (50 kpsi). This pressure was chosen because it was the maximum pressure possible for this CIP and densification would be maximized by using the highest pressure.

4.3.5.3 CIP + thermal post-processing

While CIP can compress samples to increase contact surface area between UHWMPE particles, it cannot heal the interfaces in the sample since CIP occurs below the melting endotherm of the sample. As such, 3 CIPed samples were then held at 220° C for 2 h under N_2 to re-melt the material and enable healing of the interfaces within the sample. This treatment affords the opportunity to disprove the hypothesis that applying pressure to the specimen while it is in the melt state is vital for achieving full densification.

4.3.5.4 CIP + hot isostatic pressing (HIP)

The remaining CIPed samples were subsequently processed via hot isostatic press (HIP) to explore the impact of added pressure while being held in the melt. It was hypothesized that application of pressure while parts were in the melt would lead to further densification of the part. Before being

processed in the HIP, the CIP samples were removed from the balloons and breather fabric. The resulting sample, now encased in salt and wrapped in aluminum foil, was encased in a silicone (Moldex Mold Max^{TM} 60) to create an air-tight barrier around the sample. Silicone was chosen to provide a flexible, air-tight membrane to compress the sample further and also would not degrade under further thermal post-processing.

Samples were then placed in the HIP (MTI High Pressure Vessel (HPV-LH) with a 3 L volume), and were held at 220° C under N_2, which was used to pressurize the vessel, for 2 h. The vessel took 8 h to heat up to this temperature and 8 h to cool down to room temperature after testing. This test took a total of 18 h to complete and heating and cooling rates were roughly 1.5° C/min. The pressure in the chamber during the temperature hold was 18 MPa, and this pressure was maintained during the cooling process to ensure no foaming occurred as pressure was released. This pressure was the maximum achievable pressure for this system and was chosen to maximize densification.

4.3.6 Part characterization

The crystallinity, porosity, and mechanical properties of the parts resulting from each post-processing treatment were characterized to establish corresponding process-structure-property relationships.

4.3.6.1 Differential scanning calorimetry (DSC)

After each post-processing treatment, samples were characterized using DSC. This test was used to evaluate the crystallinity in the sample and understand how crystallinity contributed to the mechanical performance of the treated parts. Samples were heated from 40° C to 180° C at 10 °C/min and then cooled to 40° C at 10 °C/min. The DSC used was a TA Q2000.

4.3.6.2 Density and shrinkage

The density of each treatment was measured to understand the amount of porosity within the part. As mechanical properties increase with density, this measurement allows the structure to be connected to the final part properties. For samples dense enough to sink in ethanol, the Archimedes method was used. In this method, the mass of the sample in ethanol is measured and used to calculate the sample's volume and then calculate density. For samples that were not dense enough to sink in ethanol (e.g., Control, CIP, CIP + re-melt), mass and dimensional measurements were made from sections cut from processed samples to calculate density.

Tensile specimens were measured for shrinkage after each post-processing treatment and compared to the Control specimens. Dimensions were measured using digital calipers. The X dimension was the length of the tensile bar, Y was the gauge width and Z was the gauge thickness (i.e., the same coordinate system as the print orientation). These measurements were taken to understand if shrinkage due to densification was isotropic.

4.3.6.3 Scanning electron microscopy (SEM)

Scanning electron microscopy (JEOL IT-500HR) was used to image a freeze fractured surface of specimens to better understand the porosity within the part at each step of post-processing. Samples were sputter coated with a 5 nm thick Iridium (Ir) coating and measured at 10 kV and measured at 200x magnification.

4.3.6.4 Hardness testing

Hardness was measured on printed and post-processed specimens using a Shore D hardness tester. Three measurements were taken for each treatment. For comparison, Braskem reports a Shore D hardness of 58 for the grade of UHMWPE used in this research processed using compression molding.

4.3.6.5 Tensile testing

To evaluate the mechanical properties of the parts at each treatment, tensile specimens were tested to failure at a strain rate of 5 mm/min on a universal testing machine (Instron 5944) using a 2 kN load cell.

4.4 Results

4.4.1 Differential scanning calorimetry (DSC)

Results from DSC of specimens following each post-processing treatment are presented in Figure 4.16 4.3. It is observed that samples that were processed without pressure while being in the melt state (e.g., Control, CIP, and CIP + re-melt) showed minimal. While all specimen's DSC curves show the same general shape, samples that were under pressure while in the melt state (e.g., CIP + HIP and Melt-pressed treatments) display an increase in the temperatures of the melting endotherm, which is indicative of thicker crystals in the sample (Figure 4.16).

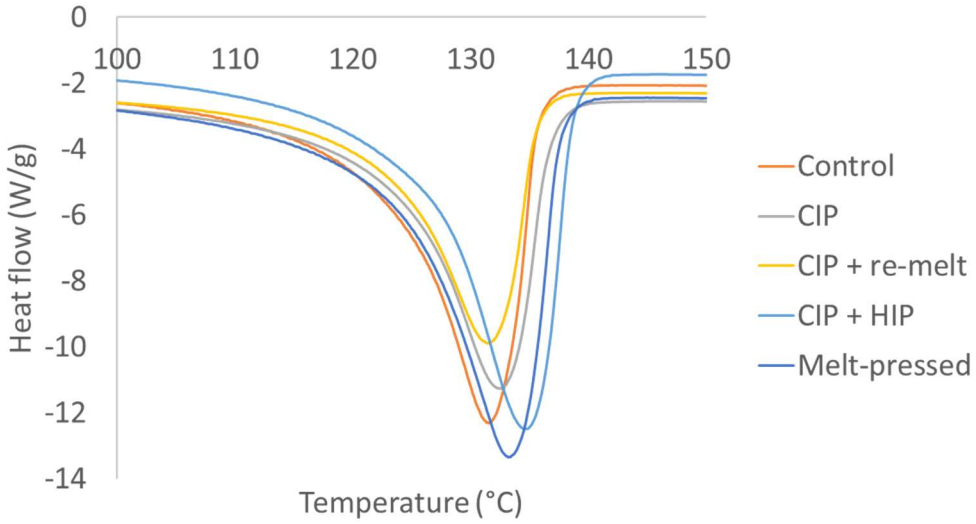

Figure 4.16 DSC curves show only small changes between samples, with slight shifts to higher temperatures for the CIP + HIP and Melt-pressed samples.

Though there are some shifts in the curves as shown in Figure 4.16, the CIP + HIP treatment was the only treatment that led to a statistical difference ($p < 0.05$) in degree of crystallinity (X%) (Figure 4.17). The CIP + HIP treatment samples had an increased crystallinity ranging from 6.9-9.3% compared to the other samples. This result suggests that the pressure, which is still applied during cooling and crystallization in CIP+HIP, increases the X% of the parts by forcing the polymer chains form crystals which are denser than the amorphous phase (Figure 4.17). For all other samples, there is no pressure applied during the cooling of the sample.

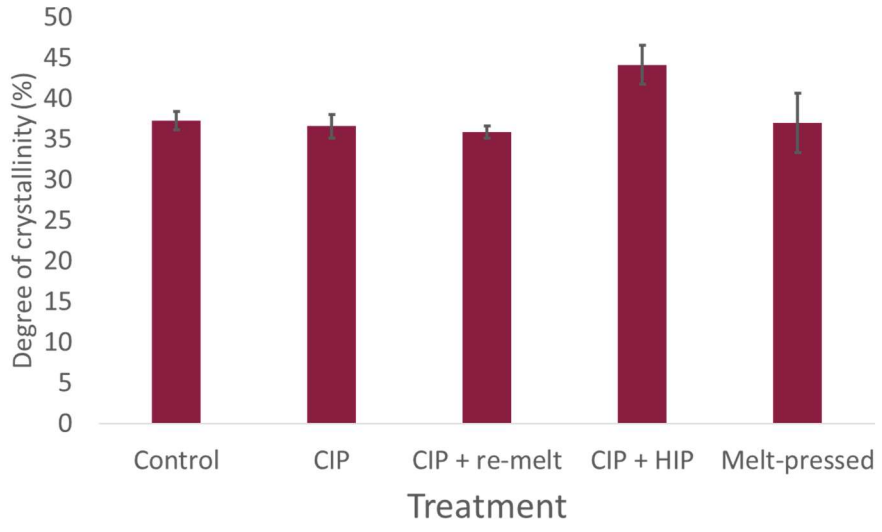

Figure 4.17 treatments show similar X% excluding the CIP + HIP treated samples. These samples show an increase in crystallinity that likely comes from the pressure applied on the samples during cooling and crystallization.

The peak melting temperature ($T_{m,peak}$) for each treatment showed a similar trend (Figure 4.18); while all other treatments were similar, the CIP + HIP sample showed a statistically significant difference in $T_{m,peak}$. Samples with higher X% are more likely to form thicker crystals, which would increase the temperatures of the melting endotherm.

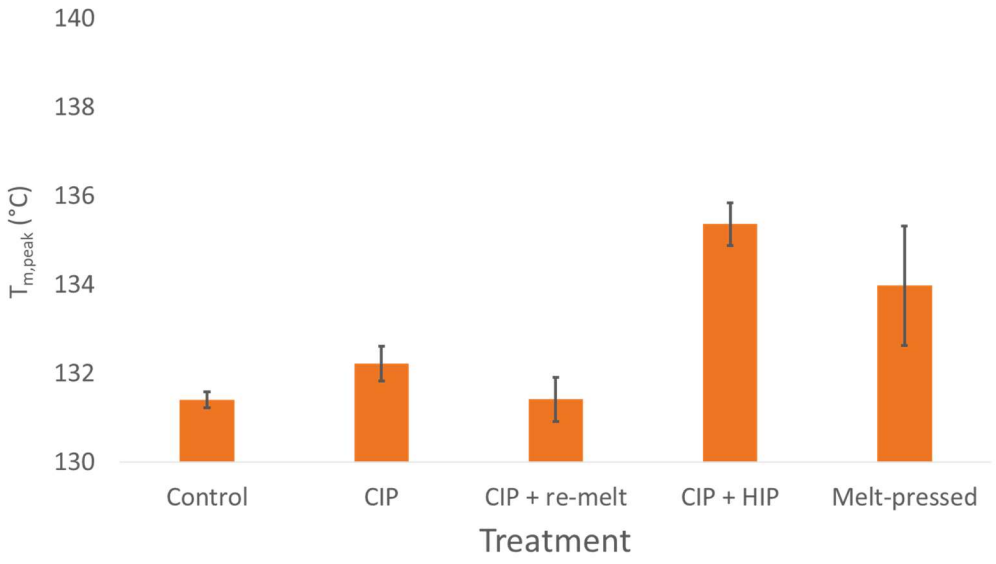

Figure 4.18 DSC measurements show that the overall shifts in peak melting temperatures were small between each treatment.

$T_{m,peak}$ and crystallinity measurements are collected in Table 4.2. The overall spread of the values is small, which is likely caused by UHMWPE's ability to crystallize and how processing will show only small impacts on that (excluding the sample crystallized under pressure for the CIP + HIP treatment).

Table 4.2 displays the key DSC results for each treatment

Treatment	X%	Peak T_m
Control	37.25 ± 1.14	131.40 ± 0.19
CIP	36.57 ± 1.46	132.22 ± 0.39
CIP + heat	35.82 ± 0.74	131.41 ± 0.50
CIP + HIP	44.11 ± 2.40	135.36 ± 0.48
Melt pressed	36.96 ± 3.65	133.97 ± 1.35

4.4.2 Density

Figure 4.19 presents the density measurements for specimens following each treatment condition. Overall, the results fall into three distinct levels of density. The lowest level only includes the control sample. This sample has not undergone any pressurized post-processing and therefore has a density far below the bulk density (0.925 g/cm^3). The two treatments that were only CIPed showed the next tier of samples, which achieved roughly 70% relative density. The over 300 MPa

of pressure applied during CIP can significantly deform and densify the sample, however this densification is still limited because pressure is applied while the UHMWPE is crystallized and a solid. Crystals restrict chain motion, which limits densification. The densification must occur via plastic deformation of the foam-like structure of the Control sample.

The CIP + HIP and Melt-pressed treatments resulted in the largest densification. Both treatments resulted in parts that achieved the bulk density of the polymer. This was enabled by pressure being applied while the sample was molten, which enables the polymer chains to deform and organize into a completely dense structure.

It is important to note that while CIP densifies the specimens by an additional ~50% increase (Figure 4.19), the CIP + re-melt specimens showed no significant increase in densification. This demonstrates that though there may be healing of the interface and entanglements across its surface, there is not any further densification occurring via surface tension during re-melting. This result is expected given the large MW of the UHMWPE. However, when pressure is applied to the specimen while being held above its Tm (as in CIP + HIP and Melt-pressed treatments), the specimens achieved full densification with values equaling the bulk density of the material (0.925 g/cm^3).

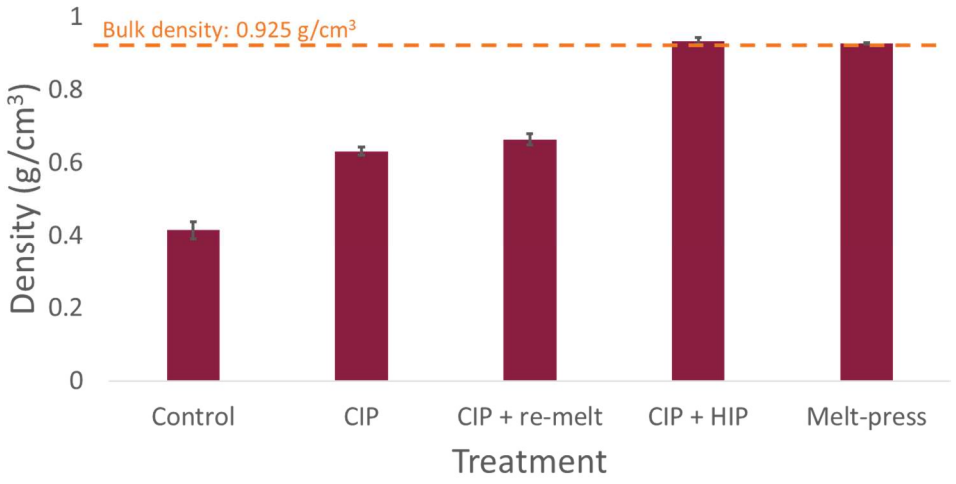

Figure 4.19 samples form three levels of density based on post-processing treatment. Both the CIP + HIP and Melt-pressed samples achieved complete densification since they have a measured density equal to the bulk density of the polymer.

4.4.3 Shrinkage

Table 4.3 dimensional and shrinkage measurements for each post-processing treatment.

Treatment	X (mm)	Y (mm)	Z (mm)	X (%)	Y (%)	Z (%)
Control	39.5 ± 0.04	4.6 ± 0.02	6.8 ± 0.06	-	-	-
CIP	34.6 ± 0.41	4.1 ± 0.02	6.2 ± 0.04	12.5	9.9	9.6
CIP + heat	33.2 ± 0.45	4.0 ± 0.11	6.0 ± 0.05	16.2	12.2	11.9
CIP + HIP	33.9 ± 0.15	3.6 ± 0.12	5.9 ± 0.13	14.3	22.0	14.0

Dimensional and shrinkage measurements are detailed in Table 4.3. Though for some dimensions, shrinkage appears to be isotropic in some directions, there is not a treatment which shows fully isotropic shrinkage. These results come from measurements of tensile bars with three unique designed sizes, which makes it difficult to determine shrinkage as precisely as if the tests were performed on cube samples. Shrinkage measurements are measured relative to the control treatment and not taken between treatment steps.

4.4.4 Scanning electron microscopy (SEM)

As shown in Figure 4.19, samples show very little densification during the first thermal processing step (Control treatment). Cross-sectional SEM microscopy of these samples elucidates that individual powder particles are largely intact after this stage of post-processing. The surface area connecting adjacent particles is very limited, which will reduce any mechanical performance of the resultant parts (Figure 4.7. T).

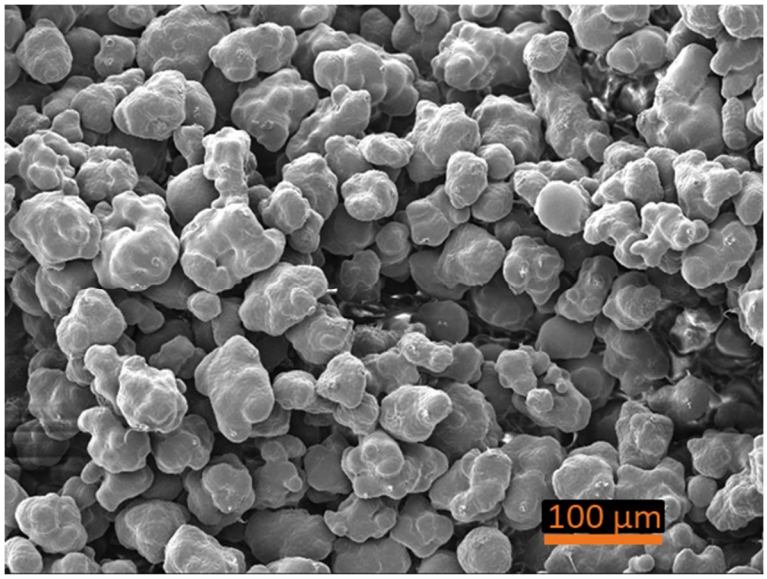

Figure 4.7. The initial melt processing of the printed parts shows little deformation of the particles, and minimal contact area between touching particles.

After CIP post-processing, particles are still visible within the part. This shows that interfaces between the particles are not being healed by pressure alone, which is expected since chain motion in the particles is restricted by crystallinity. Figure 4.20 does show that there is more contact area between particles, due to the higher density achieved after CIP. Creation of this contact surface could be helpful for enabling welding between particles during future molten post-processing of the samples.

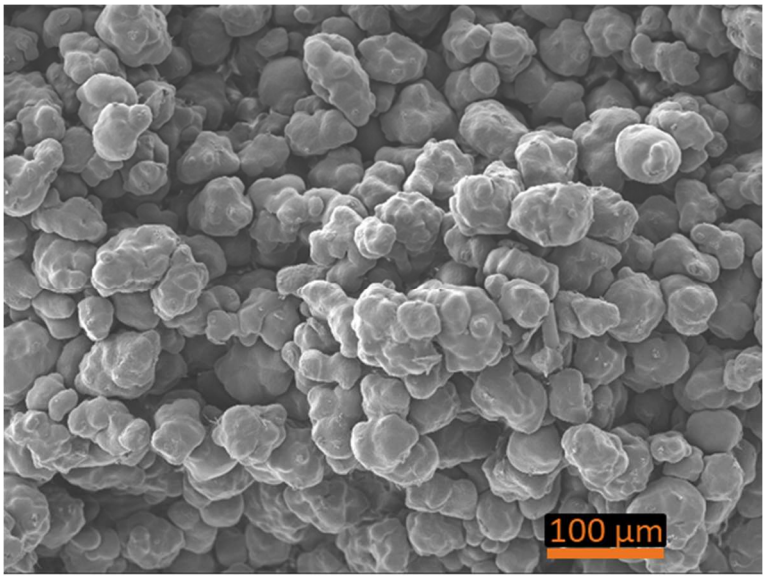

Figure 4.20. SEM image of CIP specimen cross-section. Particles have more contact area, but have not deformed.

After the second melt post-processing step for the CIP + re-melt samples, there is significant healing of the interfaces between particles. Particles can be seen to deform and coalesce somewhat, which forms large areas of continuous material (Figure 4.21). Remnants of particles are still visible in this sample.

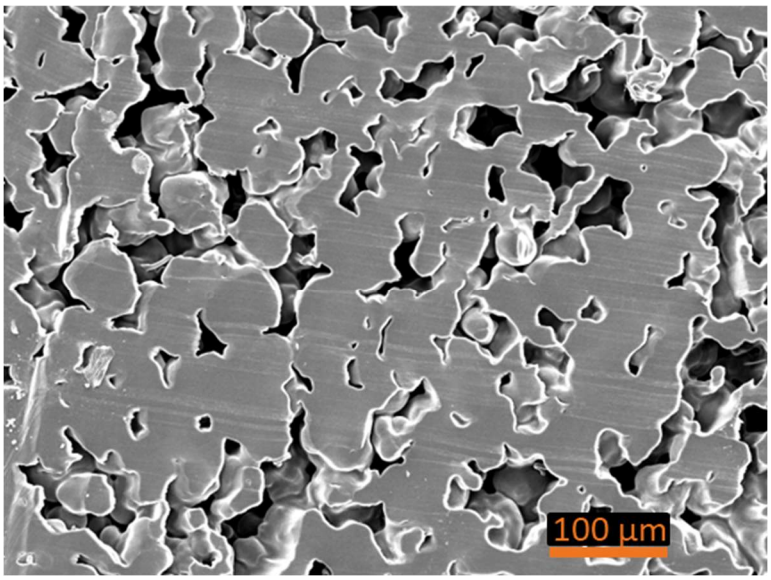

Figure 4.21 SEM of the re-melting the sample after CIP shows that there is significant healing of the surface following heat treatment.

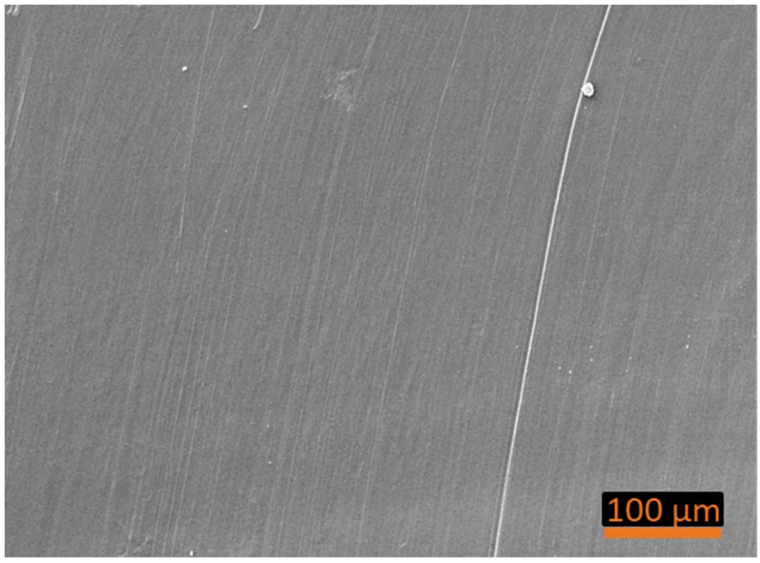

Figure 4.22 SEM of the CIP + HIP sample shows a very rough surface from the freeze fracture.

Figure 4.10 shows the cross-section of a CIP+HIP specimen, which elucidates the removal of individual particle interfaces. The surface shows no porosity, which suggests full densification of the part. This result agrees with the density results observed for this sample.

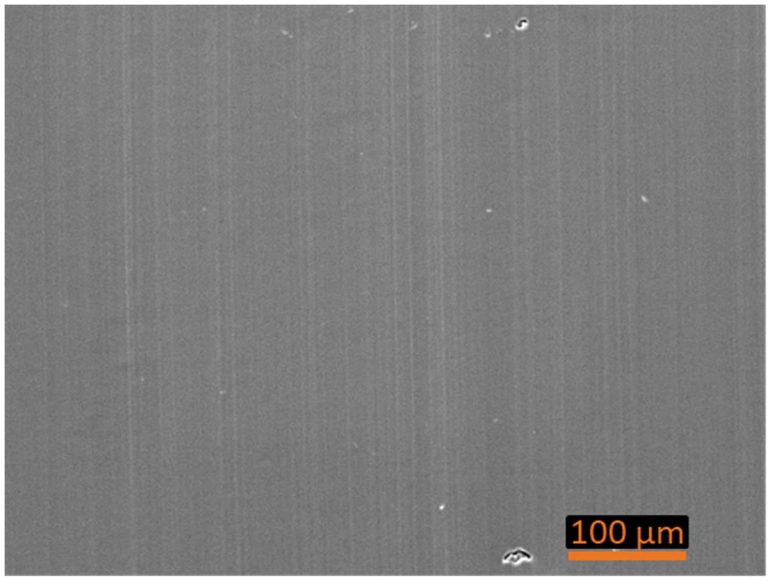

Figure 4.23 the melt-pressed sample shows a smooth surface with almost no porosity.

The melt-pressed sample (Figure 4.23) has an entirely smooth surface. Almost no porosity is present and the SEM confirms that the sample is entirely dense.

4.4.5 Hardness testing

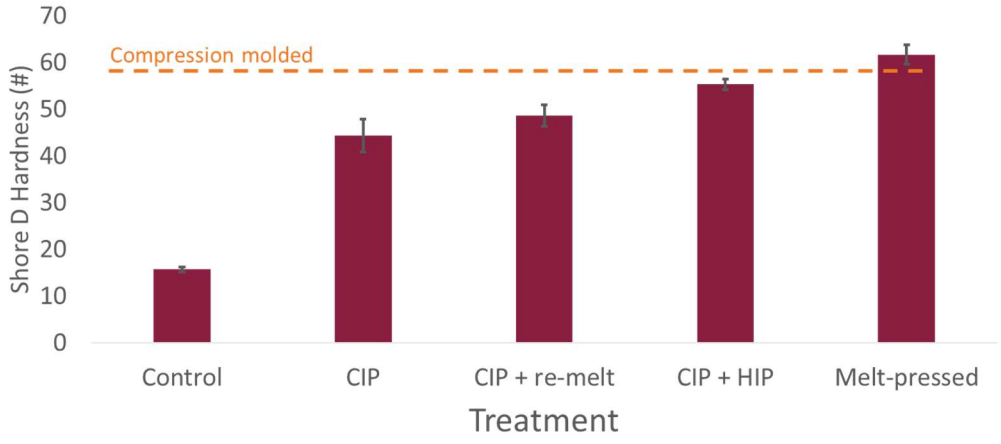

Figure 4.24 hardness increases during each pressurized post-processing step. For the CIP + HIP & Melt-pressed treatment, hardness values similar to compression molded samples are achieved.

As with the density results, hardness measurements can be grouped in a similar set of three tiers (Figure 4.19). Notably, the CIP + HIP treatment was near the hardness reported for this grade of UHMWPE when it is compression molded (Shore D hardness = 58). Figure 4.25 shows that hardness values track well with increases in density, which is expected since porous structures will be less able to resist the needle on the probe of the hardness tester.

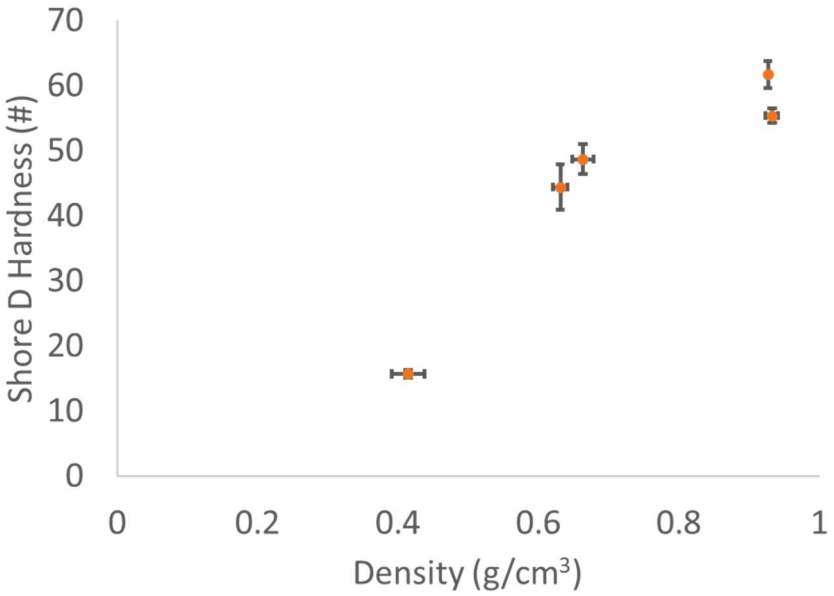

Figure 4.25 hardness increase with density. Notably the density and hardness do not change significantly with the melt post-processing that occurs for the CIP + re-melt sample. Compression molded samples have a reported Shore D hardness of 58.

4.4.6 Tensile testing

There were significant differences in tensile strength at each tested treatment. The combination of densification during CIP and the re-melting of the material during a second thermal post-processing step yielded an increase from 1 MPa from the Control treatment to 9.5 MPa for the CIP + re-melt treatment (Figure 4.26). This increase goes far beyond what would be expected for the 50% increase in density achieved during CIP and suggests that the re-melting of the material heals or coalesces the particles at new interfaces that are much closer contact following CIP.

HIP post-processing causes a nearly 100% increase in tensile strength for the CIP + HIP treatment samples compared to the CIP + re-melt, which demonstrates the importance of applying pressure during thermal post-processing. The increase in crystallinity observed for the CIP + HIP treatment (Figure 4.17) will also contribute to the increase in tensile strength.

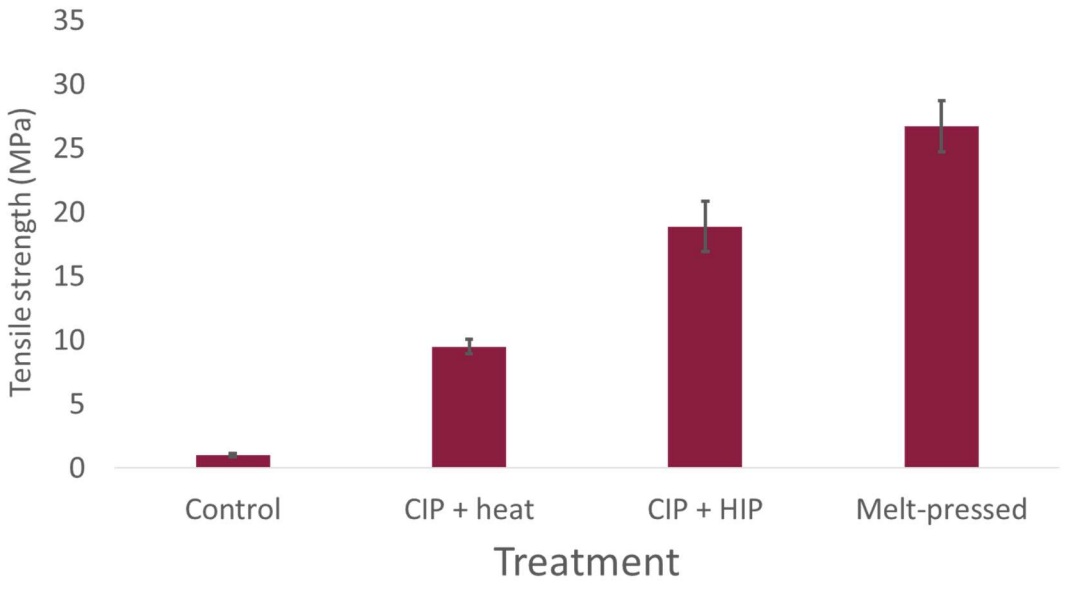

Figure 4.26 tensile tests shows increasing with each post-processing treatment. Though both the CIP + HIP and Melt-pressed treatment both achieved bulk density, the Melt-pressed treatment led to significantly higher tensile strength.

Though the tensile strength for this treatment is much higher than the control and the CIP + re-melt samples, it is still more than 5 MPa lower than the Melt-pressed sample. This is unexpected from the density results, which show that, while the samples have both achieved maximum density, the CIP + HIP sample has a much higher X%. The small amount porosity shown in SEM of the CIP + HIP sample could contribute to some of the loss of tensile strength. In previous UHMWPE processing literature, there is some precedence for the differing properties between densifying nascent, un-melted powder particles and UHMWPE powder that has been melted. Researchers have suggested that there is limited entanglement between UHMWPE that are not nascent powders [30,31]. It is hypothesized that the differences in tensile strength between the CIP + HIP and the Melt-pressed treatment come from this limitation in entanglements that cannot be changed within the processing and post-processing method used in this research.

Strain at break follows a similar trend as density and tensile strength, with large increases following each processing condition. However, the CIP + HIP sample achieves the same value of strain at break as the Melt-pressed sample, which suggests that any limitation from the material being melted before post-processing is not important for this property. It is likely that the slightly higher X% of the CIP + HIP sample does not impact the elongation at break significantly. The CIP + HIP treatment shows a strain at break of 429 ± 2%.

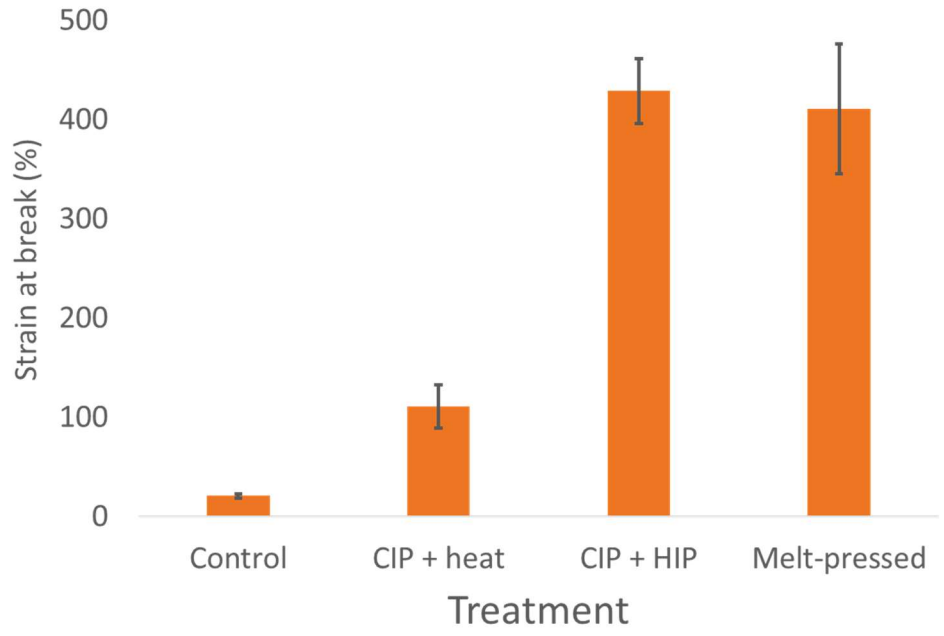

Figure 4.27 though tensile strengths were different between the CIP + HIP and Melt-pressed treatments, the strain at break is similar. This demonstrated the high performance achieved in the printed speciments following the CIP + HIP treatment.

The low density and foam-like structure of the Control treatment led to failure at low stresses and strains and doesn't have enough strength to show a yield stress. After the CIP + re-melt treatment, samples are dense enough and the entanglements between particles are strong enough to show a yield stress and necking of the sample before breaking. Samples from the CIP + HIP treatment not only show necking but also a small amount of strain hardening as the sample exceeds 200% strain. Strain hardening behavior further demonstrates the impact on the mechanical properties from the

densification achieved during this treatment. The Melt-pressed sample shows very similar behavior to the CIP + HIP sample; however, the extent of strain hardening is much higher in the Melt-pressed sample. The differences in tensile strength are achieved during strain hardening, which suggests that the differences in the samples that led to strain hardening are most important to achieving higher tensile strength in the Melt-pressed sample.

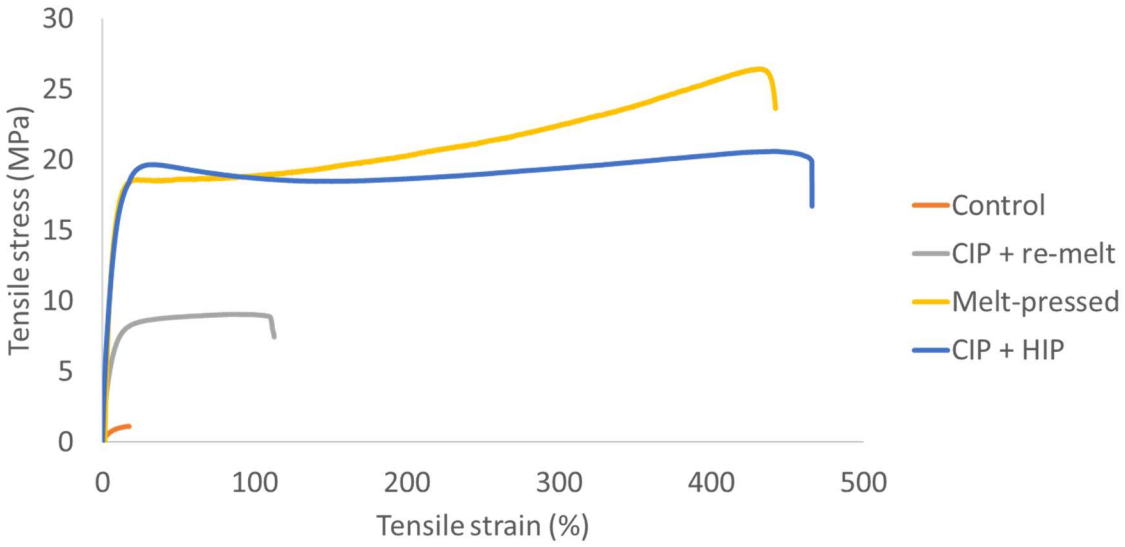

Figure 4.28 as density increases in the sample and particles are able to weld together, there are increases in performance. Between the Control and CIP treatment, a yield stress appears and some necking occurs. For the CIP + HIP treatment, strain hardening occurs, which helps lead to an increased strain at break and tensile strength.

Both 2.5D and complex geometries were processable with the CIP + HIP process chain. Figure 4.17 displays examples of each. Control samples, which have only undergone the first post-processing step, are shown next to each CIP + HIP sample for visual comparison. There is slight yellowing of the CIP + HIP samples, which suggests some degradation has occurred.

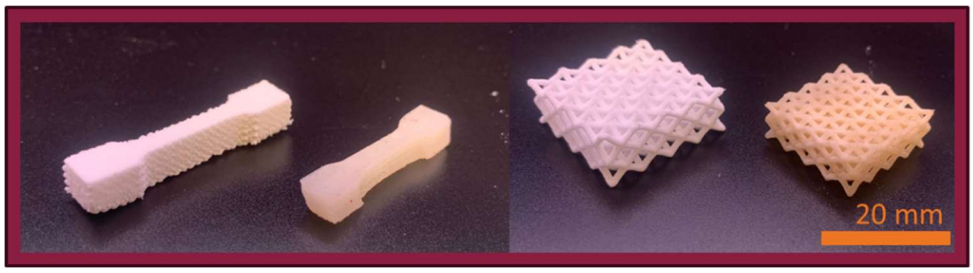

Figure 4.29 control specimens (right) and the same printed geometry after CIP + HIP treatment.

4.5 Conclusions & Future Work

This work demonstrates the first route to achieve fully dense UHMWPE samples using additive manufacturing. A post-processing treatment which enabled manufacturing of the highest performance printed UHMWPE parts was determined in this work and changes in the structure and performance of parts were recorded during each step of post-processing to understand how changes occurred at each post-processing step.

Research on post-processing treatments was conducted to evaluate the effects of post-processing pressure and temperature applied in multiple different ways. UHMWPE's high melt viscosity requires pressure to consolidate the porous as-printed parts. Pressure in each post-processing treatment was applied isostatically in an attempt to maintain part geometry and have isotropic shrinkage. Combining CIP and HIP (324 MPa in CIP, and 18 MPa at 220° C for 2 h for HIP) post-processes enabled production of tensile specimens that achieved the bulk density of UHMWPE. Morphology, both crystalline and macroscopic, density, hardness and tensile properties were all evaluated for each post-processing treatment to understand how these properties changed during each step of post-processing. It was necessary for pressure to be applied in the melt to achieve complete densification of the part. It was not possible to achieve the target density using either method (CIP for pressure and melting for heat) on its own.

Samples processed via the CIP + HIP treatment showed similar mechanical performance to melt-pressed specimens. Tensile strength for this treatment is still lower than the melt-pressed comparison samples; however, previous research suggests that the lower tensile strength observed for the CIP + HIP treatment samples is unavoidable. Samples that were CIPed and simply re-melted did not show significant densification during the melting process. This showed that the

pressure in HIP post-processing was necessary to overcome UHMWPE's melt viscosity and fully density the printed parts.

The pressures and times used during HIP are currently not optimized; exploring alternate post-processing parameters could help to develop higher performing parts during post-processing. The parameters explored in this research achieved fully dense parts via post-processing. Controlling the morphology and entanglements within the part could further increase performance of the post-processed parts. It would be beneficial to determine if the small porosity shown in SEM of the CIP + HIP treated samples could be eliminated with optimized post-processing.

All parts tested in this study were tensile specimens of the same size. In future work, the authors will investigate the effects of the CIP+HIP treatment on a wider variety of geometries, including samples with various thicknesses. Cubes of various sizes should be printed and post-processed to more fully determine whether shrinkage is isotropic and if there is a size limit where this changes.

4.6 References

[1] M. Ziaee, N.B. Crane, Binder jetting: A review of process, materials, and methods, Addit. Manuf. 28 (2019) 781–801. https://doi.org/10.1016/j.addma.2019.05.031.

[2] M. Pagac, J. Hajnys, Q.-P. Ma, L. Jancar, J. Jansa, P. Stefek, J. Mesicek, A Review of Vat Photopolymerization Technology: Materials, Applications, Challenges, and Future Trends of 3D Printing, Polymers. 13 (2021). https://doi.org/10.3390/polym13040598.

[3] I. Gibson, D.W. Rosen, B. Stucker, M. Khorasani, D. Rosen, B. Stucker, M. Khorasani, Additive manufacturing technologies, Springer, 2021.

[4] J.P. Rolland, K. Chen, J. Poelma, J. Goodrich, R. Pinschmidt, J.M. DeSimone, L.M. Robeson, Methods of producing EPOXY three-dimensional objects from materials having multiple mechanisms of hardening, (2018).

[5] J.P. Rolland, K. Chen, J. Poelma, J. Goodrich, R. Pinschmidt, J.M. DeSimone, L.M. Robeson, Methods of producing three-dimensional objects from materials having multiple mechanisms of hardening, (2017).

[6] X. Kuang, Z. Zhao, K. Chen, D. Fang, G. Kang, H.J. Qi, High-speed 3D printing of high-performance thermosetting polymers via two-stage curing, Macromol. Rapid Commun. 39 (2018) 1700809.

[7] D.A. Rau, J. Herzberger, T.E. Long, C.B. Williams, Ultraviolet-Assisted Direct Ink Write to Additively Manufacture All-Aromatic Polyimides, ACS Appl. Mater. Interfaces. 10 (2018) 34828–34833. https://doi.org/10.1021/acsami.8b14584.

[8] J. Herzberger, V. Meenakshisundaram, C.B. Williams, T.E. Long, 3D Printing All-Aromatic Polyimides Using Stereolithographic 3D Printing of Polyamic Acid Salts, ACS Macro Lett. 7 (2018) 493–497. https://doi.org/10.1021/acsmacrolett.8b00126.

[9] C.B. Arrington, D.A. Rau, J.A. Vandenbrande, M. Hegde, C.B. Williams, T.E. Long, 3D Printing Carbonaceous Objects from Polyimide Pyrolysis, ACS Macro Lett. 10 (2021) 412–418. https://doi.org/10.1021/acsmacrolett.1c00032.

[10] R.M. Dunn, K.R. Hart, E.D. Wetzel, Improving fracture strength of fused filament fabrication parts via thermal annealing in a printed support shell, Prog. Addit. Manuf. 4 (2019) 233–243. https://doi.org/10.1007/s40964-019-00081-x.

[11] R.A. Wach, P. Wolszczak, A. Adamus-Wlodarczyk, Enhancement of Mechanical Properties of FDM-PLA Parts via Thermal Annealing, Macromol. Mater. Eng. 303 (2018) 1800169. https://doi.org/10.1002/mame.201800169.

[12] C.A. Chatham, A. Das, T.E. Long, M.J. Bortner, C.B. Williams, Ageing of PBF-Grade Poly(Phenylene Sulfide) Powder and its Effect on Critical Printability Properties, Macromol. Mater. Eng. 306 (2021) 2000599. https://doi.org/10.1002/mame.202000599.

[13] R.D. Goodridge, R.J.M. Hague, C.J. Tuck, An empirical study into laser sintering of ultra-high molecular weight polyethylene (UHMWPE), J. Mater. Process. Technol. 210 (2010) 72–80. https://doi.org/10.1016/j.jmatprotec.2009.08.016.

[14] Y. Khalil, A. Kowalski, N. Hopkinson, Influence of energy density on flexural properties of laser-sintered UHMWPE, Addit. Manuf. 10 (2016) 67–75. https://doi.org/10.1016/j.addma.2016.03.002.

[15] Y. Khalil, A. Kowalski, N. Hopkinson, Influence of laser power on tensile properties and material characteristics of laser-sintered UHMWPE, Manuf. Rev. 3 (2016) 15. https://doi.org/10.1051/mfreview/2016015.

[16] S. Hambir, J.P. Jog, Sintering of ultra high molecular weight polyethylene, Bull. Mater. Sci. 23 (2000) 221–226. https://doi.org/10.1007/BF02719914.

[17] K.M. Kozlovsky, Additive Manufacturing of Ultra-High Molecular Weight Polyethylene under Applied External Pressure, Ph.D., University of Notre Dame, n.d. https://www.proquest.com/docview/2322186293/abstract/252693F78D224297PQ/1 (accessed April 26, 2022).

[18] J.S. Bryant, M.J. Bortner, C.B. Williams, Powder bed fusion additive manufacturing of ultra-high molecular weight polyethylene using a novel laser scanning strategy, Addit. Manuf. (2023) 103885. https://doi.org/10.1016/j.addma.2023.103885.

[19] G.W. Halldin, I.L. Kamel, Powder processing of ultra-high molecular weight polyethylene I. Powder characterization and compaction, Polym. Eng. Sci. 17 (1977) 21–26. https://doi.org/10.1002/pen.760170104.

[20] J.M. Kelly, ULTRA-HIGH MOLECULAR WEIGHT POLYETHYLENE*, J. Macromol. Sci. Part C. 42 (2002) 355–371. https://doi.org/10.1081/MC-120006452.

[21] J. Higgins, D. Schroeder, Using Isostatic Pressing Techniques to Mold Uhmwpe, MRS Online Proc. Libr. OPL. 394 (1995).

[22] J.F. Vega, S. Rastogi, G.W.M. Peters, H.E.H. Meijer, Rheology and reptation of linear polymers. Ultrahigh molecular weight chain dynamics in the melt, J. Rheol. 48 (2004) 663–678. https://doi.org/10.1122/1.1718367.

[23] B. Haworth, N. Hopkinson, D. Hitt, X. Zhong, Shear viscosity measurements on Polyamide-12 polymers for laser sintering, Rapid Prototyp. J. 19 (2013) 28–36. https://doi.org/10.1108/13552541311292709.

[24] J. Benz, C. Bonten, Temperature induced ageing of PA12 powder during selective laser sintering process, in: Dresden, Germany, 2019: p. 140001. https://doi.org/10.1063/1.5084904.

[25] D.M. Sadler, A. Keller, Neutron Scattering of Solution-Grown Polymer Crystals: Molecular Dimensions Are Insensitive to Molecular Weight, Science. 203 (1979) 263–265. https://doi.org/10.1126/science.203.4377.263.

[26] C. Bastiaansen, H. Meyer, P. Lemstra, Memory effects in polyethylenes: influence of processing and crystallization history, Polymer. 31 (1990) 1435–1440. https://doi.org/10.1016/0032-3861(90)90147-Q.

[27] -Gilles de Gennes, “Explosion”upon melting, Comptes Rendus Académie Sci. Sér. 2 Mécanique Phys. Chim. Astron. (1995) 363–365.

[28] P.J. Barham, D.M. Sadler, A neutron scattering study of the melting behaviour of polyethylene single crystals, Polymer. 32 (1991) 393–395. https://doi.org/10.1016/0032-3861(91)90440-T.

[29] C. Buckley, J. Wu, D. Haughie, The integrity of welded interfaces in ultra high molecular weight polyethylene: Part 1—Model, Biomaterials. 27 (2006) 3178–3186. https://doi.org/10.1016/j.biomaterials.2006.01.030.

[30] Y.-Q. Xue, T.A. Tervoort, P.J. Lemstra, Welding Behavior of Semicrystalline Polymers. 1. The Effect of Nonequilibrium Chain Conformations on Autoadhesion of UHMWPE, Macromolecules. 31 (1998) 3075–3080. https://doi.org/10.1021/ma970544u.

[31] T. Deplancke, O. Lame, F. Rousset, R. Seguela, G. Vigier, Mechanisms of Chain Reentanglement during the Sintering of UHMWPE Nascent Powder: Effect of Molecular Weight, Macromolecules. 48 (2015) 5328–5338. https://doi.org/10.1021/acs.macromol.5b00618.

[32] N.C. Parasnis, K. Ramani, Analysis of the effect of pressure on compression moulding of UHMWPE, J. Mater. Sci. Mater. Med. 9 (1998) 165–172. https://doi.org/10.1023/A:1008871720389.

[33] A.Y. Kumar, Y. Bai, A. Eklund, C.B. Williams, The effects of Hot Isostatic Pressing on parts fabricated by binder jetting additive manufacturing, Addit. Manuf. 24 (2018) 115–124. https://doi.org/10.1016/j.addma.2018.09.021.

[34] A. Kumar, Y. Bai, A. Eklund, C.B. Williams, Effects of Hot Isostatic Pressing on Copper Parts Fabricated via Binder Jetting, Procedia Manuf. 10 (2017) 935–944. https://doi.org/10.1016/j.promfg.2017.07.084.

[35] A.Y. Kumar, J. Wang, Y. Bai, S.T. Huxtable, C.B. Williams, Impacts of process-induced porosity on material properties of copper made by binder jetting additive manufacturing, Mater. Des. 182 (2019) 108001. https://doi.org/10.1016/j.matdes.2019.108001.

[36] A. Kaletsch, S. Qin, S. Herzog, C. Broeckmann, Influence of high initial porosity introduced by laser powder bed fusion on the fatigue strength of Inconel 718 after post-processing with hot isostatic pressing, Addit. Manuf. 47 (2021) 102331. https://doi.org/10.1016/j.addma.2021.102331.

[37] W. Tillmann, C. Schaak, J. Nellesen, M. Schaper, M.E. Aydinöz, K.-P. Hoyer, Hot isostatic pressing of IN718 components manufactured by selective laser melting, Addit. Manuf. 13 (2017) 93–102. https://doi.org/10.1016/j.addma.2016.11.006.

[38] N. Van De Werken, P. Koirala, J. Ghorbani, D. Doyle, M. Tehrani, Investigating the hot isostatic pressing of an additively manufactured continuous carbon fiber reinforced PEEK composite, Addit. Manuf. 37 (2021) 101634. https://doi.org/10.1016/j.addma.2020.101634.

[39] C.S. Abbott, M. Sperry, N.B. Crane, Relationships between porosity and mechanical properties of polyamide 12 parts produced using the laser sintering and multi-jet fusion powder bed fusion processes, J. Manuf. Process. 70 (2021) 55–66. https://doi.org/10.1016/j.jmapro.2021.08.012.

[40] C.E. Zawaski, Process and Material Modifications to Enable New Material for Material Extrusion Additive Manufacturing, (2020).

Chapter 5: Powder bed fusion of polypropylene-ethylene copolymers

Coauthor: Michelle Pomatto

5.1 Abstract

Polypropylene has long been a material of interest for additive manufacturing to enable both functional prototyping of this commonly injection molded commodity polymer and to create end-use products. However, due to its high crystallization rates relative to polyamides, polypropylene has proven difficult to process without warpage occurring. Creating random copolymers of polypropylene and polyethylene is one method for controlling crystallization kinetics; however, there are no established process-structure-property relationships for processing these copolymers. Increasing ethylene content is shown to decrease crystallization kinetics and the onset of melting for copolymers. Through a combination of experimental printing trials and flash differential scanning calorimetry, it was found that, for a 2.2% ethylene copolymer, the decrease in these two properties led to a material that was easier to process without warpage than the polypropylene homopolymer. However, at 4.9% ethylene, the onset of melting was reduced so significantly that crystallization kinetics at this temperature were more rapid than the 2.2% ethylene sample, and the polymer powder was more likely to warp during processing. Tensile strength decreased and strain at break increased with increasing ethylene content, which suggests that ethylene content can also be used to tune mechanical performance of polypropylene materials in PBF.

5.2. Introduction

5.2.1 Powder bed fusion of polypropylene

Polypropylene (PP) has recently become a frequently studied material for processing in powder bed fusion (PBF), and has been successfully printed many times, but a fundamental understanding

of its processing has yet to be established [1–6]. There is particular interest in polypropylene because of its powder reusability in the PBF process. Polypropylene, and all polyolefins, are not synthesized via condensation reactions, which keeps these polymers from increasing in molecular weight—and therefore, viscosity—during printing via post-condensation reactions. Post-condensation reactions that occur in polyamide materials can lead to increases in molecular weight (MW) limit powder reuse [7]. This difference greatly aids in the reuse of these PP powder and current research suggests there is little impact on printed PP part properties with powder reuse [6,8]. This key difference aids in reducing waste during PBF processing, which makes processing more efficient and sustainable.

5.2.2 Understanding crystallization during powder bed fusion

One key goal during PBF processing—and all additive manufacturing (AM) processing of semicrystalline polymers—is to keep crystallization rates low to reduce the rate of shrinkage of printed layers, and therefore mitigate part warpage [9,10]. Samples crystallize during the printing process as they cool and stay at bed temperature, which can lead to warping (and therefore potential for part failure during recoating) throughout the entire PBF process [11]. The idea of a supercooling window, a long-established paradigm in PBF that suggests no crystallization happens at a chosen bed temperature, does not accurately reflect the observed behavior for all polymers, and therefore each polymer system merits analysis of its crystallization kinetics to understand crystallization during printing [11,12].

One robust method for achieving a general understanding of crystallization kinetics in polymers is to measure isothermal crystallization rates, which can be represented as a crystallization half time ($t_{1/2}$). A $t_{1/2}$ is the time at which the fractional crystallinity reaches 50% of the total crystallizable content at the measured temperature. Isothermal crystallization kinetics of PBF materials have

been studied by other researchers using both differential scanning calorimetry (DSC) and fast scanning calorimetry (FSC) [12–17]. To give perspective on crystallization half times ($t_{1/2}$) of common PBF materials, Zhao et al. observed $t_{1/2}$ values ranging from 2-25 minutes at process-relevant temperatures for their polyamide [18]. Paolucci et al. used FSC to measure $t_{1/2}$ values for another commercial polyamide and observed similar values. Chen et al. studied isothermal crystallization of PEEK with temperatures ranging from 1 to 16° C below the onset of melting for their polymer. The observed $t_{1/2}$ values ranged from 2.5 minutes at the lowest temperature to 35.5 minutes at the highest measured temperature. One conclusion made in this work was that a bed temperature should be set according to when $1/t_{1/2}$ approaches zero [19]. However, this conclusion essentially suggests that $t_{1/2}$ values for a PBF material should be very large, which is self-evident. Faster crystallizing polymers may have no $t_{1/2}$ values that meet this criterion, which suggests its limited applicability.

Controlling crystallization and shrinkage during processing can be especially challenging when processing PP due to the relatively rapid crystallization kinetics of this polymer [1]. Multiple strategies to address warpage during AM of semi-crystalline polymers have been employed. In MatEx of polypropylene, Bachhar et al. changed part geometry to create a larger surface for a part to adhere to the print-bed and therefore reduce the effects of warpage, though not necessarily changing crystallization within the part [20]. This approach is less relevant to PBF where parts are not adhered to the build-plate and instead rest on loose powder. Other researchers have explored compositional changes to their materials to reduce warpage. Das et al. printed PP blends that included a slower crystallizing PP component to slow crystallization and reduce warpage [13]. Other researchers studying PBF of semicrystalline polymers addressed problems with part warpage by adjusting and optimizing process parameters [12].

In the research presented in this chapter, changes are made to the material's chemical structure to understand how changes in crystallization kinetics impact the PBF process. The specific change is the addition of ethylene content to polypropylene to make a polypropylene-ethylene copolymer.

5.2.3 Polypropylene-ethylene copolymers

Polymerization of polypropylene-ethylene random copolymers have been shown to have decreasing amounts of crystallinity as ethylene (Et) content in the copolymer increases [21,22]. Addition of ethylene content has also demonstrated lowering spherulitic growth rates and crystallization rates [22,23]. Each of these results comes from the ethylene repeat units disrupting the PP crystals that form during processing of these materials. Minimal research has been conducted on PBF of PP-PE copolymers. Tan et al. studied a PP homopolymer and an 11% Et copolymer [24]. They observed a multiple order of magnitude difference in elongation at break in the copolymer compared to the PP homopolymer. Higher tensile strengths were also observed in the copolymer. However, the melt viscosity was two orders of magnitude higher for the copolymer, which suggests the molecular weight (MW) of the copolymer is much higher than the homopolymer. For this reason, it is difficult to fairly compare the two samples' mechanical properties [24]. The approach of adding a comonomer to influence crystallization kinetics was also explored for a polyaryletherketone (PAEK) by Yi et al. [17].

It is clear from this initial research that copolymerization is one avenue for expanding the breadth of material properties of PBF materials. Controlling ethylene content is one pathway for tuning crystallization kinetics and overall crystallinity in PBF printed PP. It is hypothesized that increased in ethylene content, which decreases crystallization kinetics, will reduce the chance of warpage during the printing process and increase processability.

5.2.4 Context and Aims

Generally, the goal of this research is to understand how changes in crystallization kinetics influence a polymer's PBF processability and the resulting printed structure and properties. PP-PE copolymers are used as an example system where small compositional changes significantly change crystallization kinetics of the material. It is hypothesized that samples with slower crystallization kinetics will be more easily processable due to their slower shrinkage during cooling, which makes warpage less likely. This research also helps further the general understanding of processing PP-PE copolymers in PBF, which have the potential to achieve higher elongations at break than is often observed in PBF-processed materials. To test this hypothesis, copolymers with % Et ranging from 0 to 4.9% are studied.

5.3. Materials and Methods

To develop an understanding of how the addition of ethylene content to polypropylene impacts the copolymers' process-structure-property relationships, fundamental characterization of the raw and printed materials was completed. Mechanical testing of printed samples was used to evaluate how % Et impacts printed part properties. To understand how changes in % Et impacts processability, the authors examined the longest layer cycle time a material could be printed without warping.

5.3.1 Material characterization

5.3.1.1 Powder analysis

This work was conducted on three different powders with molecular weight, ethylene content and particle sizes as reported by the material manufacturer in Table 5.1.

Table 5.1 Particle sizes and size distributions of the PP-PE copolymers, as reported from the material supplier.

Ethylene content (%)	d10 (µm)	d50 (µm)	d90 (µm)
0	42	85	151
2.2	37	81	164
4.9	36	71	129

5.3.1.2 Thermogravimetric analysis (TGA)

Samples were evaluated using thermogravimetric analysis (TGA) to understand at which temperature volatilization of the material would occur. Samples were prepared by vacuum drying overnight at 80° C. All analyses were performed with a ramp rate of 20° C/min to 800° C in a nitrogen atmosphere in a TA Instruments TGA Q550 thermogravimetric analyzer.

5.3.1.3 Differential Scanning Calorimetry of neat powder

A TA instruments Q2000 differential scanning calorimeter (DSC) was used to understand the melting behavior of each polymer. Samples were heated from 0° C to 200° C at 10 °C/min in nitrogen and isothermally held at 200° C for 3 minutes to remove all thermal history. Samples were then cooled from 200° C to 0° C at 10 °C/min to observe changes in heat flow associated with crystallization upon cooling. This measurement was used to determine the onset of melting for each polymer, which represents the maximum possible bed temperature that can be used during printing without melting occurring prior to energy deposition. This measurement also helped to characterize the shape of the melting endotherm and to determine differences in crystallinity between each polymer.

5.3.1.4 Fast scanning calorimetry (FSC)

A Mettler Toledo Flash DSC 1 with a Huber intra cooler TC100 was employed to analyze the crystallization kinetics of the PP and each copolymer. Prior to evaluation, the chip sensors were individually conditioned, and temperature corrected utilizing Mettler Toledo supplied calibration data and following Mettler Toledo instrument specifications. The temperature was experimentally calibrated by an indium standard. The onset of indium melting versus heating rate was used to determine the corrected horizontal shift of the experimental melting profiles. All experiments were conducted in an ultra-high purity N_2 gas environment with a flow rate of 60 mL/min to limit oxidation and moisture in the sample chamber. Small (<10 μm diameter) powder particles were used for experiments. All samples were pre-melted at 5 K/s to 200 ºC for 1 s to establish good thermal contact. The sample mass was estimated from the change in heat capacity at the glass transition temperature from an amorphous sample with all samples measured between 4 μg – 9 μg. Experiments were repeated with fresh samples and over multiple chip sensors to ensure reproducibility.

The isothermal crystallization temperatures (T_{iso}) between 0° C to 120° C were analyzed. After removing thermal history at 200° C for a minimum of 1 s, the sample was quenched at -5,000 K/s to the respective T_{iso} and held for varying amounts of time (0.001 s – 200 s). After holding for the specific amount of time, the sample was quenched at -5,000 K/s to below the T_g to arrest any further crystallization. The partially crystallized sample was then heated to 200° C at a heating rate of 10,000 K/s to measure the melting endotherm upon heating. This rate was chosen because it eliminated any possibility of crystallization during heating, which increases the accuracy of the measurement. The maximum isothermal crystallization time (t_{iso}) was determined as when the melting enthalpy remained at a constant value with increasing t_{iso}. The maximum isothermal

crystallization time is dependent on T_{iso}. The observed melting enthalpy versus t_{iso} was used to calculate crystallization half-time ($t_{1/2}$) for PP and copolymers over a range of isothermal crystallization temperatures.

5.3.1.5 Melt rheology

Powders were melt-pressed into a 1 mm thick, 25 mm diameter disk at 200° C to prepare samples for melt rheology measurements. A frequency sweep with frequencies ranging from 0.1-100 rad/s was performed for each sample at 200° C. Samples were tested with a 1 mm gap using a 25 mm parallel plate geometry in a TA ARES-G2 rheometer with a strain of 0.1%.

5.3.2 Powder Bed Fusion Processing

A Prodways Promaker P2000 HT was used for all printing conducted for this research. The printer uses a 60 W, CO_2 laser with controllable beam velocity, hatch spacing and laser power.

Printing parameters (Table 5.2) which led to maximum densification in the printed parts, which is indicated by achieving 95% relative density, for each sample were determined and used to print each polymer [26]. The mechanical properties of these parts were taken to be representative of differences between the different polymers. Tensile bars were printed for mechanical testing, and various complex geometries were printed to demonstrate printability of complex geometries for each polymer.

Table 5.2 PBF processing parameters. All parts were printed with the same set of laser parameters; however, the bed temperature was adjusted for each polymer, as informed by DSC results.

Et (%)	T_{bed} (°C)	Laser power (W)	Beam velocity (mm/s)	Hatch spacing (mm)	Energy density (J/mm^2)
0	103	20	1725	0.254	0.046
2.2	109	20	1725	0.254	0.046
4.9	132	20	1725	0.254	0.046

5.3.3 Printed part characterization

5.3.3.1 Density

Printed part density was measured using the Archimedes method, or ASTM D792 method A, as is common for PBF parts [25]. Ethanol was used as the medium for this measurement. Density was used as the metric to determine if printed samples should be considered to have properties representative of the material. Here, a relative density of approximately 95% is used because this is the maximum theoretical density for samples printed via PBF [26]. Although there is some slight difference in theoretical maximum density between different grades of PP and density differences between PP and PP-PE copolymers, all samples' relative densities were determined using a theoretical maximum density of 0.92 g/cm^3.

5.3.3.2 Tensile testing

Printed tensile specimens were tested using an Instron 5944 tensile tester and a 2 kN load cell. Samples were tested using a strain rate of 5 mm/min. This evaluation was used to understand differences in tensile strength and elongation at break of printed parts for each polymer. Knowing the changes in these values with changes in Et content help determine the impact structural differences have on the final properties of printed parts.

5.3.3.3 Differential scanning calorimetry (DSC) of printed parts

A TA instruments Q2000 differential scanning calorimeter was used to understand the crystalline morphology of the printed parts for each polymer. Samples were heated from 0° C to 200 °C at 10° C/min in nitrogen and isothermally held at 200 °C for 3 minutes to remove all thermal history. Samples were then cooled from 200° C to 0° C at 10° C/min to observe changes in heat flow associated with crystallization upon cooling. This measurement was used to determine the onset of melting for each polymer, which represents the maximum possible bed temperature that can be used during printing without melting occurring prior to energy deposition. Comparing the results of this measurement against the raw powder and among the printed specimens elucidates changes in crystallinity induced by processing and differences in crystallinity between each polymer, respectively.

5.3.4 Warpage experiment

5.3.4.1 Warpage experimental design

An experiment was designed to assess resistance to warpage during processing. To accomplish this, 20 x 20 x 20 mm cubes were printed. This part size was chosen to be representative of a reasonable cross-sectional area for a part in PBF and has been used by other researchers previously when collecting data to model PBF [27]. Samples were printed in triplicate. Print failure was also recorded, where print failure is defined as a sample being pushed out of position during recoating. Samples for each material were printed at bed temperatures just below their onset of melting. Specifically, the 0% Et sample was printed at T_{bed} = 103° C, 2.2% Et was printed at T_{bed} = 123° C and 4.9% Et was printed at T_{bed} = 137° C. These bed temperatures were considered the maximum possible temperature at which each material could be printed.

A 'printing stress test' was performed to determine each material's resistance to warpage as layer time increased. Longer layer times allow scanned layers to cool for longer and reach lower temperatures before scanning of the next layer. This increases the opportunity for crystallization and warpage to occur, which can cause layer shifting and print failure. A polymer that does not warp, even as layer times increase, is defined as "more processable." The laser parameters used for each sample were the same as the parameters used to print full parts, as reported in Table 5.2. Each layer cycle includes powder recoating and laser scanning of the layer, in that order. Within process settings for a print, the minimum layer cycle time can be set. If recoating of a layer and scanning take less time than the minimum layer cycle time, the printer will wait the remaining time before powder recoating for the next layer occurs. The first layer time tested for all samples was 60 s. This is far above a reasonable layer time in the printing process, which made it valuable for the stress test. If a material couldn't successfully print 10 layers without warpage at a 60 s layer time, the layer time was dropped to 40 s. This test was repeated and dropped to 20 s if a sample was still not printable. The layer in which failure occurred during printing was recorded along with the success or failure of a material to print at each minimum layer cycle time.

5.4 Results

5.4.1 Material characterization

5.4.1.1 Thermogravimetric analysis (TGA)

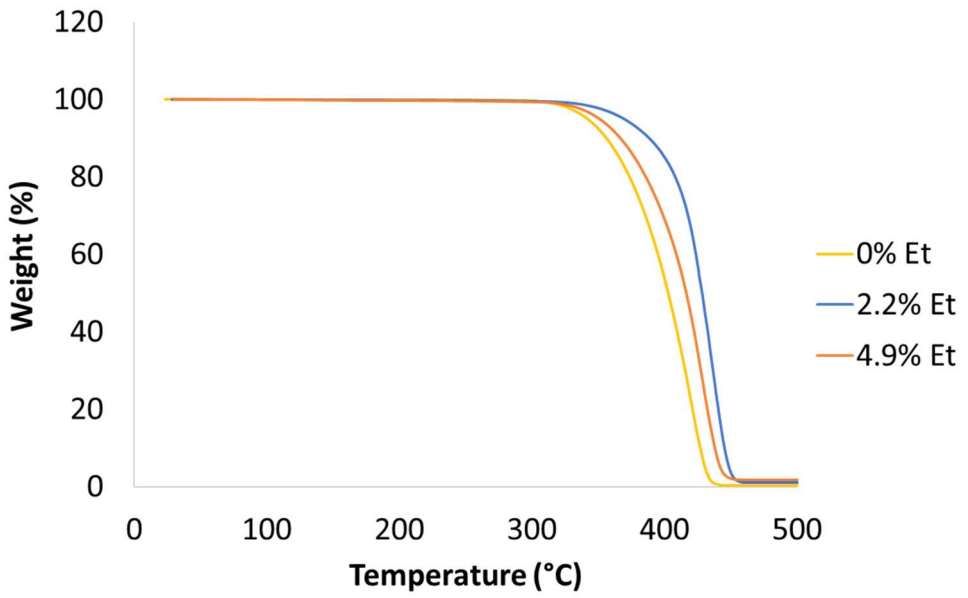

Figure 5.30. TGA data shows all samples begin to volatize between 340 and 370° C. These temperatures are well above the temperature expected during PBF processing.

Results from TGA show that each sample volatizes at roughly the same temperature (340-370° C). This is expected due to the samples' similar chemical composition and molecular weight. Samples also have temperature of 5% degradation (TD_5) values that are much greater than any of the samples' melting endotherms, which means volatilization during PBF processing is unlikely. This result also confirms that any differences observed in the processing and properties of printed parts are not due to changes in volatility.

5.4.1.2 Differential scanning calorimetry (DSC) of neat material

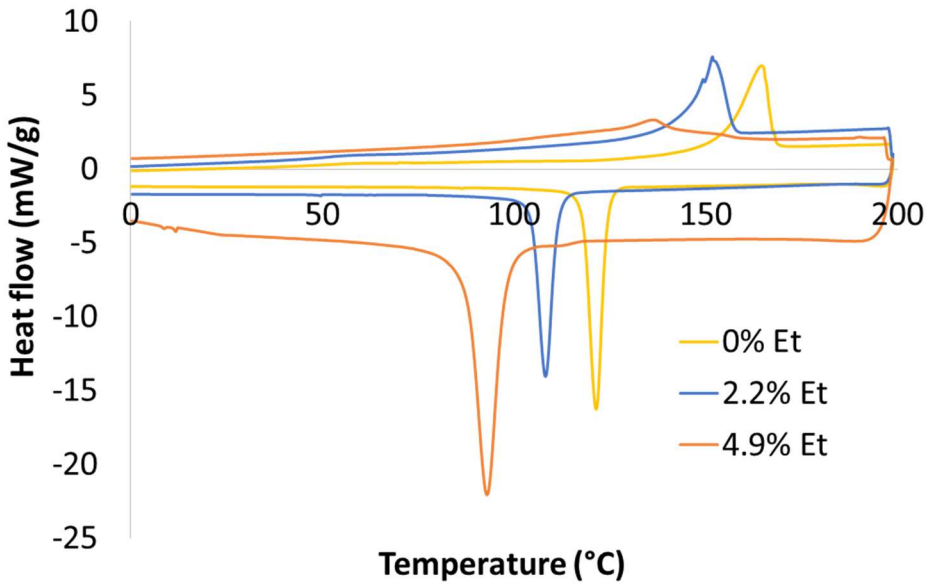

Figure 5.31. DSC shows that peak melting temperatures shift significantly lower as ethylene content increases. Melting endotherms also broaden significantly, which limits the usable T_{bed} range for the samples with higher ethylene content.

The addition of ethylene content caused significant changes to the onset of melting and degree of crystallization of the polymers. As seen in Figure 5.2, the onset of melting decreased as ethylene content is increased. This change will directly impact the usable bed temperature (T_{bed}) range for the material. When setting T_{bed}, a material must be below its onset of melting to avoid any coalescence between particles prior to energy deposition. If this temperature boundary is exceeded, some amount of coalescence will occur between particles in the build area regardless of laser scanning path and lead to limited powder reusability at best and a coalesced chunk of powder (commonly referred to as, "bricking,") at worst. With this being the case, the difference in maximum usable bed temperature between the 0% Et PP homopolymer, and the 4.9 % Et copolymer is approximately 30° C (Table 5.3).

Table 5.4 onset of melting and peak melting temperature ($T_{m,peak}$) shift significantly with the small increases in ethylene content. Onset of crystallization, which is often reported in PBF literature, is not reported here as it only represents crystallization at one specific cooling rate. Fast scanning calorimetry (FSC) is used to fully characterize crystallization at different temperatures.

Et (%)	Onset T_m (°C)	$T_{m,peak}$ (°C)
0	137.2	165.2
2.2	123.9	151.0
4.9	103.4	137.8

5.4.1.3 Fast scanning calorimetry (FSC)

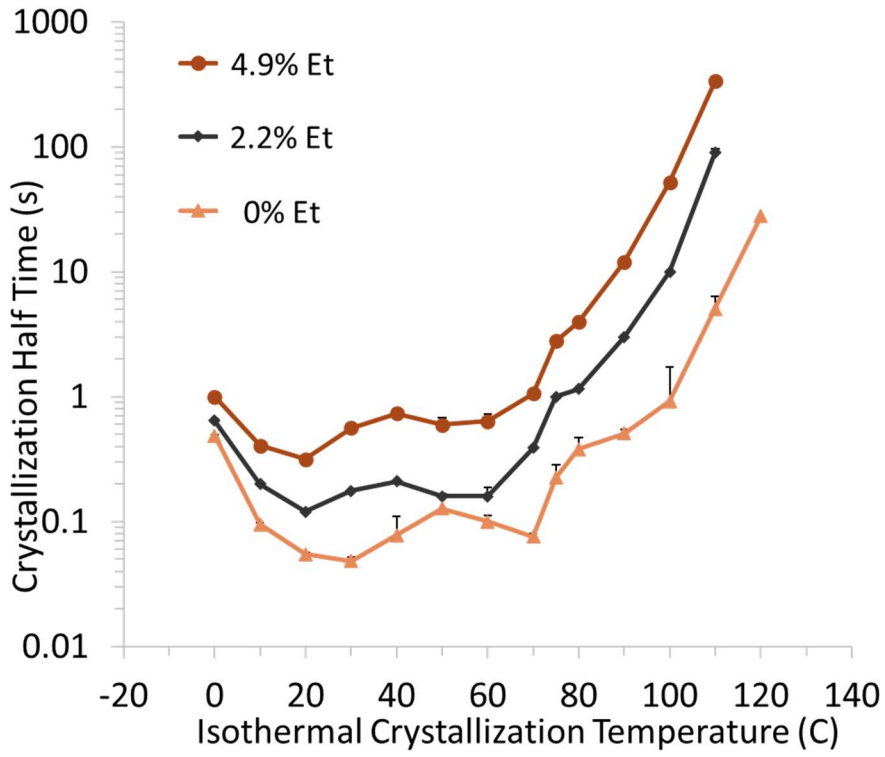

Figure 5.3 Flash DSC elucidates crystallization half times. Half times increase at each temperature as ethylene content increased.

Flas DSC measurements elucidate that increasing ethylene content increases the crystallization half times ($t_{1/2}$) at all measured temperatures, as anticipated (Figure 5.3). The ethylene monomers randomly distributed within each polymer chain act as defects during crystallization, which slow down this process. Isothermal crystallization experiments do not correspond exactly to the PBF process, which is non-isothermal; however, they offer insight into fundamental differences in crystallization kinetics between each polymer. It is hypothesized that higher crystallization half-times will lead to less warpage during the printing process, since slower crystallization corresponds to slower shrinkage, which causes warpage during PBF.

5.4.1.4 Melt rheology

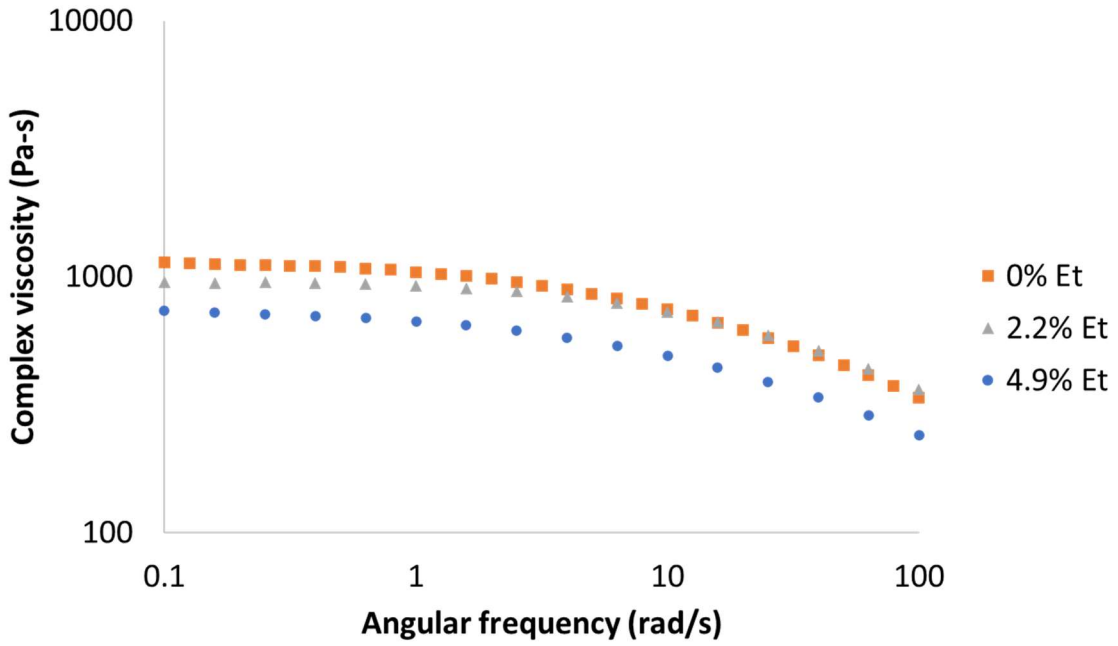

Figure 5.4 rheometry of each polymer shows only minor differences in zero-shear viscosity between samples.

All samples showed similar zero-shear viscosities (the viscosity value relevant to PBF), and are in a standard range for PBF materials (Figure 5.4). This suggests that there will not be difficulties coalescing any of these materials to form fully dense parts during laser scanning.

5.4.2 Printed part analysis

Figure 5.5 Complex 3D geometries were printable with each material.

Multi-layered, complex parts were printable with each polymer regardless of ethylene content. Samples achieved their maximum possible density during the printing process (~95% relative density) [26]. The reported properties should not be treated as fully optimized; however, reaching complete densification is a critical factor for mechanical properties of a part.

Table 5.4 Aall densities for printed parts were within the ~95% density range expected for fully dense parts in PBF.

Et (%)	Density (g/cm^3)	Relative density (%)
0	0.88 ± 0.05	97.3 ± 0.26
2.2	0.85 ± 0.03	94.1 ± 0.02
4.9	0.86 ± 0.01	95.1 ± 0.32

5.4.2.1 Differential scanning calorimetry (DSC) of printed parts

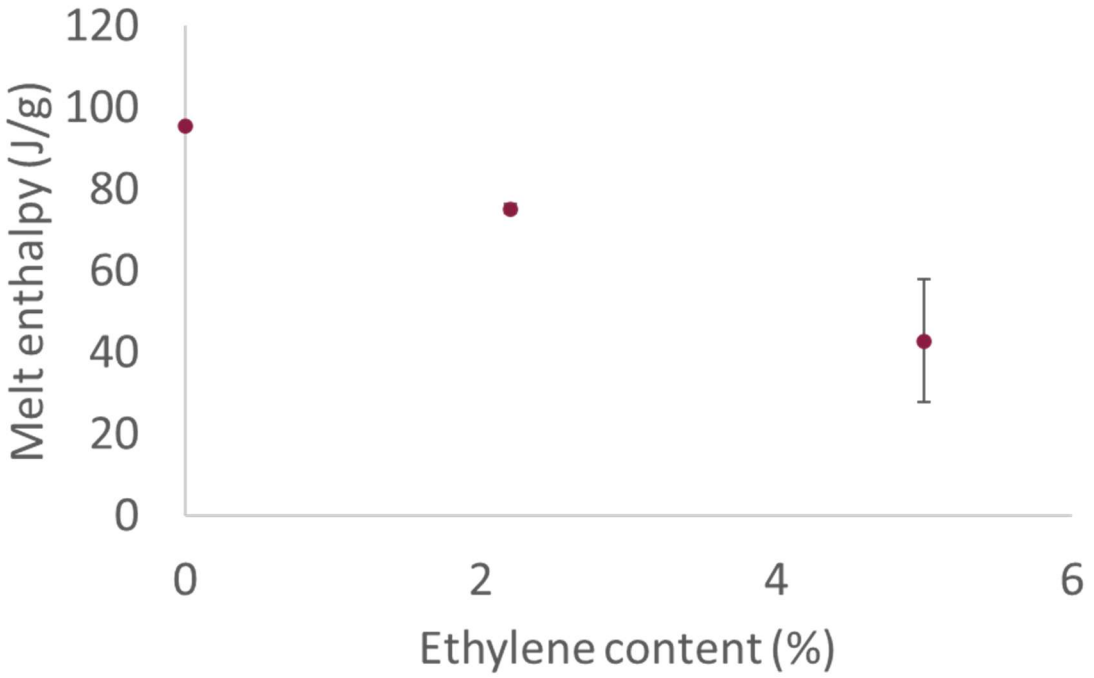

Figure 5.6 DSC of printed parts elucidates that ethylene content led to decreases in the melt enthalpy. This result is expected because ethylene units disrupt the formation of polypropylene crystals. Standard deviation values are included for each ethylene content. However, for 2.2 and 0% ethylene, the standard deviation is too small to appear on the plot.

Printed parts were evaluated with DSC and showed a decrease in crystallinity as ethylene content increased. This result was expected based on the lower crystallinity of the starting materials. The melt enthalpy of the 4.9% Et sample is less than half of the homopolymer's enthalpy.

5.4.2.2 Tensile testing

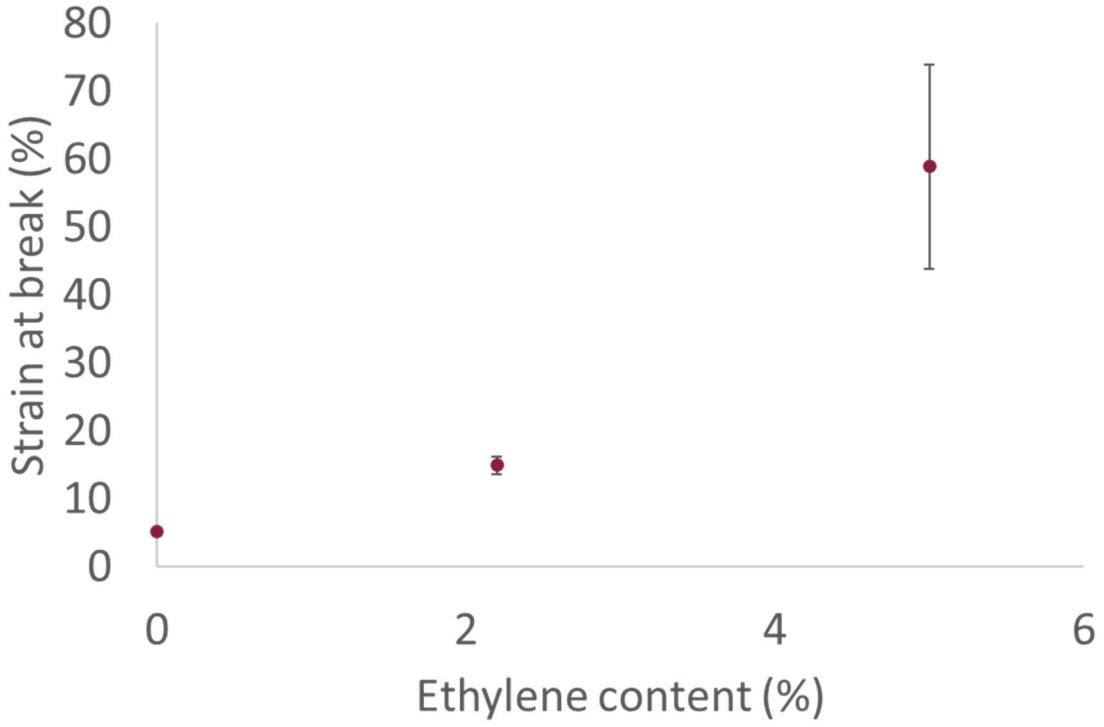

Figure 5.7 Ethylene content increases change the strain at break significantly even though the content is still quite low. These results show the tunability of this mechanical property with changes in the material chemistry.

Typically, strain at break in PBF processed materials is somewhat low due to the high degree of crystallinity that develops as printed parts are held at temperatures near melting for long times during cooling [1]. As seen in Figure 5.7, strain at break changed dramatically with increases in ethylene content. Between 0 and 4.9% Et, samples showed an order of magnitude increase in strain at break. This higher strain at break is caused by the lower amount of crystallinity and smaller crystals found in the printed samples. This much higher elongation at break could be valuable in applications where the low strain at break of many PBF materials is insufficient.

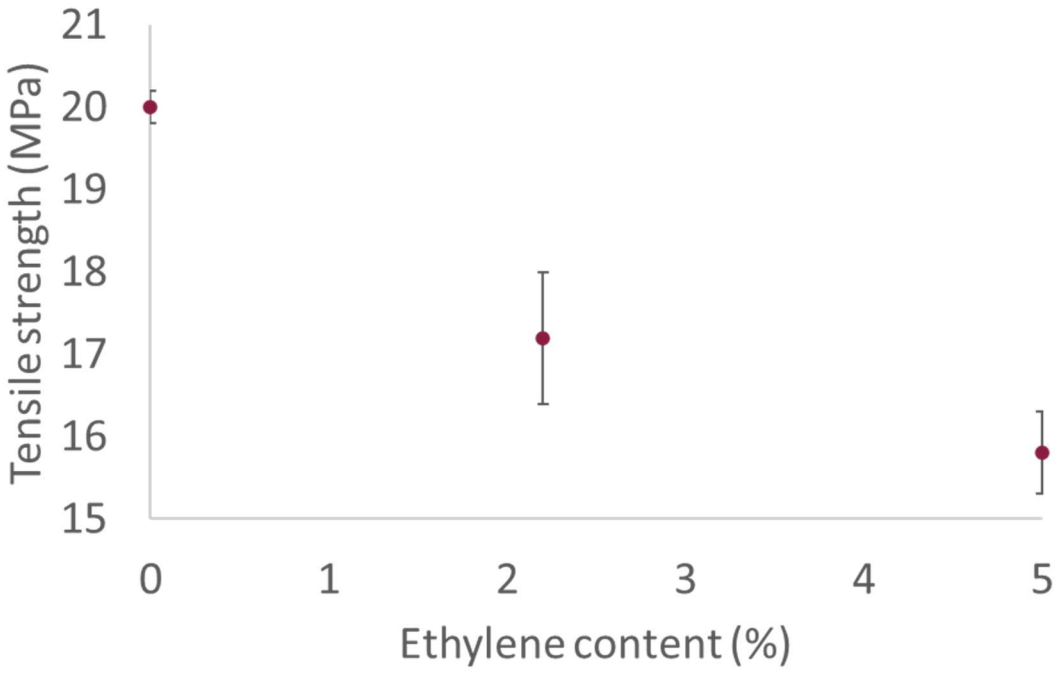

Figure 5.8 changes in tensile strength are opposite those of strain at break. This is consistent for what would be expected with decreasing crystallinity in a polymer.

The increase in strain at break does come at the cost of lower tensile strength. As seen in Figure 5.8, tensile strength decreases approximately 5 MPa with the addition of 4.9% Et, when compared to the 0% Et homopolymer. These differences are consistent with the behavior expected for samples with lower crystallinity.

Table 5.5 Increases in ethylene content reduces ethylene content and impacts the mechanical behavior of the tested specimens. Increases in ethylene content yield weaker parts that have higher strain at break.

% Et	Tensile strength (MPa)	Strain at break (%)	Melt enthalpy (J/g)
0	20 ± 0.2	5.2 ± 0.2	95.4
2.2	17.2 ± 0.8	14.9 ± 1.2	75.2
4.9	15.8 ± 0.5	58.9 ± 15	42.8

5.4.3 Warpage experiment

A material's resistance to warpage was predicted at each bed temperature by estimating the $t_{1/2}$ at the chosen bed temperature using curves fitted to the isothermal crystallization data (Table 5.6). Here, a higher $t_{1/2}$ value is expected to lead to printability at longer layer cycle times. Additionally, if the isothermal multiple layer cycles occur before one $t_{½}$ for a sample, it is expected that the material would be printable at this layer time. Estimations from the FSC isothermal crystallization data (Figure 5.3) show that the 2.2% Et sample has the highest $t_{1/2}$ by far at its maximum usable bed temperature (123° C, from Table 5.3), while each other polymer had $t_{1/2}$ values an order of magnitude lower than the 2.2% Et sample. Notably, the magnitude of these $t_{1/2}$ values was on the order of the layer time (i.e., 10s of seconds).

Table 5.5 samples failed during printing at layer times proportional to their predicted $t_{1/2}$ values.

Et (%)	T_{bed} (°C)	$t_{1/2}$ at T_{bed} (s)	60 s, printable? (Yes/No), Layer of failure (#)	40 s, printable? (Yes/No), Layer of failure (#)	20 s, printable? (Yes/No,) Layer of failure (#)
0	137	41	No, 1	No, 1	Yes
2.2	123	425	Yes	-	-
4.9	103	83	No, 3	No, 6	Yes

As seen in Table 5.6, the performance of each material during the warpage experiment matched expectations set by the estimated $t_{1/2}$ values. Higher $t_{1/2}$ values led to less warpage during the tests. Here, less can mean both: being printable at a higher minimum layer and failing at a higher layer number at a specific minimum layer time. Both the 0 and 4.9% Et samples were only able to be printed without warpage over 10 layers when the layer time was 20 s. The 0% sample failed after just one layer of printing for both 60 s and 40 s layer times. The 4.9% sample showed more unique failure in that the warpage that ultimately led to failure of the print occurred over multiple layers. This demonstrates previous layers crystallizing and warping while subsequent layers are printed. Layers can warp in concert to cause overall failure during printing of the part.

5.5 Conclusions

Three different polypropylene materials with ethylene contents ranging from 0 to 4.9% were successfully processed via PBF and analyzed. Fundamental properties of each powder material were characterized and showed that, while each sample's crystallinity changed significantly with ethylene content, other material properties important to processing (degradation temperature, IR-absorptivity, melt viscosity) were consistent across samples. Samples were also able to reach their maximum density during printing, which allowed for equal comparison of mechanical properties. These results help to show that all differences observed during processing and in the printed part properties come from differences in crystallinity and crystallization kinetics rather than other properties.

Increases in ethylene content had many impacts on the processing and properties of materials. Changes included a downward shift of the peak melting temperature and onset of melting temperature, broadening of the melting endotherm, and a decrease in melt enthalpy. Not only did the increase in ethylene content change the structure of the materials, it also impacted the

crystallization kinetics of the material. When compared at the same temperature, increases in ethylene content led to slower isothermal crystallization kinetics as measured by FSC, which is an expected result for random polypropylene-ethylene copolymers.

The changes in structure of the material caused by the introduction of ethylene content led to significant changes in mechanical properties. Tensile elongation increased by an order of magnitude with the addition of 4.9% Et; however, tensile strength decreased by 25%. There is a balance of these two mechanical properties, and the results reported here suggest that ethylene content can be added to tune mechanical properties to the desired elongation at break. This result is promising for the creation of PBF materials with high elongation at break.

Though increasing ethylene content caused the expected change in crystallization kinetics, the shift in onset of melting led to significantly lower temperatures at which each material could be printed without melting the material before laser scanning. This led to faster crystallization at these appropriate bed temperatures for the 4.9% Et sample; however, this shift increased the processability of the 2.2% Et sample. The 2.2% Et sample was less likely to warp than both the 4.9% Et sample and the homopolymer due to its much larger $t_{1/2}$ at the processing bed temperature (Table 5.5).

Tuning crystallization kinetics of PBF materials to increase processability is a difficult goal to realize. This work acts as a demonstration of tuning crystallization kinetics in one specific material class, and shows that changes to a material that impact crystallization kinetics can also impact the crystalline morphology of the material. This work is also limited to exploring samples with ethylene contents of 2.2 and 4.9%. It is possible that the greater processability achieved with 2.2% Et could be balanced with a lower decrease in tensile strength at a lower % Et. Future work should include analysis of polypropylene-ethylene copolymers with even lower ethylene contents.

5.6 References

[1] A. Das, J.S. Bryant, C.B. Williams, M.J. Bortner, Melt-Based Additive Manufacturing of Polyolefins Using Material Extrusion and Powder Bed Fusion, Polym. Rev. (2023) 1–66. https://doi.org/10.1080/15583724.2023.2220024.

[2] L. Fiedler, L.O.G. Correa, M.L.U. Halle-Wittenberg, Evaluation of Polypropylene Powder Grades in Consideration of the Laser Sintering Processabiliy, Z. Kunststofftechnik. (2007) 15.

[3] T. Reinhardt, A. Martha, G. Witt, P. Köhler, Preprocess-Optimization for Polypropylene Laser Sintered Parts, Comput.-Aided Des. Appl. 11 (2014) 49–61. https://doi.org/10.1080/16864360.2013.834138.

[4] I. Flores Ituarte, O. Wiikinkoski, A. Jansson, Additive Manufacturing of Polypropylene: A Screening Design of Experiment Using Laser-Based Powder Bed Fusion, Polymers. 10 (2018) 1293. https://doi.org/10.3390/polym10121293.

[5] W. Zhu, C. Yan, Y. Shi, S. Wen, C. Han, C. Cai, J. Liu, Y. Shi, Study on the selective laser sintering of a low-isotacticity polypropylene powder, Rapid Prototyp. J. 22 (2016) 621–629. https://doi.org/10.1108/RPJ-02-2015-0014.

[6] A. Wegner, T. Ünlü, Powder Life Cycle Analyses for a New Polypropylene Laser Sintering Material, in: Proc. 27th Annu. Int. Solid Free. Fabr. Symp. – Addit. Manuf. Conf., Austin, Texas, 2016: pp. 834–846.

[7] K. Wudy, D. Drummer, Aging effects of polyamide 12 in selective laser sintering: Molecular weight distribution and thermal properties, Addit. Manuf. 25 (2019) 1–9. https://doi.org/10.1016/j.addma.2018.11.007.

[8] F.M. Mwania, M. Maringa, J.G. van der Walt, Investigating the Recyclability of Laser PP CP 75 Polypropylene Powder in Laser Powder Bed Fusion (L-PBF), Polymers. 14 (2022) 1011. https://doi.org/10.3390/polym14051011.

[9] J.-P. Kruth, G. Levy, F. Klocke, T.H.C. Childs, Consolidation phenomena in laser and powder-bed based layered manufacturing, CIRP Ann. 56 (2007) 730–759. https://doi.org/10.1016/j.cirp.2007.10.004.

[10] D. Drummer, D. Rietzel, F. Kühnlein, Development of a characterization approach for the sintering behavior of new thermoplastics for selective laser sintering, Phys. Procedia. 5 (2010) 533–542. https://doi.org/10.1016/j.phpro.2010.08.081.

[11] C.A. Chatham, T.E. Long, C.B. Williams, A review of the process physics and material screening methods for polymer powder bed fusion additive manufacturing, Prog. Polym. Sci. 93 (2019) 68–95. https://doi.org/10.1016/j.progpolymsci.2019.03.003.

[12] D. Drummer, S. Greiner, M. Zhao, K. Wudy, A novel approach for understanding laser sintering of polymers, Addit. Manuf. 27 (2019) 379–388. https://doi.org/10.1016/j.addma.2019.03.012.

[13] A. Amado, K. Wegener, M. Schmid, G. Levy, Characterization and modeling of non-isothermal crystallization of Polyamide 12 and co-Polypropylene during the SLS process, (n.d.) 10.

[14] F. Neugebauer, V. Ploshikhin, J. Ambrosy, G. Witt, Isothermal and non-isothermal crystallization kinetics of polyamide 12 used in laser sintering, J. Therm. Anal. Calorim. 124 (2016) 925–933.

[15] F. Paolucci, M.J.H. van Mook, L.E. Govaert, G.W.M. Peters, Influence of post-condensation on the crystallization kinetics of PA12: From virgin to reused powder, Polymer. 175 (2019) 161–170. https://doi.org/10.1016/j.polymer.2019.05.009.

[16] F. Paolucci, D. Baeten, P.C. Roozemond, B. Goderis, G.W.M. Peters, Quantification of isothermal crystallization of polyamide 12: Modelling of crystallization kinetics and phase composition, Polymer. 155 (2018) 187–198. https://doi.org/10.1016/j.polymer.2018.09.037.

[17] N. Yi, R. Davies, A. Chaplin, O. Ghita, Novel Backbone Modified Poly(Ether Ether Ketone) (PEEK) Grades for Powder Bed Fusion with Enhanced Elongation at Break, Addit. Manuf. (2022) 102857. https://doi.org/10.1016/j.addma.2022.102857.

[18] M. Zhao, K. Wudy, D. Drummer, Crystallization Kinetics of Polyamide 12 during Selective Laser Sintering, Polymers. 10 (2018) 168. https://doi.org/10.3390/polym10020168.

[19] P. Chen, H. Cai, Z. Li, M. Li, H. Wu, J. Su, S. Wen, Y. Zhou, J. Liu, C. Wang, C. Yan, Y. Shi, Crystallization kinetics of polyetheretherketone during high temperature-selective laser sintering, Addit. Manuf. 36 (2020) 101615. https://doi.org/10.1016/j.addma.2020.101615.

[20] N. Bachhar, A. Gudadhe, A. Kumar, P. Andrade, G. Kumaraswamy, 3D printing of semicrystalline polypropylene: towards eliminating warpage of printed objects, Bull. Mater. Sci. 43 (2020) 1–8. https://doi.org/10.1007/s12034-020-02097-4.

[21] Y. Feng, J.N. Hay, The characterisation of random propylene–ethylene copolymer, Polymer. 39 (1998) 6589–6596. https://doi.org/10.1016/S0032-3861(97)10171-9.

[22] M. Gahleitner, P. Jääskeläinen, E. Ratajski, C. Paulik, J. Reussner, J. Wolfschwenger, W. Neißl, Propylene-ethylene random copolymers: Comonomer effects on crystallinity and application properties: PP-Ethylene Random Copolymers, J. Appl. Polym. Sci. 95 (2005) 1073–1081. https://doi.org/10.1002/app.21308.

[23] K. Jeon, Y.L. Chiari, R.G. Alamo, Maximum Rate of Crystallization and Morphology of Random Propylene Ethylene Copolymers as a Function of Comonomer Content up to 21 mol %, Macromolecules. 41 (2008) 95–108. https://doi.org/10.1021/ma070757b.

[24] L.J. Tan, W. Zhu, K. Sagar, K. Zhou, Comparative study on the selective laser sintering of polypropylene homopolymer and copolymer: processability, crystallization kinetics, crystal phases and mechanical properties, Addit. Manuf. 37 (2021) 101610. https://doi.org/10.1016/j.addma.2020.101610.

[25] C.A. Chatham, T.E. Long, C.B. Williams, Powder bed fusion of poly(phenylene sulfide) at bed temperatures significantly below melting, Addit. Manuf. 28 (2019) 506–516. https://doi.org/10.1016/j.addma.2019.05.025.

[26] C.A. Chatham, M.J. Bortner, B.N. Johnson, T.E. Long, C.B. Williams, Predicting mechanical property plateau in laser polymer powder bed fusion additive manufacturing via the critical coalescence ratio, Mater. Des. 201 (2021) 109474. https://doi.org/10.1016/j.matdes.2021.109474.

[27] D. Soldner, S. Greiner, C. Burkhardt, D. Drummer, P. Steinmann, J. Mergheim, Numerical and experimental investigation of the isothermal assumption in selective laser sintering of PA12, Addit. Manuf. 37 (2021) 101676. https://doi.org/10.1016/j.addma.2020.101676.

[28] S. Bruckner, S.V. Meille, I. Vittoriopetraccone, POLYMORPHISM IN ISOTACTIC POLYPROPYLENE, (n.d.).

[29] A. Turner-Jones, Development of the y-crystalform in random copolymers of propylene and their analysis by DSCand x-ray methods, (n.d.).

Chapter 6: Emulation of polymer powder bed fusion using fast scanning calorimetry

Coauthors: Michelle Pomatto, Yifeng Lin

6.1 Abstract:

Understanding crystallization as it occurs during powder bed fusion has long been a goal. Since crystallization directly informs whether warpage occurs during the printing process and the final part properties, understanding this aspect of PBF would yield a robust understanding of the process. The overall goal of this work is to emulate a powder bed fusion (PBF) build to assess how each layer in the build crystallizes during the printing process. The method of emulation is conducted in three steps: 1. *in situ* thermal measurements of layer scanning are conducted, 2. thermal measurements are used to inform a thermal model to simulate layer temperatures after measurement is not possible, 3. thermal model temperature profiles are used in FSC to directly measure the sample. Previous approaches relied on crystallization models to determine crystallinity, but here, crystallization is directly measured in an emulation of the printing process using FSC.

6.2. Introduction

Powder bed fusion (PBF) is a powerful additive manufacturing technique but is almost always limited to process-property relationship development. Recent progress in research has helped add structural analysis to elucidate process-structure-property relationships, but understanding how that structure develops has been difficult to assess. The goal of this work is to emulate a powder bed fusion (PBF) build to assess how each layer in the build crystallizes during the printing process. This emulation would help determine both the extent of crystallization in a layer while subsequent layers are still being scanned (melt enthalpy) and characterize the crystallinity that has

forms (melting endotherm shape). The emulation uses *in situ* thermal measurements of the PBF process as input into a 1D thermal model to establish each layer's thermal history. Each layer's modeled temperatures are then used as input to establish a process-relevant characterization schema for fast scanning calorimetry, in which the evolution of a printed layer's crystallinity is measured.

6.2.1 Crystallization during powder bed fusion

Layer warpage, which can lead to print failure in polymer powder bed fusion (PBF) during recoating, is directly caused by shrinkage due to crystallization [1–4]. Mechanical properties also depend on crystallization and the development of crystallinity during PBF [4,5]. Thus, understanding crystallization during the polymer powder bed fusion (PBF) process is critical as it yields insight into both processing behavior and ultimate properties of printed parts. Ultimately, the goals for understanding crystallization during the PBF process are:

1. To understand exactly how a polymer crystallizes and shrinks during the printing process, which would enable complete understanding of how warpage occurs during the printing process, and
2. To understand how crystallinity develops during the printing process, which determines a part's mechanical properties [6].

With this understanding, the printing process and ultimate part properties could be accurately predicted and optimized [7].

Previously established assumptions that crystallization only occurs during the cooling stage of the PBF printing process is becoming more commonly accepted as false. Researchers have now shown on multiple occasions that crystallization occurs throughout the printing process, and not only

during the cool down stage of printing [8,9]. For example, Drummer et al. observed solidification of material within millimeters below the print surface. These results necessitate further observation and characterization of exactly how solidification occurs during PBF [9]. Assumptions of crystallization only during the cooling stage of printing have also been assumed in PBF modeling literature. Some previous research in this area only begins simulating crystallization once a material reaches the bed temperature, and neglects any crystallization that occurs above bed temperature [2,6]. Neglecting this crystallization can lead to inaccuracies, especially for materials that show rapid crystallization.

One limitation when trying to understand crystallization during PBF processing is that material temperature is very difficult to directly measure following powder recoating where the polymer melt if covered with fresh powder [5]. Some work towards understanding the temperature of parts throughout a PBF build has been conducted using machine setups with extensive embedded thermocouples to measure temperatures during printing [8,10,11]. In-situ IR-thermography is a common method for measuring surface temperature during the printing process, and this method is more adaptable to a commercial system than implementing thermocouples; however, it can only measure the temperature of the top surface of the build piston [10]. Another approach towards thermal modeling of PBF is to use an energy balance approach to predict the temperature of a scanned layer at a specific time; however, this approach makes assumptions of perfect energy absorption by the polymer powder and do not consider coalescence and rheology of a material, which can lead to inaccuracies compared to experimental data [4]. Employing thermal models to predict layer temperature is one other method for attaining thermal data of the PBF process.

6.2.2 Using the Nakamura model to model crystallization during PBF

Modeling of crystallization during PBF processing often uses direct measurements of temperature in combination with the Nakamura crystallization model to predict the development of crystallinity [4,8,12]. This model is the most used non-isothermal crystallization kinetics model in PBF research [3–5,8,13,14]. When using the Nakamura model for non-isothermal measurements at constant cooling rates for PBF, Zhao et al. observed errors on the order of ±10% for their modeling of polyamide 12 [5].

Models rely on the accuracy of the data used to create them. Isothermal crystallization data can be difficult to obtain at temperatures significantly below melting, especially when using a standard DSC, which has limited cooling rates [3]. When there are errors in the data, or data needs to be extrapolated, the chance for large errors in the modeled results is high [15]. Often, researchers adapt the Nakamura model to better match their data. In modeling PBF, adaptations to the Nakamura model that incorporate re-melting during the printing process have also been introduced [8,16]. For polypropylene-ethylene polymers, which are studied in this chapter, adaptations to account for primary and secondary crystallization in these materials have been made for standard non-isothermal crystallization [17]. Though a powerful tool, the Nakamura model has some limitations in its accuracy, only predicts a relative amount of crystallinity and does not inherently account for more complicated crystallization and melting during a process. Direct measurements of a material using a measurement-- such as fast scanning calorimetry (FSC)— would mitigate each of these limitations of the Nakamura model.

6.2.3 Fast scanning calorimetry as an analysis tool for additive manufacturing

Fast scanning calorimetry (FSC) is an experimental technique that enables rapid heating (40,000 K/s) and cooling (4,000 K/s) rates of samples. These cooling rates help collect accurate isothermal crystallization data, especially at temperatures far below melting (i.e., high degrees of

supercooling). Though FSC is becoming a more important tool in PBF research, its application has still been somewhat limited. Paolucci et al. used FSC to quantify isothermal crystallization kinetics for PBF-grade polyamide powders [18,19]. However, this research was a more traditional use of FSC, in which isothermal crystallization data was collected. Other researchers have used FSC in combination with a laser to heat the polymer sample to measure heating and cooling rates in a setup that mimics the PBF process [20–22].

FSC has also been used to study semicrystalline polymers in other AM processes. Comelli et al. used a thermal model to predict layer temperature in material extrusion (MEX) of PEEK and used the resultant data to simulate crystallization during MEX using a FSC, which gave the researchers insight into crystallization throughout the entire printing process [23]. Quick et al. employed FSC to mimic cooling behavior found in metal PBF and determine heat capacities during processing [24].

6.2.4 Contribution

This work details a method for emulating the PBF process to directly observe crystallization during PBF on a layer-by-layer basis. Previous approaches relied on crystallization models to determine crystallinity, but here, crystallization is directly measured in an emulation of the printing process using FSC. The method of emulation is conducted in three steps: 1. *in situ* thermal measurements of layer scanning are conducted, 2. thermal measurements are used to inform a thermal model to simulate layer temperatures after measurement is not possible, 3. thermal model temperature profiles are used in FSC to directly measure the sample. The steps of the method for emulation are displayed in Figure 6.32.

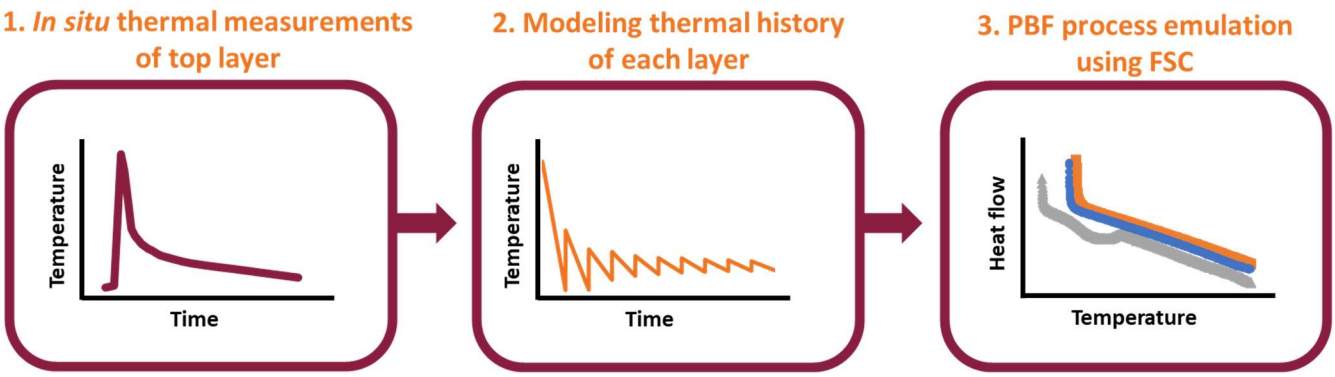

Figure 6.32 the three-step process for emulation of the PBF process. Step 3 yields direct measurements of any crystallinity that forms within the printed layer.

Direct measurement of the material in FSC and using temperature profiles directly informed from process measurements should yield a more accurate measurement of crystallization during the printing process. Further, FSC measurements inherently incorporate any impacts to non-isothermal crystallization that would have to be included within a crystallization model. Measurements of crystallinity by FSC provide a full melting endotherm for the measured material, which helps describe the thickness of the crystalline lamella as well as the amount of crystallinity. Crystallization models only determine relative amount of crystallinity. Understanding the crystallinity of each layer at any point during a build can help understand process failure modes, such as warpage, and create feedback that could inform different processing approaches to mitigate print failure. The benefits of a direct measurement of a material using FSC are discussed in this work and an emulation of a 10-layer build that utilizes in-situ thermal measurements, thermal modeling, and FSC to evaluate crystallization during the PBF process is demonstrated.

6.3. Materials and methods

6.3.1 Material system

The polymer powder used for this research was a polypropylene-ethylene copolymer powder supplied by Braskem North America. This material was a random copolymer with an ethylene

content of 4.9%. This material acted as an example material for the methodology described within this work. The emulation method is material agnostic and can be applied to any material system.

6.3.2 Experimental setup for PBF emulation

6.3.2.1 Powder bed fusion system

All PBF printing was conducted using a Prodways Promaker P2000 HT manufactured by Farsoon. This printer is equipped with a 60 W, CO_2 laser. The sample used for thermal data collection was printed with the following printing parameters: T_{bed} = 103° C, 25 W, 1725 mm/s, 0.254 mm hatch spacing, 100 μm layer height, and 20 s layer time. These parameters had previously been determined to lead to successful printing of the material tested in this research and are therefore representative of realistic processing parameters. The sample printed for thermal measurements was a 20 x 20 x 20 mm cube, which was taken to be large enough to be representative of powder bed fusion parts. A full-scale tensile bar (3 mm thickness) was printed using these parameters and measured using standard DSC to assess its crystallinity for comparison to samples simulated in FSC.

6.3.2.2 *In situ* IR-thermography

In-situ thermal measurements were taken during the printing process via an infrared camera (Micro Epsilon TIM 640) mounted in the PBF system to view the build area. In-situ temperature measurements were taken during and after laser scanning of each layer. Within each scanned area, the maximum temperature was measured and reported as the layer temperature.

Each layer's temperature was measured beginning with powder spreading across the layer and ending with powder spreading of the subsequent layer. The peak temperature during scanning, and minimum temperature after scanning, were of particular interest for the thermal modeling detailed

in Section 2.2.3. Previous researchers have used similar geometries and sizes for IR thermography of PBF [8]. A total of 10 printed layers were measured, with the goal of simulating a 10-layer build. This layer count has been previously used by other researchers [2]. In-situ thermal measurements were taken for layers 1, 5 & 10. These three layers were emulated using the steps detailed in sections 2.2.3-2.2.5.

6.3.2.3 Thermal model to generate layer temperatures

Due to the limitations of direct temperature measurement of a layer following recoating (described in Section 1.1) a thermal model was used to estimate each layer's temperature over the course of the 10-layer build. The in-situ measurements of maximum layer temperature (Section 2.1.2) were used as the input for a simplified PBF process model. This 1D heat transfer model, which uses a finite difference approach that accounts for conduction and convection, estimates layer temperature throughout the print process. Convection coefficients were determined by testing values to fit the thermal data. Air temperature was directly measured using a thermocouple and was 98° C. It is assumed that each layer has a uniform temperature.

6.3.2.4 Fast scanning calorimetry to emulate PBF

The simulated temperature history of each layer was then used as the temperature cycle in a fast scanning calorimeter (FSC) to directly measure and emulate the printing process and measure crystallinity in each layer of the printed part. A Mettler Toledo Flash DSC 1)with Huber intra cooler TC100 was used for all FSC measurements in this research. This instrument is capable of heating rates up to 40,000 °C/s and cooling rates up to 4000 °C/s. To simplify the FSC scheme used to mimic the temperature profile produced by the thermal model, a single cooling rate determined by the peak and minimum temperature of each layer and a 20 s layer cycle time was calculated. This

simplification has previously been used by other researchers [6]. The mass of the single powder particle used as a sample for FSC was estimated as 6 µg from optical microscopy.

6.3.2.5 Characterization of morphology during simulated build

To assess the crystalline morphology of each layer at different times in the build, samples were heated and melt enthalpy was measured following the emulated 10^{th} layer of the build. These measurements are representative of each layer in the build following printing of the 10^{th} layer. This gives a snapshot of the morphology at three different layers in the build after the 10^{th} layer was printed. For example, the simulated 5^{th} layer would go through six heating and cooling cycles, which represents that layer's scanning and the following five scans for the subsequent layers. Following the sixth heating and cooling cycle the 5^{th} layer experiences, the sample is heated to 200° C at 10000 °C/s to completely melt the material and assess the morphology that developed during the emulation. The melt enthalpy was determined for each emulated layer to understand the amount of crystallinity in that layer after the 10^{th} layer is scanned and the build is completed.

6.4. Results & discussion

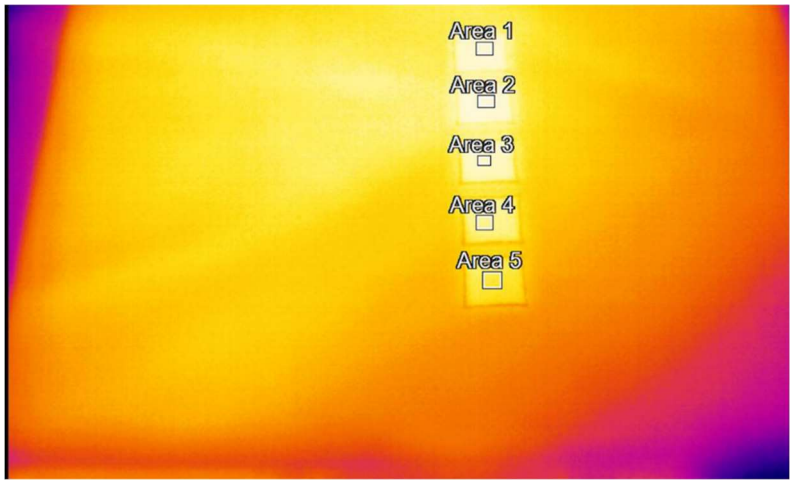

Figure 6.2 image from thermal camera with measurement areas on five scanned layers (20 x 20 mm geometry).

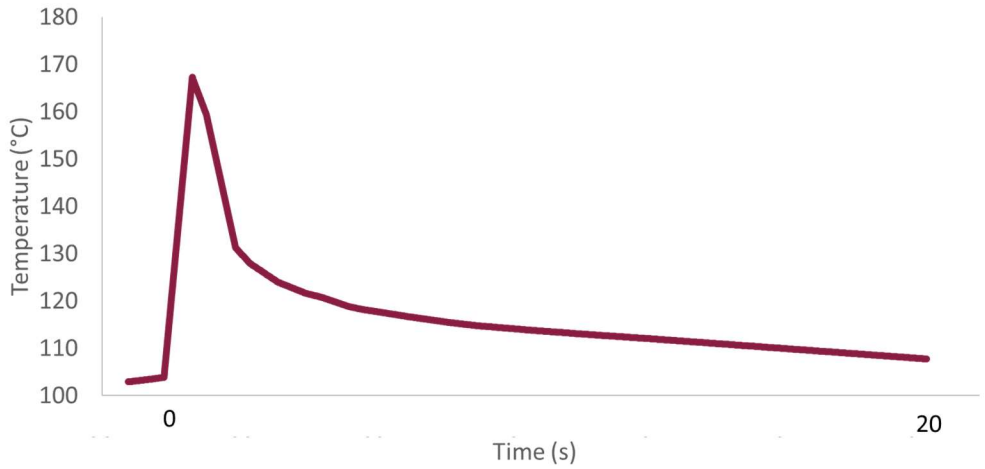

Figure 6.3 Example of temperature data for one layer collected from in-situ IR thermography. This temperature profile is then used as input into the thermal model to predict the thermal history of each layer throughout the build.

Measured layer temperature from *in situ* IR-thermography (Figure 6.3) are synthesized to establish the thermal profile of each single scanned layer (Figure 6.2) throughout the build process. This data yielded the peak temperature, cooling rate and layer temperature at the time of powder recoating.

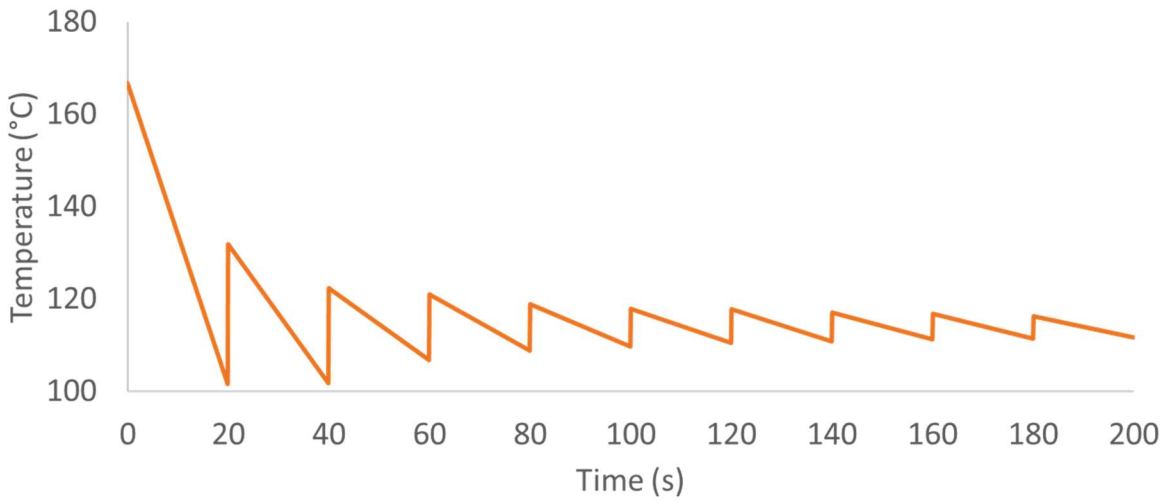

Figure 6.33 the simulated temperatures with single cooling rates, which was used as an input for the FSC measurements. The increase in temperature from subsequent printed layers decreases with time as the layer is more thermally insulated. Each peak occurs during the scanning of a subsequent printed layer. Layer cycle times are 20 s.

This data, collected for 10 layers, was input into a process thermal model to determine each layer's thermal history throughout the build when its surface is no longer measurable by the IR-camera, which occurs during powder recoating. As an example, the simulated temperature history of Layer 1 throughout the complete 10-layer build is shown in Figure 6.33. Cooling rates between layers have been set to a constant value, as described in 2.2.4. The small layer thickness, 100 μm, leads to significant reheating (10s of °C) of the printed layer during scanning of subsequent layers. The increase in temperature from scanning of following layers (which occurs at every 20s, as defined by the layer time process parameter described in Section 2.2.1), diminishes as the layers get farther from the simulated layer.

This modeled temperature is similar to the temperature profile observed by Comelli et al. during their thermal modeling of MEX [23]. Only after cooling from the first scanning does the material approach the set T_{bed} (103° C). After this layer, the predicted temperature is above T_{bed} for the rest of the 10-layer build due to the accumulation of the thermal energy of multiple scans and the

insulating powder bed surrounding the part. This is important for understanding the temperature at which early crystallization could occur within the printed material, since higher temperatures lead to slower crystallization.

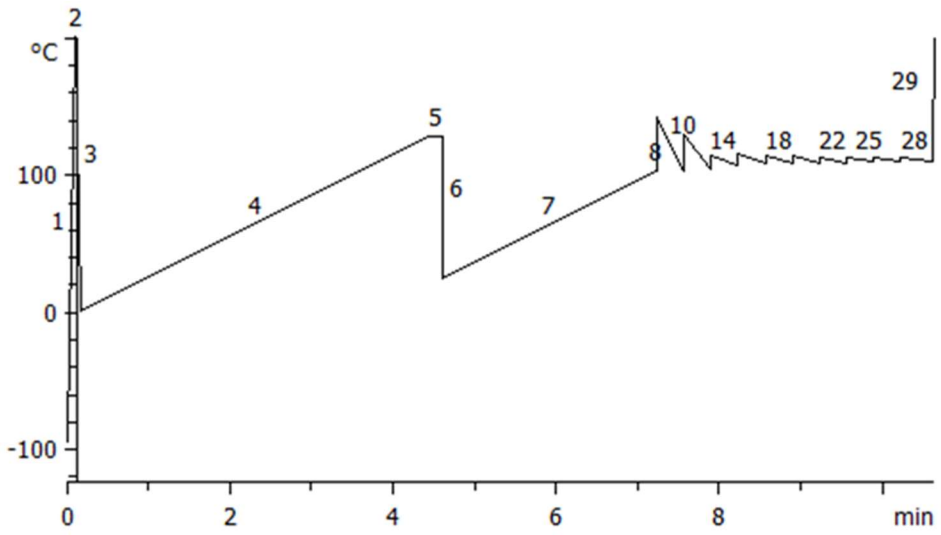

Figure 6.34 the temperature protocol for FSC to simulate Layer 1. Steps 1-7 are incorporated to set the initial structure of the material and to make sure this structure is consistent between tests. Steps 8-28 recreated the heating and cooling was predicted for Layer 1 over the course of the 10-layer build. In step 29, the material is completely melted to measure the melt enthalpy of the material. Step 29 yields the measurement of the morphology of the material during this point in the build.

The temperature protocol for FSC determined by the modeled temperature profile for Layer 1 is displayed in Figure 6.34 (the temperatures and cooling rates for each FSC protocol can be found in **Error! Reference source not found.**). The figure shows the many heating and cooling steps that occur for each layer during the PBF process. Samples are measured from each layer's FSC protocol and the extent of crystallization observed. In this research, crystallinity is only measured following scanning of the 10th layer; however, it is possible to alter the protocol to include a melting step (step 29 in Figure 6.34) at any point, which would enable measurement of a layer's crystallinity at any point in the PBF process.

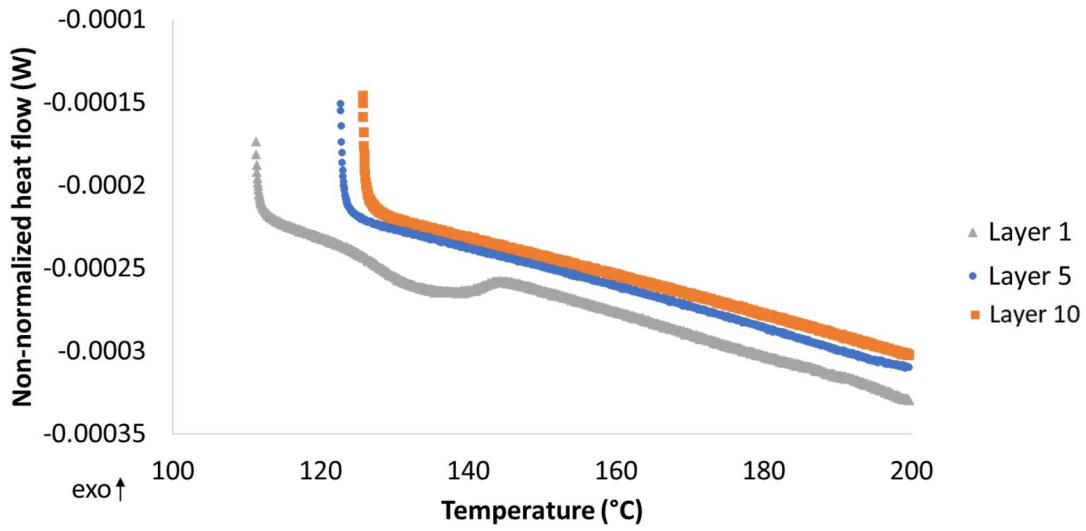

Figure 6.35 differences in heat flow from the baseline signify crystallinity developed in the sample. The area under the curve increases as the printed layer has longer to cool. This leads to Layer 1 showing the highest amount of crystallinity.

The melting endotherms for each simulated layer as measured by FSC are displayed in Figure 6.35. This measurement shows not only the amount of crystallinity within each layer, but the temperatures at which the material would melt at as well. For example, it is observed in Figure 6.35 that, in Layer 1, the melting endotherm begins at 123° C and ends at 142° C. In this way, there is significantly more information available in these curves than would come from use of the Nakamura model, which only yields the amount of crystallinity.

From Figure 6.35 it is observed that the amount of crystallinity in a layer increases as the layer has had longer to cool. Layer 1 (the first layer printed in the 10-layer build) is the only layer which shows any crystallinity at the end of the 10^{th} layer scan. The energy to melt this sample was 75.1 μJ. Normalized for the mass of the sample, the melt enthalpy was 12.5 J/g. The presence of crystallinity in only the first layer agrees with the expectation that layers will be cooler and have greater opportunity to crystallize during PBF processing.

Layer 10 shows no crystallinity following its final scan and recoat. This result is expected because the material has just been heated and cooled before the measurement of its melting endotherm. This allows for only 20 s to crystallize, which is especially challenging given that it is well above T_{bed} (103° C).

Surprisingly, Layer 5 shows no crystallinity at the end of the scanning either. This could be caused by the slower cooling that occurs in the layer since it is surrounded both above and below by other scanned layers, which provide thermal insulation to this layer and reduce its ability to crystallize.

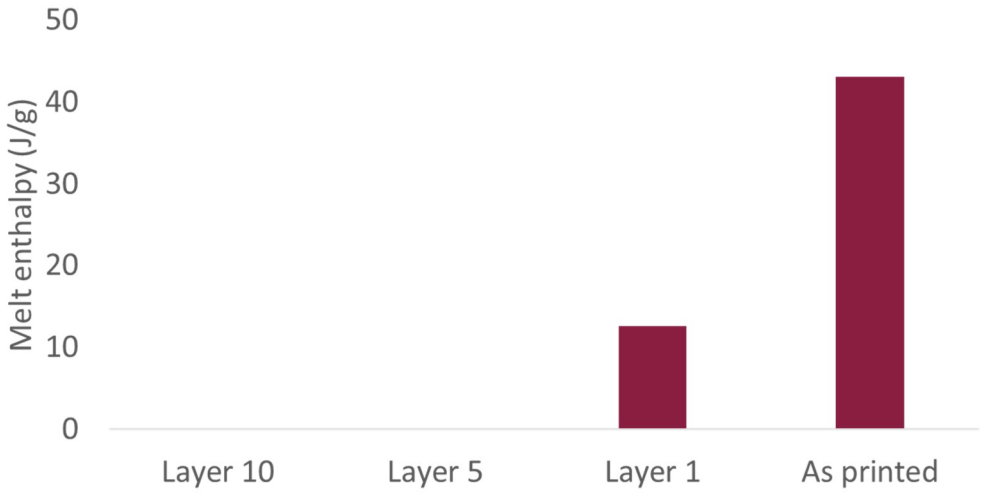

Figure 6.36 though significant crystallinity develops over the 10-layer build in Layer 1, this value is much lower than the ultimate crystallinity observed in the full-scale, printed part.

Layers' melt behavior as measured following printing of the 10th layer are compared to a full-scale, printed part in Figure 6.36. The full-scale part has a melt enthalpy of 42.8 J/g, which is much higher than the simulated layers. This part has had a much greater time at T_{bed} and has been cooled to room temperature which allows it to fully crystallize. Layer 1 having a roughly 30% the crystallinity of the final part demonstrates how quickly crystallization occurs during the printing

of this part even with only 10 layers printed and the Layer 1 spending its entire printing time above T_{bed}.

6.5 Conclusion & future work

A method that enables emulation of the PBF printing process using FSC was successfully demonstrated. In this method, direct temperature measurements of the PBF process were collected and then input into a thermal process model, which generated approximations of the thermal history of each individual layer throughout the build. Finally, the thermal profiles generated from the thermal model were used to create a FSC protocol that emulated a layer's thermal history and enabled measurements of a layer's crystallinity throughout the build process. This method for emulation offers an alternative to crystallization modeling, which is limited to only describing the amount of crystallinity in a sample at a specific time and does not characterize the crystallinity (no melting endotherm). Using FSC enables a more thorough analysis of the crystallization of the polymer during the printing process because it measures the melting endotherm of the polymer, which is determined by the thickness of the crystals in the sample. The shape of the melting endotherm will also demonstrate how crystals grow and thicken throughout the printing process. How these crystals develop will directly determine shrinkage that occurs during the printing process, which can lead to warpage and can affect the mechanical properties of the final part. This technique could be used in tandem with printing observations or a stress model to rigorously understand how warpage occurs during the printing process.

As a direct measurement of a material, FSC also offers the advantage of not needing to make adaptations to crystallization models based on a specific material's behavior. Other researchers have included augmentations to the Nakamura model which include aspects of the crystallization process to incorporate behaviors such as re-melting of a material during printing or materials that

undergo both primary and secondary crystallization [16,17]. The direct measurement of a material in FSC inherently incorporates these effects without needing experiments to understand behavior specific to the material of interest. This makes the process chain described here powerful in its ability to observe crystallization of a simulated print for a new material without any prior knowledge of crystallization behavior in the polymer. This test is rapid and could provide knowledge early in the development process of new materials for PBF.

The results observed in FSC measurements using the modeled temperature profiles further disprove the assumption that crystallization in PBF is isothermal and occurs only during the cooling stage of PBF processing. In the specific polymer system analyzed in this work, crystallization readily occurred while a layer was above T_{bed} during the scanning of subsequent layers ($t_{1/2}$ = 83 s at the chosen T_{bed}). These results demonstrate the necessity of understanding crystallization at temperatures above T_{bed} during PBF. It is necessary to understand all crystallization during the PBF process to fully understand crystallization that determines shrinkage—and therefore warpage—and final part properties.

Increasing the number of rates programmed into the FSC for each cooling step would further increase the accuracy of the FSC emulations of the printing process and enable better understanding of crystallization during the printing process. However, any limitation in the temperature modeling is carried through both the FSC measurement and the crystallization modeling, which keeps the comparison between emulation and modeling consistent. The modeling of crystallization in this work could be improved by working to better understand isothermal crystallization of the material tested in this work; however, because most researchers do not modify the Nakamura model for their work on PBF crystallization, it was seen as appropriate for modeling the material tested here.

6.6 References

[1] C.A. Chatham, T.E. Long, C.B. Williams, A review of the process physics and material screening methods for polymer powder bed fusion additive manufacturing, Prog. Polym. Sci. 93 (2019) 68–95. https://doi.org/10.1016/j.progpolymsci.2019.03.003.

[2] A. Amado, K. Wegener, M. Schmid, G. Levy, Characterization and modeling of non-isothermal crystallization of Polyamide 12 and co-Polypropylene during the SLS process, in: 5th Int. Polym. Moulds Innov. Conf., Ghent, 2012.

[3] F. Neugebauer, V. Ploshikhin, J. Ambrosy, G. Witt, Isothermal and non-isothermal crystallization kinetics of polyamide 12 used in laser sintering, J. Therm. Anal. Calorim. 124 (2016) 925–933.

[4] F. Shen, W. Zhu, K. Zhou, L.-L. Ke, Modeling the temperature, crystallization, and residual stress for selective laser sintering of polymeric powder, Acta Mech. 232 (2021) 3635–3653. https://doi.org/10.1007/s00707-021-03020-6.

[5] M. Zhao, K. Wudy, D. Drummer, Crystallization Kinetics of Polyamide 12 during Selective Laser Sintering, Polymers. 10 (2018) 168. https://doi.org/10.3390/polym10020168.

[6] N. Yi, R. Davies, A. Chaplin, O. Ghita, Novel Backbone Modified Poly(Ether Ether Ketone) (PEEK) Grades for Powder Bed Fusion with Enhanced Elongation at Break, Addit. Manuf. (2022) 102857. https://doi.org/10.1016/j.addma.2022.102857.

[7] C. Balemans, S.F.S.P. Looijmans, G. Grosso, M.A. Hulsen, P.D. Anderson, Numerical analysis of the crystallization kinetics in SLS, Addit. Manuf. 33 (2020) 101126. https://doi.org/10.1016/j.addma.2020.101126.

[8] D. Soldner, S. Greiner, C. Burkhardt, D. Drummer, P. Steinmann, J. Mergheim, Numerical and experimental investigation of the isothermal assumption in selective laser sintering of PA12, Addit. Manuf. 37 (2021) 101676. https://doi.org/10.1016/j.addma.2020.101676.

[9] D. Drummer, S. Greiner, M. Zhao, K. Wudy, A novel approach for understanding laser sintering of polymers, Addit. Manuf. 27 (2019) 379–388. https://doi.org/10.1016/j.addma.2019.03.012.

[10] C. Li, S.E. Snarr, E.R. Denlinger, J.E. Irwin, M.F. Gouge, P. Michaleris, J.J. Beaman, Experimental parameter identification for part-scale thermal modeling of selective laser sintering of PA12, Addit. Manuf. 48 (2021) 102362. https://doi.org/10.1016/j.addma.2021.102362.

[11] S. Josupeit, H.-J. Schmid, Three-dimensional in-process temperature measurement of laser sintered part cakes, in: University of Texas at Austin, 2014.

[12] K. Nakamura, T. Watanabe, K. Katayama, T. Amano, Some aspects of nonisothermal crystallization of polymers. I. Relationship between crystallization temperature, crystallinity, and

cooling conditions, J. Appl. Polym. Sci. 16 (1972) 1077–1091. https://doi.org/10.1002/app.1972.070160503.

[13] A. Amado, M. Schmid, K. Wegener, Simulation of warpage induced by non-isothermal crystallization of co-polypropylene during the SLS process, AIP Conf. Proc. 1664 (2015) 160002. https://doi.org/10.1063/1.4918509.

[14] H.W.B. Teo, K. Chen, V.T. Tran, H. Du, J. Zeng, K. Zhou, Non-isothermal crystallization behaviour of polyamide 12 analogous to multi-jet fusion additive manufacturing process, Polymer. 235 (2021) 124256. https://doi.org/10.1016/j.polymer.2021.124256.

[15] T.W. Chan, A.I. Isayev, Quiescent polymer crystallization: Modelling and measurements, Polym. Eng. Sci. 34 (1994) 461–471. https://doi.org/10.1002/pen.760340602.

[16] D. Soldner, P. Steinmann, J. Mergheim, Modeling crystallization kinetics for selective laser sintering of polyamide 12, GAMM-Mitteilungen. 44 (2021) e202100011. https://doi.org/10.1002/gamm.202100011.

[17] H.J.M. Caelers, A. De Cock, S.F.S.P. Looijmans, R. Kleppinger, E.M. Troisi, M. Van Drongelen, G.W.M. Peters, An experimentally validated model for quiescent multiphase primary and secondary crystallization phenomena in PP with low content of ethylene comonomer, Polymer. 253 (2022) 124901. https://doi.org/10.1016/j.polymer.2022.124901.

[18] F. Paolucci, M.J.H. van Mook, L.E. Govaert, G.W.M. Peters, Influence of post-condensation on the crystallization kinetics of PA12: From virgin to reused powder, Polymer. 175 (2019) 161–170. https://doi.org/10.1016/j.polymer.2019.05.009.

[19] F. Paolucci, D. Baeten, P.C. Roozemond, B. Goderis, G.W.M. Peters, Quantification of isothermal crystallization of polyamide 12: Modelling of crystallization kinetics and phase composition, Polymer. 155 (2018) 187–198. https://doi.org/10.1016/j.polymer.2018.09.037.

[20] L. Lanzl, K. Wudy, M. Drexler, D. Drummer, Laser-high-speed-DSC: Process-oriented Thermal Analysis of PA 12 in Selective Laser Sintering, Phys. Procedia. 83 (2016) 981–990. https://doi.org/10.1016/j.phpro.2016.08.103.

[21] K. Wudy, M. Drexler, L. Lanzl, D. Drummer, Analysis of time dependent thermal properties for high rates in selective laser sintering, Rapid Prototyp. J. 24 (2018) 894–900. https://doi.org/10.1108/RPJ-01-2017-0013.

[22] T. Laumer, K. Wudy, M. Drexler, P. Amend, S. Roth, D. Drummer, M. Schmidt, Fundamental investigation of laser beam melting of polymers for additive manufacture, J. Laser Appl. 26 (2014) 042003. https://doi.org/10.2351/1.4892848.

[23] C.A. Comelli, N. Yi, R. Davies, H. Van Der Pol, O. Ghita, Material extrusion thermal model mapped across polyetheretherketone isothermal and continuous cooling transformation charts, Addit. Manuf. 59 (2022) 103129. https://doi.org/10.1016/j.addma.2022.103129.

[24] C.R. Quick, P. Dumitraschkewitz, J.E.K. Schawe, S. Pogatscher, Fast differential scanning calorimetry to mimic additive manufacturing processing: specific heat capacity analysis

of aluminium alloys, J. Therm. Anal. Calorim. 148 (2023) 651–662. https://doi.org/10.1007/s10973-022-11824-4.

6.7 Supplementary Information

Layer 1

Layer #	Maximum temperature (°C)	Minimum temperature (°C)	Cooling rate (°C/s)
1	166.70	101.30	3.27
2	131.85	101.67	1.51
3	122.33	106.79	0.78
4	120.99	108.72	0.61
5	118.87	109.75	0.46
6	117.87	110.38	0.37
7	117.79	110.80	0.35
8	117.06	111.23	0.29
9	116.80	111.46	0.27
10	116.26	111.60	0.23

Layer 5

Layer #	Maximum temperature (°C)	Minimum temperature (°C)	Cooling rate (°C/s)
5	182.06	111.64	3.52
6	144.93	112	1.65
7	134.92	118.16	0.84
8	134.24	120.95	0.66
9	133	122.36	0.53
10	131.7	123.18	0.43

Layer 10

Layer #	Maximum temperature (°C)	Minimum temperature (°C)	Cooling rate (°C/s)
10	192.70	126.10	3.33

6.S1 details the maximum temperatures, minimum temperatures and cooling rates used for the emulations of layers 1, 5 and 10. These values were directly input into the FSC, with 20 s of cooling at the specified rate between the maximum and minimum temperature.

7. Summary, Contributions & Future Work

7.1 Summary

The primary goal of this dissertation is to expand the understanding of laser-based polymer powder bed fusion by studying the processing of polyolefins. These materials offer the challenge of having faster crystallization kinetics than the polyamides that are commonly processed in PBF and are therefore more challenging to process. Ultra-high molecular weight polyethylene (UHMWPE) offers the additional challenge of having an especially high melt viscosity, which, when analyzed from a standard PBF viewpoint, should not be processable using this AM method. As synthesized in Chapter 2, polyolefins are challenging to process via AM due to their rapid crystallization, which makes warpage during PBF much more likely.

Chapters 3 and 4 present work towards the goal of manufacturing fully dense parts from UHMWPE. In Chapter 3, a method for PBF-processing UHWMPE is developed which enables complex geometries to be printed. This was accomplished by leveraging melt explosion, which occurs in nascent, as synthesized, UHMWPE powder when it is first molten. Melt explosion was controlled by partially melting the scanned area using large hatch spacings, which printed each part with an internal lattice that held the entrapped loose powder in place. Then, the high melt viscosity of UHMWPE was leveraged to coalesce the printed green part together into a handleable part. This could only be accomplished because of the high viscosity of the molten material held its shape within the melt. By leveraging these two unique behaviors, complex geometry parts were successfully printed

In Chapter 4, additional post-processing methods were explored to further densify printed UHWMPE parts. Specifically, pressure was induced in multiple post-processing steps to densify

the printed parts and increase the density of printed samples to that of the bulk polymer. Part structure and performance was characterized for multiple post-processing treatments and it was found that a combination of cold isostatic pressing (CIP) to densify the printed part and then hot isostatic pressing (HIP) to further densify the part in the melt, yielded fully dense parts, with similar performance to the same grade of UHMWPE when it is compression molded (slightly lower tensile strength, equivalent elongation at break).

In Chapter 5, the author investigated how changes in polymer structure influence the processing and properties of a polymer in PBF. Polypropylene-ethylene (PP-PE) random copolymers were used as a demonstration material, as increases in ethylene content (0-4.9%) significantly decrease the crystallization kinetics of the polymer. It was hypothesized that this would increase the processability (e.g., less likely to experience warpage that disrupts printing) of the material; however, increases in ethylene content led to broadening of the melting endotherm and a lower onset of melting for the material. The decrease in the onset of melting from increases in ethylene content reduced the bed temperature that could be used for printing without melting the material, which ultimately, made the material with the highest ethylene content crystallize faster at a usable bed temperature. However, the intermediate ethylene content sample was more processable than both the highest ethylene content sample and the homopolymer, which suggests a balance of crystallization kinetics and melting endotherm shifting was achieved. This work also characterized the general impact of ethylene content on printed part performance and found that, as crystallinity decreased with increasing ethylene content, there was both an increase in elongation at break and a decrease in tensile strength. The results show that the crystallinity can be tuned by the inclusion of ethylene content and these two mechanical properties can be adjusted.

In Chapter 6, a methodology for emulating the PBF process using fast scanning calorimetry (FSC) was developed and demonstrated. This methodology employs FSC to emulate the temperatures a specific layer in a PBF build experiences over the length of the build to characterize the layer's crystallinity at a given point in the process. This methodology had three steps:

1. Each layer's temperature is recorded during printing using in-situ IR thermography.
2. Thermal history of each layer is simulated using a thermal model informed by the in-situ temperature measurements.
3. These temperature history profiles can then be input into FSC to emulate the build for each specific layer and understand how crystallinity develops in a layer during a build.

This methodology builds on crystallization modeling that is common in PBF by collecting crystallization data directly from a crystallizing polymer, which circumvents any adjustments to a crystallization model necessary for a specific material. This methodology also showed not only the amount of crystallinity in the sample at a specific time, but how the crystallinity is distributed. The full melting endotherm is measured in this method; this information gives significantly more insight into the crystallinity of a material than the absolute crystallinity reported by crystallization models.

7.2 Scientific contributions

Listed below are the scientific contributions that were accomplished within this work to push forward the study of laser-based polymer powder bed fusion.

7.2 Key contributions:

- Leveraged fundamental polymer phenomenon to enable printing of a material that is expected to not be printable due to its high viscosity

- Developed understanding of the complex interplay between crystallization kinetics, material structure and how these properties impact processing in PBF
- Provided an alternative to crystallization modeling for assessing the development of crystallinity in each layer during PBF

7.3 Major contributions:

- Developed a process-chain which enabled PBF of UHMWPE
    - First reported PBF printing of complex, multi-layered UHWMPE parts.
    - Process-chain led to successful printing of a material that should be too viscous to process in powder bed fusion
    - Connected empirically observed expansion with fundamental polymer behavior to develop a novel processing strategy
    - Leveraged the high melt viscosity of UHMWPE to enable post-processing in the melt while maintaining shape
    - First demonstration of polymer PBF which melts material during post-processing to densify the part and set part properties
    - Achieved successful processing by exploring non-traditional process parameter combinations using low T_{bed} and high hatch spacing
- Post-processed PBF printed UHMWPE to a fully dense part with high performance
    - Creation of a novel post-process flow that leverages pressure induced densification.
    - Leveraged the high melt viscosity of UHMWPE to enable post-processing in the melt while maintaining shape
    - First demonstration of achieving fully dense UHWMPE parts printed via PBF (or any other AM process)

    - Developed an understanding of how pressure affects densification and mechanical performance at each step of post-processing treatments
- Processed and characterized printed parts of PP-PE copolymers with ethylene contents ranging from 0-4.9%
    - Determined balance of mechanical properties between tensile strength and elongation at break for PP-PE copolymers
- Built understanding of impact of ethylene content on the processing of PP-PE copolymers in PBF
    - Crystallization kinetics decrease with increasing ethylene content, but melting endotherm also shifts to lower temperatures, which limits the usable bed temperature for printing for high ethylene content samples
    - This combination of changes in behavior leads to usable bed temperatures where crystallization is faster for the samples with high ethylene which results in this sample to be more difficult to process in PBF and more likely to warp during processing, however lower ethylene contents led to a more processable material
    - Changes in ethylene content that lower crystallization kinetics also impact the morphology of a material, which can diminish processability without warpage at high enough ethylene contents
- Developed process-chain which enabled emulation of the PBF process for each specific layer using FSC
    - Emulated a 10-layer PBF build using FSC

- Unlike existing PBF modeling literature, this method of emulation yields the entire melting endotherm of a emulated layer at any point during a PBF build, rather than only an amount of crystallinity
- Direct measurement of the polymer, which yields a melting endotherm can be used to understand the exact type of crystallinity developed during the printing process and how that crystallinity develops during the build

7.4 Limitations of presented work

All printing of UHMWPE was conducted on highly sieved "fines" collected from the UHMWPE production process. This yielded a specific particle size distribution that was found to work for the sets of processing parameters discussed in this dissertation. The adjustments for using larger particle sizes or particle size distributions and how this might cause interplay between the laser diameter and the printing process has not been investigated. The printing process established in Chapter 3 has the majority of the scanned area of each part made up by non-intersecting scanlines. It is possible that the way in which melting occurs from the single scanline could be dependent on particle size and adjustments would have to be made for a different particle size distribution.

The UHMWPE studied in Chapters 3 and 4 is a 3000 kDal polyethylene. This is on the lowest end of what is considered UHMWPE and there are many UHMWPE grades with significantly higher molecular weights (up to 10000 kDal for some grades). Melt explosion should occur in any of these UHMWPE depending on the extent of co-crystallization in the material during synthesis, however, the amount of expansion will depend on the molecular weight. Increases in molecular weight should yield an even greater difference between the solution crystallized, nascent powder's radius of gyration R_g and the R_g of the melt for that grade of UHMWPE. This could cause challenges in achieving the partial melt and expansion necessary to enable printing without too

much expansion and tuning of the printing parameters to the specific grade of UHMWPE would be necessary.

The size of the samples investigated in chapter 4 are very small compared to common PBF materials or even possible applications for printed UHMWPE such as parts in knee and hip replacements or bearings. Though densification was achievable in these parts, it cannot be assumed that densification is generalizable to parts of any size. Further experiments would be necessary to understand the limitations of this post-processing approach and determine design for additive manufacturing (DFAM) guidelines for this methodology.

In the chapter 5 work on tuning crystallization kinetics with increases in ethylene content, the minimum amount of ethylene content was 2.2%. Though this value positively impacted processing, it is possible that lower ethylene contents could improve processing further and minimize loss of tensile strength. This work sets a window in which processing difficulties occur, however conclusions about lower ethylene contents have not been made. It is possible that at lower ethylene contents there is a balance of slower crystallization kinetics and smaller changes to the melting endotherm in the PP-PE copolymer and increase mechanical properties.

Though the methodology established in chapter 6 was carried out and showed observations of crystallization in a simulated build, this method is very time-intensive. Collecting and analyzing thermal data for PBF is non-trivial with the current setup and for future work collecting data for different sets of process parameters, this work is multiplied. Thermal modeling is not time intensive but conducting experiments using FSC can be very tedious. Ultimately, to get more accurate results many cooling rates must be used in each layer to mimic the cooling curve observed in the printed and programming this type of scheme is taxing. FSC does not yield measurements of the crystallinity at each time-step, it instead needs to have a final heating step to measure the

melting endotherm. This means if the crystallinity for a layer is desired during each printing cycle, the same number of runs of the FSC must be conducted, which is programming intensive and can take significant time.

7.5 Future Work and Final Reflections

Connecting polymer science to PBF is still a burgeoning field. The push away from researching process-property relationships to fully understanding process-structure-property relationships in PBF enables true understanding of the completer PBF process. This dissertation worked to build the connections between polymer science and PBF processing through demonstrations using polyolefin materials.

Melt explosion during PBF of UHMWPE is observed but not directly characterized in the work of Chapter 3. Work towards using in situ small-angle x-ray scattering (SAXS) or small-angle neutron scattering (SANS) is essential to completely understand what occurs on a polymer chain level during the laser scanning process which causes expansion. Previous studies have observed melt explosion through melting films and compression molding, but not in such a very non-isothermal process like PBF. The interaction between the rapid heating of UHMWPE during PBF and the melting and expansion that occurs could further the understanding of how this phenomenon occurs and its implications in the PBF process.

The key properties which make UHMWPE such an important material for applications are its wear properties. These properties have yet to be explored for the process-chain established in chapters 3 and 4. It is paramount to characterize these properties and begin to optimize post-processing around wear properties. Achieving fully dense parts was a key goal to maximizing wear properties, however, wear characterization is necessary to fully assess the printed parts.

One large area of future work is to take the demonstrations of printability from Chapters 3 and 4 and apply the results to polytretrafluoroethylene (PTFE). PTFE is the most similar thermoplastic to UHMWPE in that it is incredibly viscous, and its highly crystalline nature could yield an expansion during melting in a PBF system. The combination of these two similarities suggests that the methodology determined in this dissertation may yield a processing route for PTFE additive manufacturing, which is still a large goal within the field. PTFE has the potential to open up PBF printed materials to many applications for which no current material is suited. Future researchers should take caution, as degrading fluoropolymers can be quite hazardous.

Though the impact of changes in chemical structure, which changed the crystallization kinetics of different samples was explored, there are still not guidelines established for the type of crystallization kinetics that are necessary for successful PBF of a material. This is a key goal in PBF research and could enable testing of small quantities of an experimental powder in a DSC or FSC to predict printability. Defining and understanding the bounds of crystallization kinetics (if they exist) for PBF materials is paramount to efficiently adding materials to the PBF printing portfolio. This work supports the established behavior in PBF that polymers with slower crystallization rates are more processable but doesn't fully push that metric to define boundaries for printability. This is an essential goal for future work in PBF.

The methodology established in Chapter 6 was limited to one evaluation of one 10-layer build for a specific set of processing parameters and specific polymer. In future work it is essential to expand the simulations and begin to connect the conclusions from FSC to processing behavior. This could include connecting the rate of crystallinity development in an FSC to warpage observed during printing to understanding differences in crystallinity between different printed parts and connecting these differences to the development of crystallinity in an FSC simulation.

Establishing rheological requirements for PBF is an area that must be fully investigated. The status of rheology in PBF is to say that coalescence requires surface tension to overcome the zero-shear viscosity of a material. This understanding is limited and polymer systems have yet to be pushed to understand how different polymers for PBF can be different from the polymers developed for traditional thermoplastic processes such as injection molding or extrusion, which apply high shear and are reliant on viscosities much different from the zero-shear viscosity.

PBF is an exceptionally unique polymer process. It includes rapid heating and cooling, no shear, and each layer in a part has its own, unique thermal history. The amount of powder needed for part-scale experiments is large enough to prove daunting to many chemists and the particle size requirements are stringent. The advancement of PBF research depends on the ability to characterize materials using small scale experiments to determine printability. FSC, modeling and small-scale rheometry are paramount to determining printability on a small scale. With each of these characterization tools understood and utilized correctly, the future in which polymers and can be rapidly and accurately characterized for printing in PBF is possible.